Fabrication and Characterization of Semiconductor Nanolasers

by

Fan Fan

A Dissertation Presented in Partial Fulfillment
of the Requirements for the Degree
Doctor of Philosophy

Approved November 2016 by the
Graduate Supervisory Committee:

Cun-Zheng Ning, Chair
Constantine A. Balanis
Joseph C. Palais
Hongbin Yu

ARIZONA STATE UNIVERSITY

December 2016

ABSTRACT

Semiconductor nanolasers, as a frontier subject has drawn a great deal of attention over the past decade. Semiconductor nanolasers are compatible with on-chip integrations towards the ultimate realization of photonic integrated circuits. However, innovative approaches are strongly required to overcome the limitation of lattice-mismatch issues. In this dissertation, two alternative approaches are employed to overcome the lattice-mismatch issues. i) By taking advantage of nanowires or nanobelts techniques, flexibility in bandgap engineering has been greatly expanded, resulting in the nanolasers with wide wavelength coverage and tunability. Simultaneous two-color lasing in green and red is firstly achieved from monolithic cadmium sulfide selenide nanosheets. The wavelength separation is up to 97 nm at room temperature, larger than the gain bandwidth of a single semiconductor material in the visible wavelength range. The strategies adopted for two-color lasers eventually leads to the realization of simultaneous red, green and blue lasing and white lasing from a single zinc cadmium sulfide selenide nanosheet with color tunability in the full visible range, making a major milestone in the ultimate solution of laser illumination and laser display. In addition, with the help of nanowire techniques, material emission has been extended to mid-infrared range, enabling lasing at ~3 μm from single lead sulfide subwavelength wires at 180 K. The cavity volume of the subwavelength laser is down to 0.44 λ^3 and the wavelength tuning range is over 270 nm through the thermo-optic mechanism, exhibiting considerable potentials for on-chip applications in mid-infrared wavelength ranges. ii) By taking advantage of membrane transfer techniques, heterogeneous integration of compound semiconductor and waveguide material becomes possible, enabling the successful fabrication of membrane based nano-ring lasers on a

dielectric substrate. Thin membranes with total thickness of ~200nm are first released from the original growth substrate and then transferred onto a receiving substrate through a generally applicable membrane transfer method. Nano-ring arrays are then defined by photolithography with an individual radius of 750 nm and a radial thickness of 400-500 nm. As a result, single mode lasing is achieved on individual nano-ring lasers at ~980 nm with cavity volumes down to 0.24 λ^3, providing a general avenue for future heterogeneous integration of nanolasers on silicon substrates.

To my mom with love, who brought me into the realm of physics

ACKNOWLEDGMENTS

I would like to take this opportunity to express my sincerest gratitude to my advisor, my mentor, Prof. Cun-Zheng Ning, who provided me this incredible chance to be a part of his research group to study at ASU. His immense knowledge, inexhaustible enthusiasm, generous encouragement, and tireless guidance inspired me to achieve each single accomplishment and helped me get through the hardship of family tragedy. These precious experiences would become the lifelong benefits on my journey ahead.

I am grateful for my labmates and friends, Dr. Zhicheng Liu and Dr. Sunay Turkdogan, whose talents in physics and material growth not only allowed me to be quickly involved in the group but also permitted numerous advancements in this dissertation. I deeply enjoyed the sleepless nights we were working together for the papers. My genuine acknowledgement goes to the rest of all current and former members of ASU's nanophotonics group, namely, Dr. Kang Ding, Dr. Leijun Yin, Dr. Patricia Nichols, Dr. Derek Caselli, Haotong Wang, Hao Ning, Dongzi Chen, David Shelhammer, Jamie Diaz, Curtis Mackey, Yueyang Yu, Seyed Ebrahim Hashemi Amiri, Praneeth Ranga, Dr. Lin Gan, Dr. Liu Yang and all the other people I had an honor to work with but might have forgotten to mention. Without their priceless discussions and support, this dissertation would not have been possible. I express my special appreciations to Dr. Alan Chin, who shared his valuable technical experience with me. I would also like to give my thanks to colleagues in Tsinghua University, Dr. Yongzhuo Li, Dr. Hao Sun and Dr. Taiping Zhang for the period of collaboration in Beijing.

I gratefully acknowledge the use of the facilities within the Center for Solid State Electronics Research at ASU for device fabrication and all the research support staff for

their helpful assistance and dedications. I would also like to appreciate the China Scholarship Council for providing me with a living allowance during my study and ARO for offering the research funding.

In the end, I wish to thank all of my family, especially my parents who always gave me unconditional love, support, and understanding, and my beloved wife and son who brought me so much joy and happiness, as my foundation of encouragement.

TABLE OF COTENTS

Page

CHAPTER Page

CHAPTER Page

LIST OF TABLES

TABLE Page

LIST OF FIGURES

FIGURE Page

FIGURE Page

FIGURE Page

FIGURE Page

LIST OF ACRONYMS

2D	Two-dimensional
CdS	Cadmium Sulfide
CdSSe	Cadmium Sulfide Selenide
CMOS	Complementary Metal-oxide-semiconductor
CRT	Cathode Ray Tube
CVD	Chemical Vapor Deposition
CW	Continuous Wave
DFB	Distributed Feedback
EDS	Energy Dispersive Spectroscopy
FDTD	Finite-difference Time-domain
FWHM	Full Width at Half Maximum
GaAs	Gallium Arsenide
Ge	Germanium
HRTEM	High-resolution Transmission Electron Microscopy
InP	Indium Phosphide
LCAO	Linear Combination of Atomic Orbitals
LCD	Liquid Crystal Display
LED	Light-emitting Diode
LILO	Light-in-light-out
MBE	Molecular Beam Epitaxy
MIR	Mid-infrared
MOVPE	Metalorganic Vapor Phase Epitaxy
NB	Nanobelt

NW	Nanowire
OLED	Organic Light-emitting Diode
PbS	Lead Sulfide
PhC	Photonic Crystal
PDMS	Polydimethylsiloxane
PIC	Photonic Integrated Circuit
PL	Photoluminescent
PPC	Polypropylene Carbonate
PR	Photoresist
RGB	Red Green and Blue
RSD	Relative Standard Deviation
RT	Room Temperature
SAD	Selected Area Diffraction
SEM	Scanning Electron Microscopy
Si	Silicon
SOI	Silicon-on-insulator
SWW	Subwavelength Wire
TEM	Transmission Electron Microscopy
UV	Ultraviolet
VCSEL	Vertical Cavity Surface Emitting Laser
VLS	Vapor-liquid-solid
VS	Vapor-solid
ZnCdSSe	Zinc Cadmium Sulfide Selenide

CHAPTER 1

INTRODUCTION

1.1 From Nano Science to Semiconductor Nanolasers

Nanoscience, the study of phenomena of materials or structures with at least one dimension on submicron scales, is not limited only to size miniaturization, but also deals with the integration of subunits of various functionalities. Since the 1980s, the discovery of novel materials and phenomena, as well as the progress on new techniques, has been providing great opportunities for the development of nanoscience. As various applications of nanoscience continue to emerge, nowadays, nanotechnology is no longer an unattainable terminology in science fiction. Considerable extensions of nanotechnology have already become parts of our daily lives, such as electronics, healthcare, energy, telecommunication, environmental protection and so on. Nanotechnology has been considered as the major impetus for the next industrial revolution. Due to its appealing prospect, more researchers have been realizing the importance of extending their focus into nanoscience and nanotechnology, and therefore profound impacts have been made in a variety of subjects such as physics, chemistry, biology, engineering and applied sciences. Nanophotonics, defined as the fusion of phonics and nanotechnology, is such a multi-disciplinary frontier. In general, it refers to the investigation of the light-matter interaction on a nanoscale and the utilization of such interaction for many real applications. Nanophotonics has been opening new avenues in the scientific world. Much attention has been recently paid to various subfields of nanophotonics, such as optical interconnects on an integrated circuits chip, which represents a major step towards photonic integrated circuits (PICs) to

ultimately solve the “electronic bottleneck”, currently limiting the speed of computer processors, by improving the speed from a few GHz to THz. The realization of the integrated optical interconnects involves the size down-scaling of different optical components onto a chip, among which a major task is to squeeze the dimensions of the lasers down to a nanoscale to enable size compatibilities with the state-of-the-art electronics. Thus, with the increase of demand for the laser miniaturization, a novel research subject, semiconductor nanolasers, has been attracting considerable interest during the last decade. Tremendous progress has been made with various innovative paradigms of nanolasers both physically and technically, including distributed feedback (DFB) nanolasers [1], vertical cavity surface emitting nanolasers (VCSELs) [2], photonic crystal (PhC) nanolasers [3], [4], metallic cavity nanolasers [5]-[7], plasmonic nanolasers [8]-[10], two-dimensional (2D) material nanolasers [11], [12], and so forth. The operation of the nanolasers has progressed from originally optical pumped, low temperature, pulse operation [16], to electric driven, room temperature (RT), continuous wave (CW) operation [5], [13]. The cavity volume of the nanolasers has been reduced from submicron regime to less than 15 nm in all three dimensions [14].

The realization of nanolaser devices, in general, involves two major aspects: the growth of active media and the definition of feedback cavities. The former is typically achieved by several planar epitaxial techniques, such as molecular beam epitaxy (MBE) or metalorganic vapor phase epitaxy (MOVPE). The latter is commonly accomplished by “top-down” approaches, as a series of well-matured nanofabrication techniques including lithography, etching, metal deposition and thin film techniques, which have long been exploited in the industry for circuits integration. With the development of nanolasers,

however, two essential issues gradually emerged, which are still limited by the traditional planar epitaxial techniques: i) the demands for nanolasers with wide wavelength range coverage and tunability, which require gain material with flexible bandgap choice and premium crystal quality; ii) the demands for silicon (Si) photonics, or the Si-based nanolasers, as an indispensable prerequisite towards the realization of integrated optical interconnects on Si platform, which require heterogeneous integration of the superior gain characteristics of compound semiconductors with the superior passive waveguide and electronic characteristics of Si. The inevitable dilemma of nanolaser fabrications arises as a result of limited lattice-mismatch tolerance of the traditional planar epitaxial techniques. Innovative technologies are demanded to overcome the above issues.

In this dissertation, two alternative techniques are applied: i) semiconductor nanowire (NW) or nanobelt (NB) techniques through "bottom-up" growth approaches, which can produce defect-free semiconductors with broad bandgap tunability; ii) heterogeneous integration techniques through a membrane transfer approach, which can heterogeneously combine compound semiconductor with Si together. As a complementary method to traditional "top-down" and planar epitaxial approaches, these techniques lead to the successful demonstration of different types of nanolasers, including monolithic multi-color nanosheet lasers, mid-infrared (MIR) subwavelength-wire (SWW) lasers, and membrane based nano-ring lasers, which will be introduced in the following chapters.

1.2 Overview of Nanowire and Nanobelt Techniques via Bottom-up Approach

The emergence of bottom-up approach provided enormous opportunities to assemble complex nanostructure chemically or physically by atomic-level building blocks to

surmount the limitation of the top-down approach and planar epitaxial growth. Semiconductor NWs or NBs, as one of the most successful examples produced by bottom-up approaches, have been attracting great attention over the last two decades. Semiconductor NWs or NBs typically have at least one transverse dimension in tens or hundreds of nanometer scale. Due to their small cross sections, semiconductor NWs or NBs can tolerant much larger lattice mismatch (over 10% of lattice difference), than the traditionally planar epitaxial growth of thin film from the substrate. Such advantages provide more flexibility in the material and bandgap choices with defect-free natures or high crystal quality. The nature of semiconductor NWs or NBs guarantees their potential to be exploited as a flexible gain material with high crystal quality. On the other hand, due to their high refractive index contrast to the surrounding air, semiconductor NWs or NBs can provide good confinement to optical modes with relatively large Q factor. Consequently, amplified spontaneous emission can be easily established and eventually oscillate as lasing modes in semiconductor NWs or NBs. Therefore, semiconductor NWs or NBs are also naturally satisfactory optical cavities with small cavity volume. Due to these unique features, semiconductor NWs or NBs have exhibited great promise in semiconductor nanolasers, as one of the most important building blocks for PICs in nanophotonics.

Various types of semiconductor NW or NB lasers have been reported [15]-[18], since the very first demonstration of lasing in ZnO NWs [19]. Yet, a number of challenging issues remain. One of the challenges is to achieve lasing in multiple wavelengths from a single nanostructure. Such lasing capability will enable novel applications of integrated devices, which I will extensively discuss in Chapter 2 and Chapter 3 in more detail. Another

important aspect of research is to expand the lasing wavelengths into near infrared and MIR range. Most of the research works so far have been focused on attaining lasing at visible and UV wavelengths, while many detection and sensing applications require nanoscale sources in long wavelength regimes, which will be discussed in Chapter 4.

The growth of NWs or NBs involves different mechanisms, among which, vapor-liquid-solid (VLS) growth and vapor-solid (VS) growth are common.

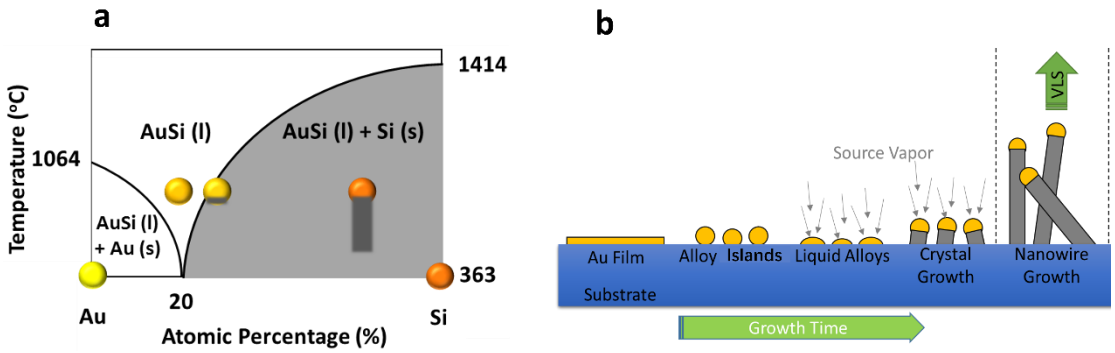

Figure 1.1 Illustration of VLS growth mechanism. (a) Binary phase diagram of Au and Si. (b) Schematic diagram of VLS growth sequence with diverse morphologies in different growth stages.

The NWs growth is typically dominated by VLS growth. It was firstly proposed by Wagner and Ellis [20] at Bell Lab in the early 1960s and was later used for growing III-V NWs by scientists at Hitachi [21] in the early 1990s. Here, I take the growth of Si NWs as an example for illustration. The growth of Si NWs via VLS mechanism typically employs Au (or some other heavy metals such as Ag, Pt, Cu, Ni, Co, and Ti) as a catalyst. The melting temperature of the Au-Si alloy reaches a minimum of 363 ℃ at the Au-Si eutectic point, which is much lower than the Si melting point, 1414 ℃, as shown in Fig. 1.1a. The growth starts with a substrate such as Si, coated by catalyst (Au) layer. As schematically shown in Fig. 1.1b, with the increase of substrate temperature, the Au catalyst layer becomes liquid

alloy islands and breaks up into droplets once the eutectic point is reached. Meanwhile, source vapor has been evaporated and transported to the substrate region and has been continuously applied and adsorbed into the liquid droplets on the substrate surface, till the occurrence of supersaturation. Nucleation then happens at the bottom of the alloy droplets, which starts the growth of NWs.

The growth of uniform NBs or nanosheets, however, involves both VLS and VS mechanism. In this case, NWs are grown at the first stage with an increase of temperature.

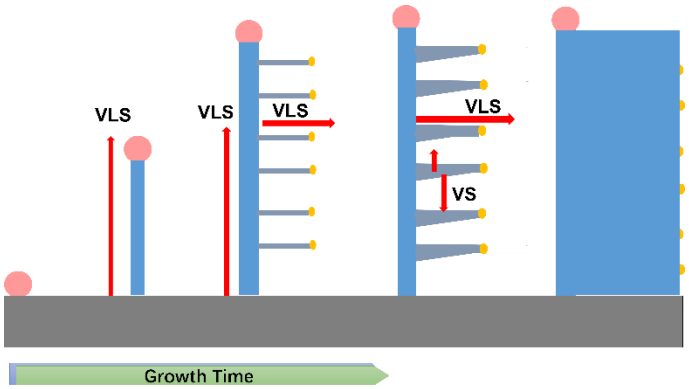

Figure 1.2 Schematic diagram of uniform NB or nanosheet growth

As the temperature further increases, the growth of secondary NWs starts via self-catalysis, vertical to initial VLS growth direction, under a high level of supersaturation. Meanwhile, additional VS growth fills the gaps between the secondary NWs to expand the structure to NBs or nanosheets with lateral uniformity.

1.3 Overview of Si Photonics and Membrane-Transfer Techniques

Lasers that are compatible with Si substrate have long been a goal, since the rapid development of electronic integration. To overcome the “bottleneck” of the date transfer rate in electronic circuits, short range integrated optical interconnects adaptable to state-of-

the-art complementary metal-oxide-semiconductor (CMOS) technique are needed to dramatically increase the bandwidth of communication network on chip. Beyond the well-matured CMOS technique, additional desirable properties make Si as the irreplaceable substrate choice for the realization of PICs, known as Si photonics. As substrates, Si has very low defect density and high thermal conductivity; As a waveguide material, Si benefits from propagation loss one order of magnitude lower than that of compound semiconductors, and its native oxide, SiO_2, servers as high-quality waveguide cladding with a low index.

Despite the considerable advantages, there is a fundamental barrier preventing the development of Si-based light source: the indirect band structure of Si, which results in optical transition far less efficient, since the conservation of energy and momentum requires photons to be involved in carrying out the excess momentum in radiative recombination. Compound semiconductors, such as indium phosphide (InP) and gallium arsenide (GaAs), on the other hand, have direct band structure, facilitating the optical process more rapidly via a simple phonon-free process. Wide chasm thus formed between light-emitting devices, dominated by the compound semiconductor, and passive optical devices, dominated by elementary semiconductors, such as Si or germanium (Ge).

Many attempts have been made to eliminate the chasm between the material uses in active and passive optical devices, such as Ge lasers [22] under high-level injection, when electrons start to occupy the direct band valley for radiative recombination. Si Raman laser [23] is another example that uses indirect bandgap material as an active medium, where the optical process is helped by phonon emitting through Raman scattering mechanism. Nonetheless, those devices still suffer from low efficiency as the intrinsic

shortcoming of indirect bandgap material. The idea of heterogeneous integration of Si with compound semiconductors has also been pursued. Various laser devices have been demonstrated through heterogeneous integration, including three major categories: heterogeneous growth of compounds semiconductors on Si [24], [25], direct wafer bonding [26]-[28], and metallic device bonding [29]. To overcome the lattice mismatch, the heterogeneous wafer growth requires the use of bulky defective buffer layer to mitigate the lattice strain and thermal expansion. Yet, the issue of long term reliability has prevented this approach from being widely adopted. More impressive results have been reported via direct wafer bonding approaches[30], [31]. However, stringent requirement of bonding interface and inefficient use of compound layer remain a problem. The metallic device bonding has been applied in many industry fields, but precise alignment is still a technical barrier for the massive transfer of prefabricated lasers on a large scale.

In 2006, researchers from John Rogers' group reported an alternative technique for more efficient heterogeneous integration [32], by using an elastomer stamp to assist the membrane transfer process. Since then, both edge emitting [33] and surface emitting lasers [3] have been successfully fabricated. The use of the method is based on that the adhesion energy between semiconductor membrane and elastomer has a peel-speed dependency. High peel-speed is employed for lifting the membrane from the donor substrate, while low peel-speed is employed for releasing the membrane onto the receiving substrate. However, calibration of peel-speed is required for different semiconductor membranes and elastomer interface to determine the minimum peel-speed for membrane lifting and the maximum peel-speed for membrane releasing.

Recently, a novel transfer method has been developed for 2D monolayers [34]. The method includes an intermediate sacrificial layer between the monolayer and the elastomer, and has an advantage of independence on peeling speed. Such transfer method greatly simplifies the complexity of transfer procedure and eliminates the need for speed control and calibration. By adopting the method to semiconductor membrane transfer, successful heterogeneous integration of compound semiconductor nano-ring lasers onto a low-index dielectric substrate has been achieved, which will be specifically discussed in Chapter 6.

1.4 Structure of the Dissertation

Contents of this dissertation are organized in the following order:

In Chapter 2, the physics basis of semiconductor nanolasers has been distributed into the discussion of several subtopics, considered as the elementary tools for the following theoretical analysis.

From Chapter 3 to Chapter 5, NWs and NBs techniques by "bottom-up" growth are applied, allowing the accomplishments of defect-free semiconductors with broad bandgap tunability and MIR emission ability. More specifically, in Chapter 3, the results of simultaneous two-color lasing from a monolith cadmium sulfide selenide (CdSSe) nanosheet are enabled through a special cavity design. The wavelength separation reaches 97 nm, much larger than the typical gain bandwidth of a single semiconductor material.

In Chapter 4, the adoption of the strategies used in Chapter 3 leads to the successful demonstration of the simultaneous red, green and blue (RGB) lasing from a monolithic zinc cadmium sulfide selenide (ZnCdSSe) multi-segment nanosheet. By independently

controlling the optical pumping of each segment, full-color tunable lasing and white color lasing are achieved in particular for the first time.

In Chapter 5, MIR lasing is obtained at around 3 μm from a single PbS SWW with the maximal operation temperature up to 180 K and the cavity volume of 0.44 λ^3 in vacuum. The wavelength tunability of the PbS lasers has also been exhibited, covering over 270 nm through the thermos-optic mechanism.

In Chapter 6, the generally applicable membrane transfer technique is adopted for the heterogeneous integration of the compound semiconductor membrane with the dielectric substrate, facilitating the following fabrication of membrane based nano-ring arrays. Single mode lasing is achieved at RT with individual cavity volume down to 0.39 λ^3.

In Chapter 7, conclusive remarks are made to summarize the dissertation and future work suggestions and outlook are provided.

CHAPTER 2

PHYSICS BASIS OF SEMICONDUCTOR NANOLASERS

2.1 Introduction

The physics basis to realize the operation of semiconductor nanolasers in general consists of two major issues: i) optical or electrical excitation to generate free carriers till population inversion to provide positive gain in the active region; ii) proper optical cavity to provide feedback for photons to create stimulated emission. The purpose of this chapter is to examine the theoretical foundations of those two building blocks of semiconductor nanolaser: the optical transition process and the cavity feedback process. Several subtopics spreading around the two building blocks are explicitly discussed here, including material gain and absorption, non-parabolic transition, solutions of rate equations, gain guiding effect, anti-waveguiding modes, rectangular waveguide, and dielectric disk cavity. Those are considered as elementary tools for the further analysis applied in the next few chapters.

2.2 Optical Process in Semiconductor Nanolasers

2.2.1 Absorption or Gain Coefficient and Spontaneous Emission Rate

In the following section, optical absorption or gain coefficient, and spontaneous emission rate of nanolaser gain material are derived through semi-classical quantum mechanical theory. Several textbooks [35]-[37] are consulted for the deduction of analytical expressions. Assuming the active region of semiconductor nanolaser is a perfect crystal structure, electrons in such a periodical lattice structure can be written by time-independent Schrödinger equation:

$$H_0(\psi_n) = E_n\psi_n \tag{2.1}$$

where H_0 is "unperturbed" Hamiltonian and the time-independent wave function ψ_n is the eigen solution of H_0, with energy E_n as the eigen value. The appearance of light can be considered as the photons interacting with electrons, and the total Hamiltonian is the sum of "unperturbed" Hamiltonian and an additional perturbation Hamiltonian term H',

$$H = H_0 + H' \tag{2.2}$$

written as:

$$H' = -\frac{e}{m_0}\vec{\boldsymbol{A}} \cdot \vec{\boldsymbol{p}} \tag{2.3}$$

where the $\vec{\boldsymbol{A}}$ is the vector potential of electric field of photons, $\vec{\boldsymbol{p}}$ is the momentum of electrons. Consequence of the perturbation is that electron transits from an initial state ψ_i to a final state ψ_f, with the probability W_{if} obeying Fermi's golden rule,

$$W_{if} = \frac{2\pi}{\hbar}\left|M_{if}\right|^2 \delta\left(E_f - E_i - \hbar\omega\right) \tag{2.4}$$

where M_{if} is the matrix element with the expression:

$$M_{if} = \int \psi_f^* H' \psi_i \mathrm{d}^3\mathbf{r} = -\frac{eA_0}{2m_0}\hat{\boldsymbol{e}} \cdot \vec{\boldsymbol{p}}_{cv} \tag{2.5}$$

In (2.5), $\hat{\boldsymbol{e}}$ is the unit vector of $\vec{\boldsymbol{A}}$, A_0 is the amplitude of $\vec{\boldsymbol{A}}$, and $\vec{\boldsymbol{p}}_{cv}$ is the interband matrix element that can be estimated by Kane's parameter P [35], [37]:

$$\left|\hat{\boldsymbol{e}} \cdot \vec{\boldsymbol{p}}_{cv}\right|^2 = \frac{m_0^2}{\hbar^2}P^2 = \left(\frac{m_0}{m_e} - 1\right)\frac{m_0 E_g\left(E_g + \Delta\right)}{2\left(E_g + \frac{2}{3}\Delta\right)} \tag{2.6}$$

where m_0 is the electron mass, m_e is the effective mass of electron, E_g is the bandgap energy of the active region, and Δ is the band split-off energy. The transition probability of a single electron from valence band to conduction band in (2.4) can be therefore expressed as:

$$W_{vc} = \frac{\pi e^2 A_0^2}{2m_0^2 \hbar} |\hat{\boldsymbol{e}} \cdot \vec{\boldsymbol{p}}_{cv}|^2 \delta(E_c - E_v - \hbar\omega) \tag{2.7}$$

Therefore, the total upward transition rate or the absorption rate per unit volume can be found by summing over the entire *k* space, expressed as:

$$R_{vc} = \frac{2}{V} \sum_k W_{vc}(k) f_v (1 - f_c) \tag{2.8}$$

and the total downward transition or the stimulated emission rate per unit volume can be written as:

$$R_{cv} = \frac{2}{V} \sum_k W_{cv}(k) f_c (1 - f_v) \tag{2.9}$$

where V is the volume of active region, W_{vc} and W_{cv} are upward and downward transition probabilities respectively, f_c and f_v are Fermi distribution in conduction and valence bands respectively, taking the form,

$$f_{c,v} = \frac{1}{1 + e^{(E_{c,v} - E_f)/kT}} \tag{2.10}$$

The net absorption rate per unit volume then becomes

$$\begin{aligned} R = R_{vc} - R_{cv} &= \frac{2}{V} \sum_k W_{vc}(k) [f_v (1 - f_c) - f_c (1 - f_v)] \\ &= \frac{2}{V} \sum_k W_{vc}(k) (f_v - f_c) \\ &= \frac{2}{V} \sum_k W_{vc}(k) (1 - f_e - f_h) \end{aligned} \tag{2.11}$$

where $f_e = f_c$, $f_h = 1 - f_v$. Substituting (2.7) into (2.11), we have the net absorption rate per unit volume as:

$$R = \frac{\pi e^2 A_0^2}{2m_0^2 \hbar} \cdot \frac{2}{V} \sum_k |\hat{\boldsymbol{e}} \cdot \vec{\boldsymbol{p}}_{cv}|^2 (1 - f_e - f_h) \delta(E_c - E_v - \hbar\omega) \tag{2.12}$$

In order to convert the sum over the entire *k* space in (2.12) into the energy *E* space, the concept of joint density of state needs to be utilized. Assuming near bandedge, the *k*-*E* relation of electrons can be well estimated by parabolic approximation given by,

$$E = E_c - E_v = E_g + E_e + E_h = E_g + \frac{\hbar^2 k^2}{2m_e} + \frac{\hbar^2 k^2}{2m_h} \tag{2.13}$$

where E_c and E_v are the conduction and the valence band energies respectively, E_e and E_h are the free energies of electrons and holes, respectively, and m_h is the effective mass of hole.

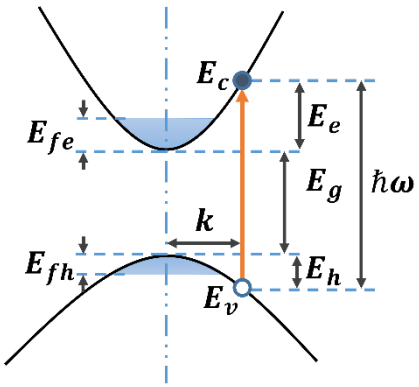

Figure 2.1 Band diagram illustrating the relation between wave vector, conduction and valence band energy, bandgap energy, electron and hole free energy, quasi-fermi energy and photon energy.

Now we can define a new term m_r, known as reduced mass of electron-hole pairs, and (2.13) is therefore simplified as:

$$E = E_g + \frac{\hbar^2 k^2}{2m_r} \tag{2.14}$$

where

$$\frac{1}{m_r} = \frac{1}{m_e} + \frac{1}{m_h} \tag{2.15}$$

and the value of E_e and E_h can be determined by the following two expressions:

$$E_e = \frac{m_r}{m_e}(E - E_g) \tag{2.16}$$

$$E_h = \frac{m_r}{m_h}(E - E_g) \tag{2.17}$$

By introducing the reduced mass of electron-hole pairs m_r, we can now give the joint

density of state for the electron-hole pairs, similar to the derivation of electron density of states, to alter the integration from the k space to the E space. That is

$$N_{cv}(E) = \frac{\sqrt{2}(m_r)^{\frac{3}{2}}(E-E_g)^{\frac{1}{2}}}{\pi^2\hbar^3} \tag{2.18}$$

Thus (2.12) can be re-written as:

$$R = \frac{\pi e^2 A_0^2}{2m_0^2\hbar} \cdot |\hat{\boldsymbol{e}} \cdot \vec{\boldsymbol{p}}_{cv}|^2 \cdot \int_{E_g}^{\infty} N_{cv}(E)(1 - f_e - f_h)\delta(E - \hbar\omega)\,\mathrm{d}E \tag{2.19}$$

Considering the finite dipole lifetime, strict energy conservation does not hold and the delta function should be replaced by a linewidth broadening function. Therefore, we have the absorption coefficient expressed as

$$\alpha = \frac{R}{S/\hbar\omega} = \frac{\pi e^2 A_0^2}{2m_0^2\hbar} \cdot |\hat{\boldsymbol{e}} \cdot \vec{\boldsymbol{p}}_{cv}|^2 \cdot \int_{E_g}^{\infty} N_{cv}(E)(1 - f_e - f_h)\mathcal{L}(E - \hbar\omega)\,\mathrm{d}E \tag{2.20}$$

In (2.20), S is the absolute value of pointing vector, and $\mathcal{L}(E - \hbar\omega)$ is the Lorentz function, known as

$$S = \frac{1}{2} n_r c \varepsilon_0 \omega^2 |A_0|^2 \tag{2.21}$$

$$\mathcal{L}(E - \hbar\omega) = \frac{1}{\pi} \cdot \frac{\gamma\hbar}{(\gamma\hbar)^2 + (E - \hbar\omega)^2} \tag{2.22}$$

where $\gamma = 1 \times 10^{13}\mathrm{s}^{-1}$ is the dephasing rate.

$$\alpha = \frac{\pi e^2}{m_0^2 c n_r \varepsilon_0 \omega} \cdot |\hat{\boldsymbol{e}} \cdot \vec{\boldsymbol{p}}_{cv}|^2 \cdot \int_{E_g}^{\infty} N_{cv}(E)(1 - f_e - f_h)\mathcal{L}(E - \hbar\omega)\,\mathrm{d}E \tag{2.23}$$

Correspondingly, the gain coefficient can be written as

$$g = -\alpha = \frac{\pi e^2}{m_0^2 c n_r \varepsilon_0 \omega} \cdot |\hat{\boldsymbol{e}} \cdot \vec{\boldsymbol{p}}_{cv}|^2 \cdot \int_{E_g}^{\infty} N_{cv}(E)(f_e + f_h - 1)\mathcal{L}(E - \hbar\omega)\,\mathrm{d}E \tag{2.24}$$

Figure 2.2 gives the calculation results of optical gain of Cadmium Sulfide (CdS) material through Eq. (2.24) as an example. With the increase of carrier density, the gain varies from negative to positive, indicating the material start to possess the capability of

stimulated transition. It is worth to note that at the bandedge, the gain typically clamps at a small value.

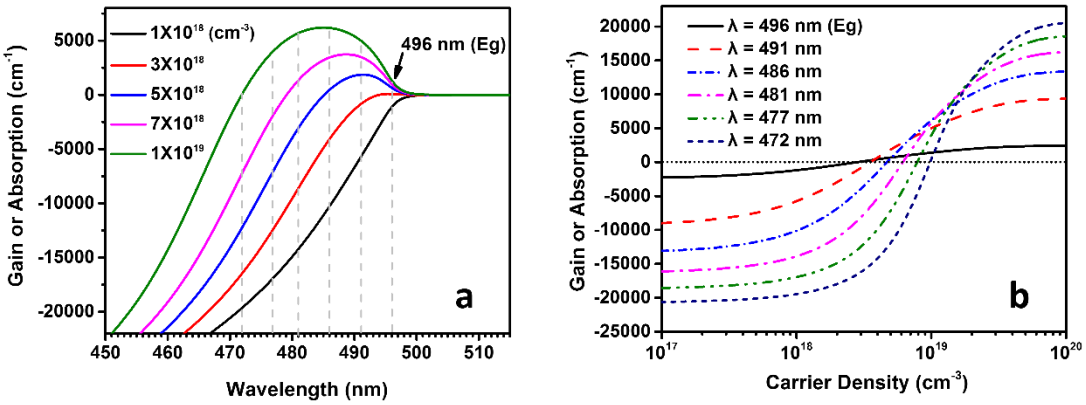

Figure 2.2 Optical gain of CdS (a) gain spectra of CdS at different carrier density (b) gain versus carrier density at different wavelengths

Thus to maximize the optical gain, we need to design nanolaser at a shorter wavelength.

Next, to give the spontaneous emission rate, we firstly consider the spontaneous emission rate per unit photonic volume,

$$R_{cv}^{sp} = A_{21} f_c (1 - f_v) \tag{2.25}$$

where according to the Einstein relationship:

$$A_{21} = N_{ph} B_{21} \tag{2.26}$$

In (2.26), N_{ph} and B_{21} are the photon density of states and the stimulated emission rate factor, respectively, given by

$$N_{ph} = \frac{\omega^2}{\pi^2 \hbar (c/n_r)^3} \tag{2.27}$$

$$B_{21} = \frac{\pi e^2}{m_0^2 n_r^2 \varepsilon_0 \omega V_{ph}} |\hat{\boldsymbol{e}} \cdot \vec{\boldsymbol{p}}_{cv}|^2 \tag{2.28}$$

Substituting (2.26), (2.27) and (2.28) into (2.25), we have

$$R_{cv}^{sp} = \frac{n_r e^2 \hbar \omega}{\pi \hbar^2 \varepsilon_0 m_0^2 c^3 V_{ph}} |\hat{\boldsymbol{e}} \cdot \vec{\boldsymbol{p}}_{cv}|^2 f_e f_h \tag{2.29}$$

Then the total spontaneous emission rate is:

$$r_{cv}^{sp} = \frac{2}{V}\sum_k A_{21} \cdot V_{ph} \cdot f_e f_h \delta(E - \hbar\omega)$$

$$= \frac{n_r e^2 \hbar\omega}{\pi\hbar^2 \varepsilon_0 m_0^2 c^3} |\hat{\boldsymbol{e}} \cdot \vec{\boldsymbol{p}}_{cv}|^2 \int_{E_g}^{\infty} N_{cv}(E) f_e f_h \cdot \delta(E - \hbar\omega) \mathrm{d}E \quad (2.30)$$

With the consideration of linewidth broadening, the spontaneous emission rate finally takes the form,

$$r_{cv}^{sp} = \frac{n_r e^2 \hbar\omega}{\pi\hbar^2 \varepsilon_0 m_0^2 c^3} |\hat{\boldsymbol{e}} \cdot \vec{\boldsymbol{p}}_{cv}|^2 \int_{E_g}^{\infty} N_{cv}(E) f_e f_h \cdot \mathcal{L}(E - \hbar\omega) \mathrm{d}E \quad (2.31)$$

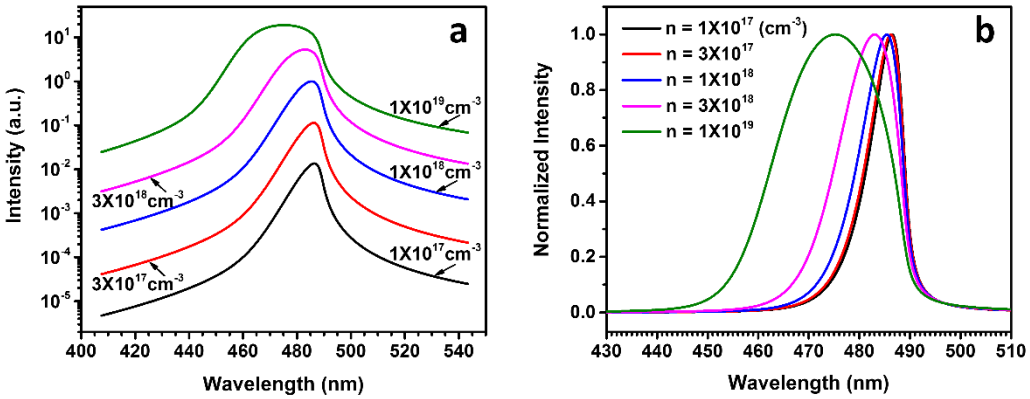

Figure 2.3 Spontaneous emission spectra of CdS (a) relative spontaneous emission intensity of CdS at different carrier densities (b) normalized spontaneous spectra at different carrier densities.

Figure 2.3 presents the calculation results of spontaneous spectra of CdS through Eq. (2.31). As can be seen clearly that, with the rise of carrier density, not only the spontaneous emission intensity but also the width of the spontaneous spectra gets increased. The full width at half maximum (FWHM) of the spontaneous spectrum gets dramatically increased when the carrier density exceeds 1×10^{18} cm^{-3}.

2.2.2 Optical Transition in Non-Parabolic Band Structure

In the above section, all the equations and calculations are derived under the parabolic band

structure approximation given by (2.13). Such approximation is indeed valid in most cases, especially for wide bandgap semiconductor materials emitting at ultraviolet (UV) and Visible range. For narrow bandgap material, emitting in MIR range or at an even longer wavelength, the behavior of non-parabolic band structure, in reality, becomes non-negligible. Deviations arise between the experimental results and theoretical prediction by only the parabolic approximation is used without any non-parabolic correction.

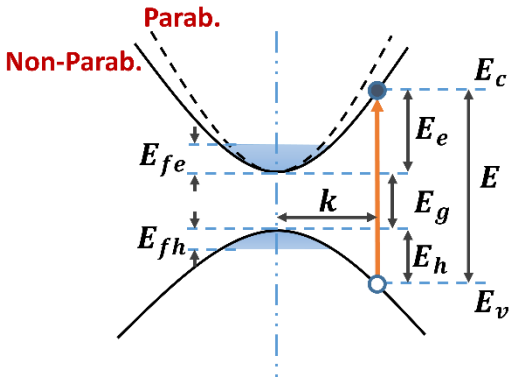

Figure 2.4 Band diagram of non-parabolic conduction band comparing to parabolic conduction band

Thus, non-parabolic band structure model needs to be applied for more precise estimation. The non-parabolic coefficient for evaluating the degree of non-parabolicity is given by [38]:

$$\alpha = \frac{\left(1-\frac{m_e}{m_0}\right)^2}{E_g} \tag{2.32}$$

Larger non-parabolic coefficient results in more distinctive non-parabolic behavior. According to (2.32), either narrower bandgap or smaller electron mass could contribute to more severe non-parabolicity. Figure 2.4. schematically shows the band diagram of non-parabolic conduction band compared to parabolic band structure. The non-parabolic dispersion in conduction band takes the form [39]:

$$\frac{\hbar k^2}{2m_e} = E_e(1 + \alpha E_e) \tag{2.33}$$

where α is the non-parabolic coefficient in (2.32), while the dispersion relation in valence band is still given by,

$$E_h = \frac{\hbar k^2}{2m_h} \tag{2.34}$$

Several issues are affected due to the non-parabolicity in band structure expressed in (2.33) and are explicated as follows:

i) Electron Density of States and Carrier Density to Quasi-Fermi Level Relation:

The electron density of states can be written as:

$$\rho_c^{non}(E_e) = \frac{k^2}{\pi^2}\frac{dk}{dE^e} \tag{2.35}$$

By substituting (2.33), we have:

$$\rho_c^{non}(E_e) = \frac{1}{2\pi^2}\left(\frac{2m_e}{\hbar^2}\right)^{\frac{3}{2}} E_e^{\frac{1}{2}}(1+\alpha E_e)^{\frac{1}{2}}(1+2\alpha E_e) \tag{2.36}$$

The carrier density for nonparabolic case is therefore:

$$n(E_{fe}) = \int_0^\infty \rho_c^{non}\cdot f_c \,\mathrm{d}E_e$$

$$= \frac{1}{2\pi^2}\left(\frac{2m_e}{\hbar^2}\right)^{\frac{3}{2}} \int_0^\infty E_e^{\frac{1}{2}}(1+\alpha E_e)^{\frac{1}{2}}(1+2\alpha E_e)\cdot f_e(E_{fe})\,\mathrm{d}E_e \tag{2.37}$$

which reflects the relation between carrier density and quasi-Fermi level in the non-parabolic band situation.

ii) Electron and Hole Free Energy and Inversed k-E Relation:

According to (2.33) and (2.34), the electron and hole free energies can be derived as:

$$E_e = \sqrt{\frac{1}{4\alpha^2} + \frac{1}{\alpha}\frac{\hbar^2 k^2}{2m_e}} - \frac{1}{2\alpha} \tag{2.38}$$

$$E_h = \frac{\hbar^2 k^2}{2m_h} \tag{2.39}$$

and thus the dispersion relation can be expressed as:

$$E - E_g = E_e + E_h = \sqrt{\frac{1}{4\alpha^2} + \frac{1}{\alpha}\frac{\hbar^2 k^2}{2m_e}} + \left(\frac{\hbar^2 k^2}{2m_h} - \frac{1}{2\alpha}\right) \tag{2.40}$$

After simple math, we can rewrite (2.40) as:

$$\left(\frac{\hbar^2}{2m_h}\right)^2 k^4 - \left[\frac{\hbar^2}{2\alpha}\left(\frac{1}{m_e} + \frac{1}{m_h}\right) + \frac{\hbar^2}{m_h}\left(E - E_g\right)\right] k^2 + \left[\left(E - E_g\right)^2 + \frac{1}{\alpha}\left(E - E_g\right)\right] = 0 \tag{2.41}$$

By solving (2.41), the inverted dispersion relation is given by

$$k = \sqrt{\frac{\left[\frac{\hbar^2}{2\alpha}\left(\frac{1}{m_e}+\frac{1}{m_h}\right)+\frac{\hbar^2}{m_h}\left(E-E_g\right)\right]}{2\cdot\left(\frac{\hbar^2}{2m_h}\right)^2} - \frac{\sqrt{\left[\frac{\hbar^2}{2\alpha}\left(\frac{1}{m_e}+\frac{1}{m_h}\right)+\frac{\hbar^2}{m_h}\left(E-E_g\right)\right]^2 - 4\left(\frac{\hbar^2}{2m_h}\right)^2\left[\left(E-E_g\right)^2+\frac{1}{\alpha}\left(E-E_g\right)\right]}}{2\cdot\left(\frac{\hbar^2}{2m_h}\right)^2}} \tag{2.42}$$

iii) Joint Density of States:

By taking differential to (2.33) and (2.34), we have

$$(2\alpha E_e + 1)dE_e = \frac{\hbar^2 k}{m_e} \cdot dk \tag{2.43}$$

$$dE_h = \frac{\hbar^2 k}{m_h} \cdot dk \tag{2.44}$$

Thus, the differential of total transition energy is:

$$dE = dE_e + dE_h = \left(\frac{\hbar^2 k}{m_e} \cdot \frac{1}{2\alpha E_e + 1} + \frac{\hbar^2 k}{m_h}\right) dk \tag{2.45}$$

Applying (2.38) into (2.45), the differential is now:

$$dE = \left(\frac{\hbar^2 k}{m_e} \cdot \frac{1}{\sqrt{1+2\alpha\frac{\hbar^2 k^2}{m_e}}} + \frac{\hbar^2 k}{m_h} \right) dk \tag{2.46}$$

Then the non-parabolic joint density of states N_{cv}^{non} can be written as:

$$N_{cv}^{non} = \frac{k^2}{\pi^2} \cdot \frac{dk}{dE} = \frac{k^2}{\pi^2} \cdot \left(\frac{\hbar^2 k}{m_e} \cdot \frac{1}{\sqrt{1+2\alpha\frac{\hbar^2 k^2}{m_e}}} + \frac{\hbar^2 k}{m_h} \right)^{-1} \tag{2.47}$$

Substituting (2.42) into (2.47), we can get the final analytical expression for the non-parabolic case.

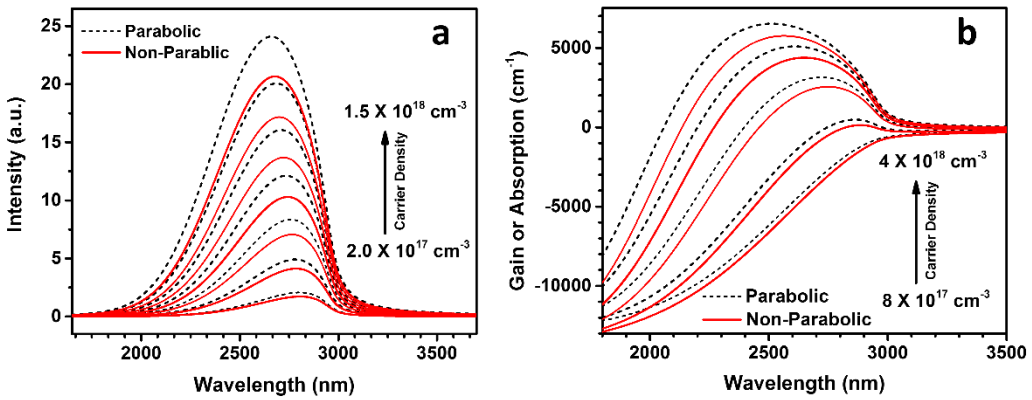

Figure 2.5 Comparison of parabolic and non-parabolic band structure with increase of carrier density (a) calculated spontaneous emission spectra of PbS in both cases (b) calculated gain spectra of PbS in both cases

By replacing the N_{cv} in (2.24) and (2.31) by N_{cv}^{non} in (2.47), I calculated the gain and spontaneous emission spectra of PbS as a representative example of narrow bandgap material emitting in MIR range. The parameters used in simulation are taken from Ref. [6] and temperature is assumed at 300 K. Figure 2.5 shows the comparison of calculated optical properties between parabolic and non-parabolic band structure through the above expressions. Due to the band structures difference resulting in the discrepancy in density of states, both spontaneous emission rate and optical gain in non-parabolic case have lower

value than that in parabolic case. Slightly red shifting is also noticed in non-parabolic band structure case comparing to it counter-part, as a result of the difference in density of states.

2.2.3 Laser Rate Equation and Steady State Solution

To reveal the operating characteristics and more underlying physics of semiconductor nanolasers, rate equation is investigated in this section. Both electrons and photons' behavior can be well described and correlated through two coupled differential equations. Considering optical pumping, the equations can be written as:

$$\frac{dN}{dt} = \frac{P}{\hbar\omega \cdot V} - GS - \frac{N}{\tau_e} \tag{2.48}$$

$$\frac{dS}{dt} = \Gamma GS - \frac{S}{\tau_{ph}} + \frac{\Gamma F \beta}{\tau_{sp}} N \tag{2.49}$$

where N and S are the electron and photon densities respectively, P is the optical pumping power, $\hbar\omega$ is the pumping photon energy, V is the volume of gain media, Γ is the optical confinement factor, β is the spontaneous emission coupling factor, and τ_{sp} is the spontaneous emission lifetime. Other parameters, such as the Purcell factor F, the total carrier lifetime τ_e, the photon lifetime τ_{ph} and the generation rate of stimulated photons G are illustrated as follows,

The Purcell factor F in (2.49) is given by [37]

$$F = \frac{3}{4\pi^2}\left(\frac{\lambda}{n_r}\right)^3 \left(\frac{Q}{V}\right) \tag{2.50}$$

where λ is the emission wavelength, n_r is the refractive index of the cavity, Q is the quality factor, and V is the cavity volume.

The total carrier lifetime τ_e is given by,

$$\tau_e = [A + B(1 - \beta + F\beta)N + CN^2]^{-1} \tag{2.53}$$

where A is the non-radiative recombination rate, defined as $\frac{1}{\tau_{nr}}$, B is the radiative recombination coefficient, defined as $\frac{1}{\tau_{sp} \cdot N}$, and C is the Auger recombination coefficient, defined as $\frac{1}{\tau_{Aug} \cdot N^2}$. The τ_{nr}, τ_{sp} and τ_{Aug} in the above definitions are non-radiative, radiative and Auger recombination lifetimes, respectively.

The photon lifetime in (2.49) is given by,

$$\tau_{ph} = \frac{Q}{\omega} \tag{2.51}$$

where ω is the photon angular frequency and Q is the quality factor in (2.50).

The generation rate of stimulated photons G is given by,

$$G = g \cdot v_g \tag{2.52}$$

where g is the material gain of active region and v_g is the group velocity.

At steady state, all terms differential to time become zero. The equations in (2.48) and (2.49) are equal to zero. That is,

$$\frac{P}{\hbar\omega \cdot V} - GS - \frac{N}{\tau_e(N)} = 0 \tag{2.53}$$

$$\Gamma GS - \frac{S}{\tau_{ph}} + \frac{\Gamma F\beta}{\tau_{sp}} N = 0 \tag{2.54}$$

By solving (2.53) and (2.54), the relation between input and output light of an optically pumped nanolaser can be established.

In addition, the FWHM of semiconductor laser linewidth at steady state is given by [41],

$$\Delta\lambda = \frac{\lambda^2}{4\pi c \tau_{sp} SV}(1+\alpha_e^2) \tag{2.55}$$

where λ is the photon wavelength, c is the speed of light, τ_{sp} is the spontaneous lifetime, S is the photon density, V is the cavity volume and α_e is the linewidth enhancement factor.

Figure 2.6a calculate the lasing characteristics of an optical pumped InGaAs nanolaser emitting at 1.5 μm. At steady state, also known as CW operation, the linewidth of laser emission narrows with the increase of pumping power, indicating the transition of output light from incoherently spontaneous emission to coherently stimulated emission.

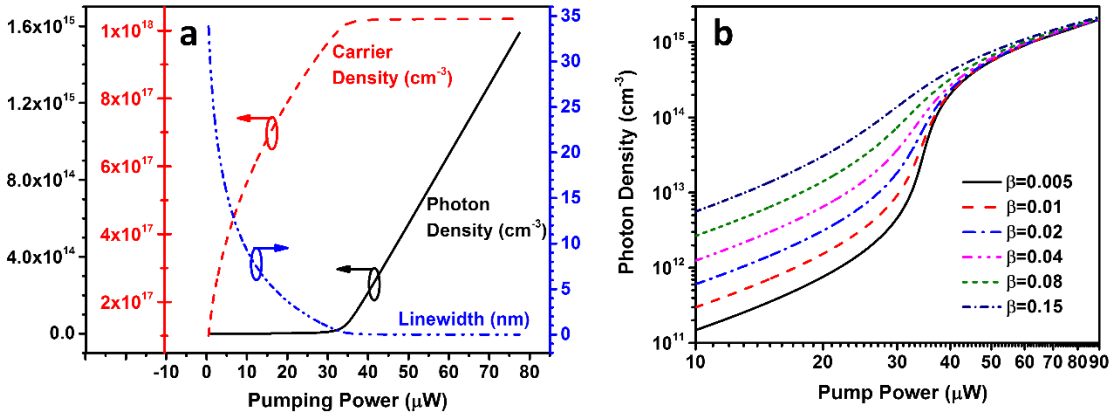

Figure 2.6 Steady state solution of semiconductor laser rate equation (a) laser operating characteristics of carrier density, photon density and lasing linewidth as function of pumping power at steady state. (b) LILO curve on log-log scale at different β values.

Figure 2.6b gives the calculation result of the light-in-light-out (LILO) features at different β values. As one of the distinctive natures of a nanolaser, the compact cavity volume contributes to larger β factor, resulting in "soft" threshold behavior in LILO relation, compared to a traditional semiconductor laser with a large cavity volume.

2.2.4 Transient Solution and Pulse Induced Linewidth Broadening

To study the transient property of nanolasers, I numerically solve the coupled differential equations in (2.48) and (2.49). Here, the fourth order Runge-Kutta method [42] was applied to the equations solving, described as follows.

Assume the coupled differential equations take the form,

$$\begin{cases} \frac{dx}{dt} = f(t,x,y) \\ \frac{dy}{dt} = g(t,x,y) \end{cases} \tag{2.56}$$

with the initial values,

$$\begin{cases} x(t_0) = x_0 \\ y(t_0) = y_0 \end{cases} \tag{2.57}$$

The iterative algorithm is given by

$$\begin{cases} x_{k+1} = x_k + \frac{h}{6}(f_1 + 2f_2 + 2f_3 + f_4) \\ y_{k+1} = y_k + \frac{h}{6}(g_1 + 2g_2 + 2g_3 + g_4) \end{cases} \tag{2.58}$$

where

$$\begin{cases} f_1 = f(t_k, x_k, y_k) \\ f_2 = f\left(t_k + \frac{h}{2}, x_k + \frac{h}{2}f_1, y_k + \frac{h}{2}g_1\right) \\ f_3 = f\left(t_k + \frac{h}{2}, x_k + \frac{h}{2}f_2, y_k + \frac{h}{2}g_2\right) \\ f_4 = f(t_k + h, x_k + hf_3, y_k + hg_3) \end{cases} \quad \begin{cases} g_1 = g(t_k, x_k, y_k) \\ g_2 = g\left(t_k + \frac{h}{2}, x_k + \frac{h}{2}f_1, y_k + \frac{h}{2}g_1\right) \\ g_3 = g\left(t_k + \frac{h}{2}, x_k + \frac{h}{2}f_2, y_k + \frac{h}{2}g_2\right) \\ g_4 = g(t_k + h, x_k + hf_3, y_k + hg_3) \end{cases} \tag{2.59}$$

The subscript k indicates the kth step of the iteration, and h represents the time interval of the iteration.

By employing the above algorithm, rate equation is solved at transient state. Figure 2.7 presents the typical turn-on characteristic of InGaAs nanolasers emitting at 1.5 μm. Damping oscillation is clearly observed within the first few nanoseconds before the nanolaser reaches a steady-state condition. The oscillation relaxation period is on the order

of tens of picoseconds indicating the maximum of laser modulation speed.

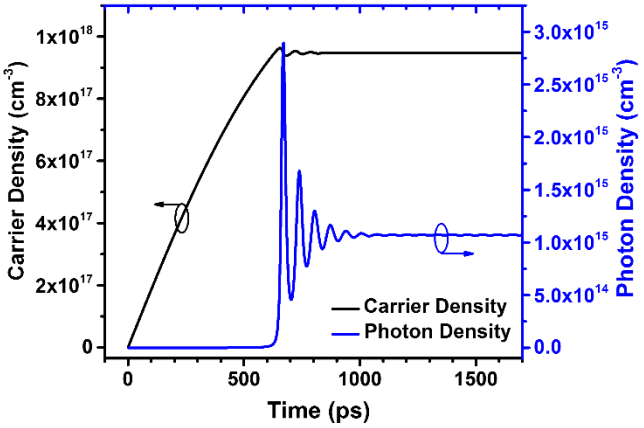

Figure 2.7 Turn-on characteristic of carrier and photon density of semiconductor nanolaser by solving transient rate equation.

Different from CW operation, the linewidth of nanolasers under pulse pumping is found to become broadened with the increase of excitation levels, rather than narrowed as predicted in (2.55). Such disparate performance can be explained by modeling the emission dynamics

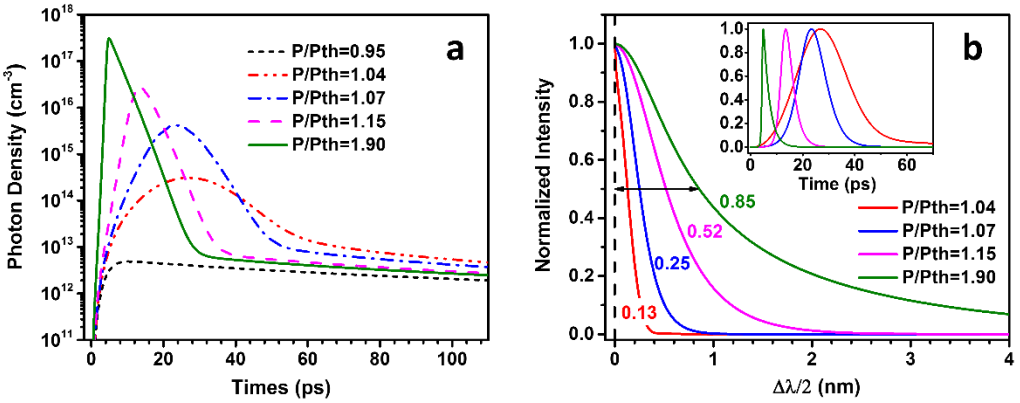

Figure 2.8 Emission dynamics of semiconductor nanolaser under pulse excitation (a) photon density in nanolaser cavity as function of time after single pulse excitation at t=0 for different excitation power (b) half linewidth of the Fourier transform of 4 curves above the threshold in (a). inset, normalized photon density as function of time above the threshold in (a)

of nanolasers via solving the transient rate equation. In the model, we assume that the

optical excitation pulse providing the initial carrier density takes the form [43],

$$P(t) = D \cdot \left(\frac{1}{\tau_{exc}}\right) \cdot \left(1.76 \times \frac{t}{\tau_{exc}}\right) \tag{2.60}$$

where D is the intensity factor and the τ_{exc} is the pulse duration. Figure 2.8 gives the calculation results of the emission dynamics of an InGaAs nanolaser. The calculation of the spontaneous emission rate and material gain used in rate equations is given by (2.30) and (2.24), respectively. The excitation pulse width in simulation is assumed to be 2 ps. As can be noticed from the results, under pulse operation, stronger excitation pulse is able to induce shorter output pulse in Fig. 2.8a as a result of faster stimulated emission process determined by stimulated lift time τ_{st}, where

$$\tau_{st} = \frac{1}{v_g \cdot g} \tag{2.61}$$

In (2.61), v_g is the group velocity and g is the material gain. According to the expression of τ_{st}, higher excitation power increases the material gain, which in turn decreases the stimulated emission lifetime, and therefore shortens the pulse width of the nanolaser emission, leading to an increment of spectral linewidth in frequency or wavelength domain. As the excitation increases from 1.04 to 1.9 of the threshold, the linewidth increases from 0.26 nm to 1.7 nm, as illustrated in Fig. 2.8b.

2.3 Waveguide and Cavity of Semiconductor Nanolasers

2.3.1 Refractive Index Guiding and Gain Guiding

As we know, reflection of light takes place at an interface where the discontinuity of the permittivity arises. In most cases, the permittivity of material is in real form and the discontinuity of the permittivity is contributed by the change of the refractive index,

defined as:

$$n = (\varepsilon_r|_{real})^{\frac{1}{2}} \tag{2.62}$$

Total internal reflection is such a phenomenon that the change of the refractive index occurs at the interface when light travels from a high refractive index medium to a low refractive index medium with an incident angle larger than the critical angle. Zero net energy of the light transmits through the interface into the low refractive index medium and the idea of light guiding within the high refractive index medium by total internal reflection is therefore inspired. By taking advantage of this idea, dielectric waveguides such as optical fibers have been widely used in communication fields due to their ultra-low power loss and other superiorities.

Besides refractive index change, if we write the permittivity into the full complex form, the discontinuity of the permittivity can also be created by the presence of its imaginary part. Since optical gain or loss in a medium is closely related to energy creation (or dissipation), applying material with optical gain (or loss) allows the material permittivity to have an imaginary term and thus is able to introduce the discontinuity. Reflection of light occurs at the interface from a transparent medium to a gain (or lossy) medium or vice versa, even though the refractive index of the two media could be identical. Thus, optical waveguiding can also be achieved by utilizing such reflection, named as gain guiding (or loss guiding). The expression of the complex relative permittivity $\tilde{\varepsilon}_r$ can be written as,

$$\tilde{\varepsilon}_r = \varepsilon_r' + i\varepsilon_r'' = (n + ik)^2 \tag{2.63}$$

where ε_r' and ε_r'' are the real and the imaginary part of complex permittivity, respectively, n is the refractive index and k is the extinction coefficient.

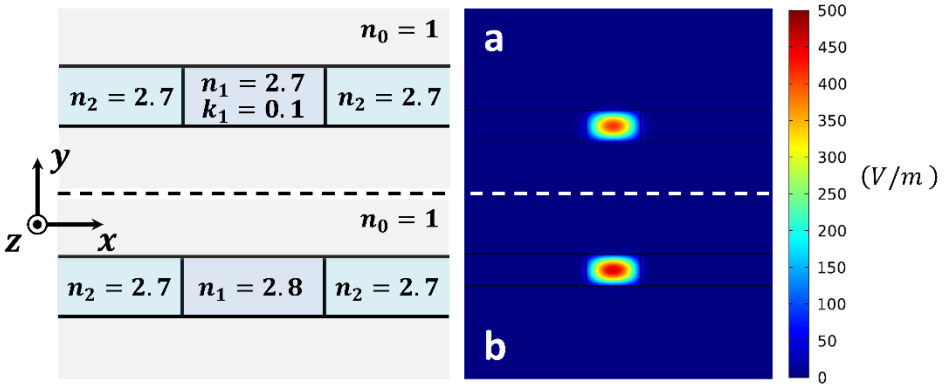

Figure 2.9 Simulation of gain guiding mode and refractive index guiding mode (a) calculated electric field distribution of gain guiding mode (b) calculated electric field distribution of refractive index guiding mode

Figure 2.9 gives the electric field distribution of a gain guiding mode versus a refractive index guiding mode simulated by COMSOL® RF Module. Although the refractive index n_1 on both sides in Fig. 2.9a is equal to n_2, the presence of extinction coefficient in the middle region due to optical gain mechanism enables the discontinuity of the permittivity. Mode can be therefore established and confined in the middle region as a result of the reflection of the light at the interface, which is equivalent to the index guiding mechanism in Fig. 2.9b. The confinement factors [45] of the modes in Fig. 2.9a and Fig. 2.9b are 99.5% and 99.7%, respectively, indicating that the gain guiding can also achieve high mode confinement, compared to the refractive index guiding.

2.3.2 Propagation Loss of Anti-Waveguiding Mode

In the previous section, we discussed the refractive index guiding by total internal reflection. Light can be confined in the high index layer (core layer) by total internal reflection without any net energy leakage into the low index layers (cladding layers). If we reverse the index arrangement, to make the low index layer in the middle “sandwiched”

between the two high index layers, light cannot be fully confined in the middle layer due to the breaks of the total internal reflection. The light energy will be partially refracted into the high index layer when the light is reflected at the interface from low index middle layer to the high index covering layer. No guiding mode can be established in the middle layer, as a result of the loss mechanism. Thus, light propagating in the aforementioned configuration can be named as an anti-waveguiding mode. If the optical gain is applied to compensate the loss, mode propagation can still be supported regardless of the anti-waveguiding property and the anti-waveguiding mode could possibly be used in many applications such as lasers. In this section, analytical expressions will be derived from the Maxwell equation and the propagation losses of the anti-waveguiding modes will be calculated by solving the transcendental equations in complex forms.

Assume the low index layer (refractive index $n_2 = 2.6$) in the middle is sandwiched by two high index layers (refractive index $n_2 = 2.7$), as shown in Fig. 2.10, and the light is propagating vertical to the paper.

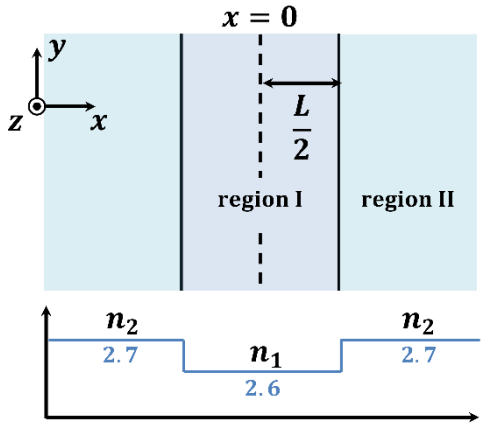

Figure 2.10 Configuration of anti-waveguiding structure.

The wave vector therefore in the z direction should be in a complex form due to the propagation loss, given by

$$\tilde{\beta}_z = \beta_z' + i\beta_z'' \tag{2.64}$$

where β_z' and β_z'' are the real and the imaginary part of the z component of the wave vector, respectively. The derivations of transcendental equations for both TM and TE cases are specified as follows:

i) TM Mode

Assume the fundamental TM mode in anti-waveguiding structure takes a standing waveform in region I (illustrated in Fig. 2.10), due to the partial reflection, and a propagating waveform in region II, due to the refraction. As a 2D problem, the expressions of the magnetic and electric fields are given by

$$H_{y1} = H_1 \cos\left(\tilde{\beta}_{x1} \cdot x\right) e^{-j\tilde{\beta}_z \cdot z} \tag{2.65}$$

$$H_{y2} = H_2 e^{-j[\tilde{\beta}_{x2} \cdot (x - L/2)]} e^{-j\tilde{\beta}_z \cdot z} \tag{2.66}$$

$$E_{z1} = \frac{j}{\omega\varepsilon_1}\frac{\partial H_{y1}}{\partial x} = \frac{-jH_1}{\omega\varepsilon_1}\tilde{\beta}_{x1} \sin\left(\tilde{\beta}_{x1} \cdot x\right) e^{-j\tilde{\beta}_z \cdot z} \tag{2.67}$$

$$E_{z2} = \frac{j}{\omega\varepsilon_2}\frac{\partial H_{y2}}{\partial x} = \frac{-jH_2}{\omega\varepsilon_2} \cdot j\tilde{\beta}_{x2} e^{-j[\tilde{\beta}_{x2} \cdot (x - L/2)]} e^{-j\tilde{\beta}_z \cdot z} \tag{2.68}$$

where the subscript 1 or 2 indicates the physical quantities in region I or II, respectively, and $\tilde{\beta}_{x1,2}$ is the component of the wave vector along the x direction in the respective region. The continuity of both the tangential electric and magnetic fields on the wall at $x = L/2$ gives the following boundary conditions,

$$H_{y1}\big|_{x=\frac{L}{2}} = H_{y2}\big|_{x=\frac{L}{2}} \tag{2.69}$$

$$E_{z1}\big|_{x=\frac{L}{2}} = E_{z2}\big|_{x=\frac{L}{2}} \tag{2.70}$$

Enforcing the above boundary conditions onto (2.65) - (2.68), we have

$$H_1 \cos\left(\tilde{\beta}_{x1} \cdot \frac{L}{2}\right) = H_2 \tag{2.71}$$

$$H_1 \frac{\tilde{\beta}_{x2}}{\varepsilon_1} \sin\left(\tilde{\beta}_{x1} \cdot \frac{L}{2}\right) = jH_2 \frac{\tilde{\beta}_{x2}}{\varepsilon_2} \tag{2.72}$$

Noticing the dispersion relations,

$$\beta_1^2 - \tilde{\beta}_{x1}^2 = \tilde{\beta}_z^2 \tag{2.73}$$

$$\beta_2^2 - \tilde{\beta}_{x2}^2 = \tilde{\beta}_z^2 \tag{2.74}$$

where $\beta_1^2 = \omega^2 \varepsilon_1 \mu_0$ and $\beta_2^2 = \omega^2 \varepsilon_2 \mu_0$, we then have the transcendental equation for TM mode as:

$$\varepsilon_2 \cdot \tilde{\beta}_{x1} \cdot \sin\left(\tilde{\beta}_{x1} \cdot \frac{L}{2}\right) = j\varepsilon_1 \sqrt{\beta_2^2 - \beta_1^2 + \tilde{\beta}_{x1}^2} \cdot \cos\left(\tilde{\beta}_{x1} \cdot \frac{L}{2}\right) \tag{2.75}$$

ii) TE Mode

Similar to TM mode, we can also list the expressions of the magnetic and electric fields for fundamental TE mode as:

$$E_{y1} = E_1 \cos(\tilde{\beta}_{x1} \cdot x) e^{-j\tilde{\beta}_z \cdot z} \tag{2.76}$$

$$E_{y2} = E_2 e^{-j[\tilde{\beta}_{x2} \cdot (x - L/2)]} e^{-j\tilde{\beta}_z \cdot z} \tag{2.77}$$

$$H_{z1} = \frac{-j}{\omega\mu} \frac{\partial E_{y1}}{\partial x} = \frac{jE_1}{\omega\mu} \tilde{\beta}_{x1} \sin(\tilde{\beta}_{x1} \cdot x) e^{-j\tilde{\beta}_z \cdot z} \tag{2.78}$$

$$H_{z2} = \frac{-j}{\omega\mu} \frac{\partial E_{y2}}{\partial x} = \frac{jE_2}{\omega\mu} \cdot j\tilde{\beta}_{x2} e^{-j[\tilde{\beta}_{x2} \cdot (x - L/2)]} e^{-j\tilde{\beta}_z \cdot z} \tag{2.79}$$

By applying the following boundary conditions at $x = \pm L/2$,

$$E_{y1}\big|_{x=\frac{L}{2}} = E_{y2}\big|_{x=\frac{L}{2}} \tag{2.80}$$

$$H_{z1}\big|_{x=\frac{L}{2}} = H_{z2}\big|_{x=\frac{L}{2}} \tag{2.81}$$

onto (2.76) - (2.69), we have

$$E_1 \cos\left(\tilde{\beta}_{x1} \cdot \frac{L}{2}\right) = E_2 \tag{2.82}$$

$$E_1 \tilde{\beta}_{x1} \sin\left(\tilde{\beta}_{x1} \cdot \frac{L}{2}\right) = jE_2 \tilde{\beta}_{x2} \tag{2.83}$$

After substituting $\tilde{\beta}_{x2}$ in terms of $\tilde{\beta}_{x1}$, we have

$$\tilde{\beta}_{x1} \cdot \sin\left(\tilde{\beta}_{x1} \cdot \frac{L}{2}\right) = j\sqrt{\beta_2^2 - \beta_1^2 + \tilde{\beta}_{x1}^2} \cdot \cos\left(\tilde{\beta}_{x1} \cdot \frac{L}{2}\right) \tag{2.84}$$

By solving $\tilde{\beta}_{x1}$ in equations (2.75) and (2.84), and applying the complex value into (2.73) to calculate $\tilde{\beta}_z$, the propagation loss is given by

$$\alpha = 2 \cdot \mathrm{Imag}(\tilde{\beta}_z) \tag{2.85}$$

Figure 2.11 shows the calculated propagation losses for both TM and TE modes as a function of the width of the low index middle layer. With the decrease of the middle width L, the propagation losses increase super exponentially for both TM and TE modes, due to the partial reflection of the light at the interface between region I and region II.

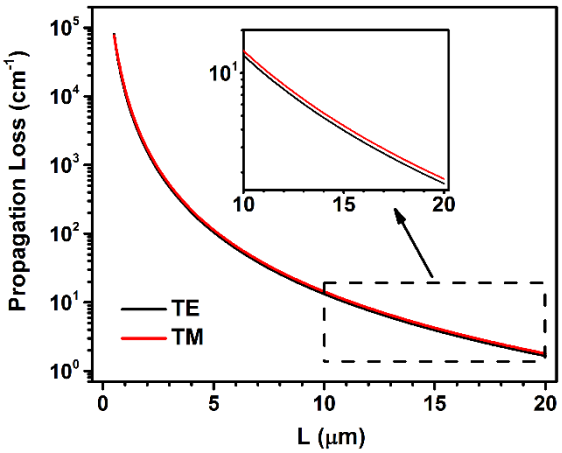

Figure 2.11 Propagation losses of anti-waveguiding modes as a function of the width of the low index middle layer.

Thus, to guarantee that the losses of anti-guiding modes are low enough to be overcome by material gain, the width of the low index layer should be sufficiently wide for real applications.

2.3.3 Estimation of Propagation Loss by Transferred Matrix Method

A more general situation than the previous section is that the middle core layer is "sandwiched" by cladding layers with lossy mediums on both sides and the refractive index of the core layer is either lower or higher than the cladding layers. To estimate the propagation loss in this general case, the transferred matrix method is used to minimize the calculation complexity while still providing satisfactory accuracy by the estimation.

Figure 2.12 describes the model, where the middle core layer with the refractive index n_1 and the layer width L, is covered by the two lossy media with the refractive index n_2 and the extinction coefficient k_2. Light is propagating in this 2D structure, with the propagation direction along the z axis (vertical to the paper). Two fundamental modes,

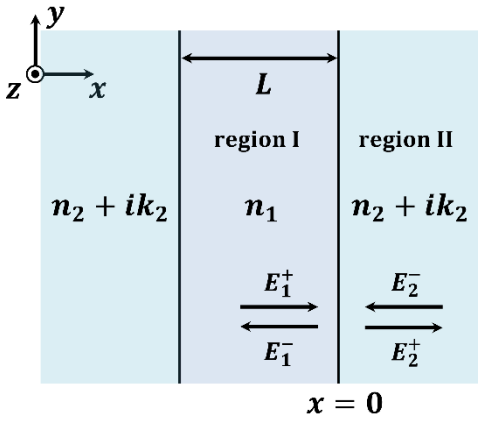

Figure 2.12 Configuration of the transfer matrix model that the middle core layer is covered by two loss mediums.

TM and TE, are discussed in the following paragraphs by transfer matrix approaches, respectively:

i) TM Mode

In contrast to the field forms that we used in the previous section, here we take the vector potential of the field in region I (the core layer) as the superposition of two

propagating lights in opposite directions. For fundamental TM mode in 2D structure, the vector potential $\boldsymbol{F}$ equals to zero and the vector $\boldsymbol{A}$ only has x component [45], written as:

$$\begin{cases} \boldsymbol{F} = 0 \\ \boldsymbol{A} = \hat{\boldsymbol{a}}_x A_x(x,\, z) = \hat{\boldsymbol{a}}_x \left(A^+ e^{-j\tilde{\beta}_x \cdot x} + A^- e^{j\tilde{\beta}_x \cdot x}\right) e^{-j\tilde{\beta}_z \cdot z} \end{cases} \tag{2.86}$$

Two non-zero items, the y-component of the magnetic field and the z-component of the electric field, are given by

$$H_y = \frac{1}{\mu} \cdot \frac{\partial A_x}{\partial z} = -j\frac{\tilde{\beta}_z}{\mu}\left(A^+ e^{-j\tilde{\beta}_x \cdot x} + A^- e^{j\tilde{\beta}_x \cdot x}\right) e^{-j\tilde{\beta}_z \cdot z} \tag{2.87}$$

$$E_z = j\frac{1}{\omega\varepsilon} \cdot \frac{\partial H_y}{\partial x} = j\frac{\tilde{\beta}_z}{\omega\varepsilon\mu}\left[A^+\left(-\hat{\beta}_x\right) e^{-j\tilde{\beta}_x \cdot x} + A^-\left(\tilde{\beta}_x\right) e^{j\tilde{\beta}_x \cdot x}\right] e^{-j\tilde{\beta}_z \cdot z} \tag{2.88}$$

Substituting the boundary conditions of the continuity at $x = 0$, where $H_{y1} = H_{y2}$ and $E_{z1} = E_{z2}$, we have

$$-j\frac{\tilde{\beta}_z}{\mu}(A_1^+ + A_1^-) e^{-j\tilde{\beta}_z \cdot z} = -j\frac{\tilde{\beta}_z}{\mu}(A_2^+ + A_2^-) e^{-j\tilde{\beta}_z \cdot z} \tag{2.89}$$

$$j\frac{\tilde{\beta}_z}{\omega\mu\varepsilon_1}\left[A_1^+\left(-\tilde{\beta}_x\right) + A_1^-\left(\tilde{\beta}_x\right)\right] e^{-j\tilde{\beta}_z \cdot z} = j\frac{\tilde{\beta}_z}{\omega\mu\varepsilon_2}\left[A_2^+\left(-\tilde{\beta}_x\right) + A_2^-\left(\tilde{\beta}_x\right)\right] e^{-j\tilde{\beta}_z \cdot z} \tag{2.90}$$

After further simplification, the equations reduce to:

$$\begin{pmatrix} A_1^+ \\ A_1^- \end{pmatrix} = \frac{\varepsilon_1}{2} \cdot \begin{pmatrix} \frac{\tilde{\beta}_{x1}/\varepsilon_1 + \tilde{\beta}_{x2}/\varepsilon_2}{2\tilde{\beta}_{x1}} & \frac{\tilde{\beta}_{x1}/\varepsilon_1 - \tilde{\beta}_{x2}/\varepsilon_2}{2\tilde{\beta}_{x1}} \\ \frac{\tilde{\beta}_{x1}/\varepsilon_1 - \tilde{\beta}_{x2}/\varepsilon_2}{2\tilde{\beta}_{x1}} & \frac{\tilde{\beta}_{x1}/\varepsilon_1 + \tilde{\beta}_{x2}/\varepsilon_2}{2\tilde{\beta}_{x1}} \end{pmatrix} \begin{pmatrix} A_2^+ \\ A_2^- \end{pmatrix} \tag{2.91}$$

According to the transfer matrix method, the electromagnetic waves have energy flow exchanges at the interface $x = 0$ (in Fig. 2.12), obeying,

$$\begin{pmatrix} E_1^+ \\ E_1^- \end{pmatrix} = \begin{pmatrix} 1/t_{ab} & r_{ab}/t_{ab} \\ r_{ab}/t_{ab} & 1/t_{ab} \end{pmatrix} \begin{pmatrix} E_2^+ \\ E_2^- \end{pmatrix} \tag{2.92}$$

which can also be written as:

$$\begin{pmatrix} A_1^+ \\ A_1^- \end{pmatrix} = \frac{\varepsilon_1}{\varepsilon_2} \begin{pmatrix} 1/t_{ab} & r_{ab}/t_{ab} \\ r_{ab}/t_{ab} & 1/t_{ab} \end{pmatrix} \begin{pmatrix} A_2^+ \\ A_2^- \end{pmatrix} \tag{2.93}$$

where t_{ab} is the transmission coefficient and r_{ab} is the reflection coefficient. The comparison of two equations (2.92) and (2.93) leads to

$$r_{ab} = \frac{\frac{\tilde{\beta}_{x1}}{\varepsilon_1} - \frac{\tilde{\beta}_{x2}}{\varepsilon_2}}{\frac{\tilde{\beta}_{x1}}{\varepsilon_1} + \frac{\tilde{\beta}_{x2}}{\varepsilon_2}} \tag{2.94}$$

The reflection of the fundamental TM mode at the interface from region I to region II can, therefore, be written as:

$$R = |r_{ab}|^2 = \left| \frac{\frac{\tilde{\beta}_{x1}}{\varepsilon_1} - \frac{\tilde{\beta}_{x2}}{\varepsilon_2}}{\frac{\tilde{\beta}_{x1}}{\varepsilon_1} + \frac{\tilde{\beta}_{x2}}{\varepsilon_2}} \right|^2 \tag{2.95}$$

ii) TE Mode

Similarly, for fundamental TE mode, the vector potential $\boldsymbol{A}$ equals to zero and the vector $\boldsymbol{F}$ only has the *x* component [45], written as:

$$\begin{cases} \boldsymbol{A} = 0 \\ \boldsymbol{F} = \hat{\boldsymbol{a}}_x F_x(x, z) = \hat{\boldsymbol{a}}_x \left(F^+ e^{-j\tilde{\beta}_x \cdot x} + F^- e^{j\tilde{\beta}_x \cdot x} \right) e^{-j\tilde{\beta}_z \cdot z} \end{cases} \tag{2.96}$$

The *y*-component of electric field and the *z* component of the magnetic field are given by

$$E_y = -\frac{1}{\varepsilon} \cdot \frac{\partial F_x}{\partial z} = j\frac{\tilde{\beta}_z}{\varepsilon} \left(F^+ e^{-j\tilde{\beta}_x \cdot x} + F^- e^{j\tilde{\beta}_x \cdot x} \right) e^{-j\tilde{\beta}_z \cdot z} \tag{2.97}$$

$$H_z = -j\frac{1}{\omega\mu} \cdot \frac{\partial E_y}{\partial x} = j\frac{\tilde{\beta}_z}{\omega\varepsilon\mu} \left[F^+ \left(-\tilde{\beta}_x \right) e^{-j\tilde{\beta}_x \cdot x} + F^- \left(\tilde{\beta}_x \right) e^{j\tilde{\beta}_x \cdot x} \right] e^{-j\tilde{\beta}_z \cdot z} \tag{2.98}$$

Applying the boundary conditions at $x = 0$, we have

$$j\frac{\tilde{\beta}_z}{\varepsilon_1} (F_1^+ + F_1^-) e^{-j\tilde{\beta}_z \cdot z} = j\frac{\tilde{\beta}_z}{\varepsilon_2} (F_2^+ + F_2^-) e^{-j\tilde{\beta}_z \cdot z} \tag{2.99}$$

$$j\frac{\tilde{\beta}_z}{\omega\varepsilon_1\mu} \left[F_1^+ \left(-\tilde{\beta}_{x1} \right) + F_1^- \left(\tilde{\beta}_{x1} \right) \right] = j\frac{\tilde{\beta}_z}{\omega\varepsilon_2\mu} \left[F_2^+ \left(-\tilde{\beta}_{x2} \right) + F_2^- \left(\tilde{\beta}_{x2} \right) \right] \tag{2.100}$$

The equations (2.99) and (2.100) can be further reduced to:

$$\begin{pmatrix} F_1^+ \\ F_1^- \end{pmatrix} = \frac{\varepsilon_1}{\varepsilon_2} \cdot \begin{pmatrix} \frac{\tilde{\beta}_{x1}+\tilde{\beta}_{x2}}{2\tilde{\beta}_{x1}} & \frac{\tilde{\beta}_{x1}-\tilde{\beta}_{x2}}{2\tilde{\beta}_{x1}} \\ \frac{\tilde{\beta}_{x1}-\tilde{\beta}_{x2}}{2\tilde{\beta}_{x1}} & \frac{\tilde{\beta}_{x1}+\tilde{\beta}_{x2}}{2\tilde{\beta}_{x1}} \end{pmatrix} \begin{pmatrix} F_2^+ \\ F_2^- \end{pmatrix} \tag{2.101}$$

The reflection of the TE mode can be written as:

$$R = |r_{ab}|^2 = \left| \frac{\tilde{\beta}_{x1}-\tilde{\beta}_{x2}}{\tilde{\beta}_{x1}+\tilde{\beta}_{x2}} \right|^2 \tag{2.102}$$

The value of $\tilde{\beta}_{x1}$ in reflection for both the fundamental TM mode in (2.95) and TE mode in (2.102) can be estimated through (2.75) and (2.84), respectively, and the value of $\tilde{\beta}_{x2}$ can be obtained by the dispersion relation (2.73) and (2.74). After arriving at the reflections, the propagation loss α can be estimated by the formula:

$$\alpha = -\frac{\ln R}{\frac{L}{v_{gx1}} \cdot v_{gz}} \tag{2.103}$$

where L is the width of the core layer, R is the reflection of the mode, v_{gx1} is the group velocity of the mode along the x direction in region I, and v_{gz} is the group velocity of the mode along the z direction. The physical meaning of (2.103) is that the value of absorption coefficient is exponential to the number of times when the mode bounces back and forward at the interfaces of both sides with the reflection of R, per unit of length where the mode propagates in the z direction.

Figure 2.13 gives the comparison of propagation loss between methods through numerical solutions and the transfer matrix estimation as a function of Δn, where $\Delta n = n_2 - n_1$. The value of extinction coefficient k_2 in region II is assumed to be 0.1. As presented in Fig. 2.13, a good agreement has been reached between the numerical solutions and the transfer matrix estimation. Slight deviations arise when n_2 becomes larger than n_1, which is a result of the error in the group velocities, introduced by the imaginary parts of

the wave vectors in the anti-waveguiding configuration.

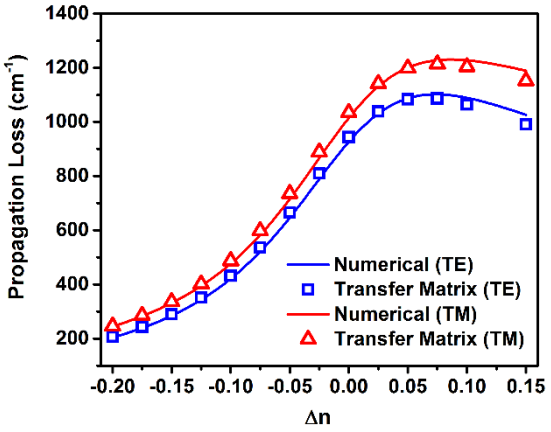

Figure 2.13 Estimation of the propagation loss by transfer matrix method compared to numerical approach.

2.3.4 Analytical Analysis of Rectangular Dielectric Waveguide

The most intensively discussed geometry in the following two chapters (Chapter 3 and 4) will be the NB or nanosheet structures. Therefore, it is necessary to carry out a careful study on lasing modes in such geometry, where we assume the mode propagates in length direction and distributes in width-thickness plane. A simplified model of the NB or nanosheet structures is rectangular dielectric waveguides. Thus, the modes in a rectangular dielectric waveguide will be studied analytically for a better understanding of the lasing modes in NB or nanosheet structures. Several references [45], [46] are consulted for the analytical derivation. Here, I only give the expression of TM^x mode for instance, however, TE^x mode would be easily deduced accordingly.

Assuming that the rectangular waveguide has index differences in the *x*-*y* plane and propagation direction in the *z* direction. For TM mode, the vector potential ***A*** only has the *x* component and the vector potential ***F*** equals to zero [45], where we have,

$$\begin{cases} \boldsymbol{A} = \hat{\boldsymbol{a}}_x A_x(x,\, z) \\ \boldsymbol{F} = 0 \end{cases} \tag{2.104}$$

The electrical and the magnetic fields are given by

$$\begin{cases} E_x = -j\frac{1}{\omega\mu\varepsilon}\left(\frac{\partial^2}{\partial x^2} + \beta^2\right) A_x \\ E_y = -j\frac{1}{\omega\mu\varepsilon}\frac{\partial^2 A_x}{\partial x \partial y} \\ E_z = -j\frac{1}{\omega\mu\varepsilon}\frac{\partial^2 A_x}{\partial x \partial z} \end{cases} \tag{2.105}$$

and

$$\begin{cases} H_x = 0 \\ H_y = \frac{1}{\mu}\frac{\partial A_x}{\partial z} \\ H_z = -\frac{1}{\mu}\frac{\partial A_x}{\partial y} \end{cases} \tag{2.106}$$

In order to get analytical solutions, the "Marcatili" approximation need to be applied [46], where we neglect the field distribution in the "shadow" areas, as shown in Fig. 2.14, to decouple the electric and magnetic fields.

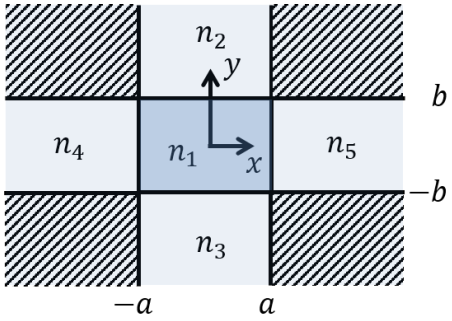

Figure 2.14 Configuration of rectangular dielectric waveguide for analytical solution.

Thus, we only need to calculate the field distribution in the rest of the five areas, where we assume:

$$\begin{cases} A_{x1} = A_1 \cos(\beta_{1x} \cdot x + \xi_1) \cos(\beta_{1y} \cdot y + \eta_1) e^{-j\beta_z \cdot z} \\ A_{x2} = A_2 \cos(\beta_{2x} \cdot x + \xi_2) \exp(\alpha_{2y} \cdot y) e^{-j\beta_z \cdot z} \\ A_{x3} = A_3 \cos(\beta_{3x} \cdot x + \xi_3) \exp(-\alpha_{3y} \cdot y) e^{-j\beta_z \cdot z} \\ A_{x4} = A_4 \exp(-\alpha_{4x} \cdot x) \cos(\beta_{4y} \cdot y + \eta_4) e^{-j\beta_z \cdot z} \\ A_{x5} = A_5 \exp(\alpha_{5x} \cdot x) \cos(\beta_{5y} \cdot y + \eta_5) e^{-j\beta_z \cdot z} \end{cases} \quad (2.107)$$

In (2.107), A_{xi} is the x component of vector potential A in respective index region; ξ_i and η_i are phase shifters; β_{ix} and α_{ix} is the propagation and decay constant in the x direction in respective index region.

Next, after we substitute (2.107) into (2.105) and (2.106), the H_y and E_z can be given by

$$\begin{cases} H_{y1} = \frac{1}{\mu}(-j\beta_z) A_1 \cos(\beta_{1x} x + \xi_1) \cos(\beta_{1y} \cdot y + \eta_1) \\ H_{y4} = \frac{1}{\mu}(-j\beta_z) A_4 \exp(-\alpha_{4x} \cdot x) \cos(\beta_{4y} \cdot y + \eta_4) \\ H_{y5} = \frac{1}{\mu}(-j\beta_z) A_5 \exp(\alpha_{5x} \cdot x) \cos(\beta_{5y} \cdot y + \eta_5) \end{cases} \quad (2.108)$$

and

$$\begin{cases} E_{z1} = j\frac{1}{\mu\varepsilon\omega}(-j\beta_z)\beta_{x1} A_1 \sin(\beta_{1x} x + \xi_1) \cos(\beta_{1y} \cdot y + \eta_1) e^{-j\beta_z z} \\ E_{z4} = j\frac{1}{\mu\varepsilon\omega}(-j\beta_z)\alpha_{x4} A_4 \exp(-\alpha_{4x} x) \cos(\beta_{4y} \cdot y + \eta_4) e^{-j\beta_z z} \\ E_{z5} = -j\frac{1}{\mu\varepsilon\omega}(-j\beta_z)\alpha_{x5} A_5 \exp(\alpha_{5x} x) \cos(\beta_{5y} \cdot y + \eta_5) e^{-j\beta_z z} \end{cases} \quad (2.109)$$

By enforcing the boundary conditions at $x = \pm a$, we have

$$\begin{cases} A_1 \cos(\beta_{1x} \cdot a + \xi_1) = A_4 \exp(-\alpha_{4x} \cdot a) \\ \frac{\beta_{1x}}{\varepsilon_1} A_1 \sin(\beta_{1x} \cdot a + \xi_1) = \frac{\alpha_{4x}}{\varepsilon_4} A_4 \exp(-\alpha_{4x} \cdot a) \\ A_1 \cos(\beta_{1x} \cdot a - \xi_1) = A_5 \exp(-\alpha_{5x} \cdot a) \\ \frac{\beta_{1x}}{\varepsilon_1} A_1 \sin(\beta_{1x} \cdot a - \xi_1) = \frac{\alpha_{5x}}{\varepsilon_5} A_5 \exp(-\alpha_{5x} \cdot a) \end{cases} \quad (2.110)$$

and

$$\beta_{1y} = \beta_{5y} = \beta_{4y} \stackrel{\text{def}}{=} \beta_y;\ \eta_1 = \eta_5 = \eta_4 \stackrel{\text{def}}{=} \eta \quad (2.111)$$

By eliminating the amplitude A, (2.110) can be simplified as:

$$\begin{cases} cot(\beta_{1x} \cdot a + \xi_1) = \frac{n_4^2}{n_1^2}\frac{\beta_{1x}}{\alpha_{4x}} \\ cot(\beta_{1x} \cdot a - \xi_1) = \frac{n_5^2}{n_1^2}\frac{\beta_{1x}}{\alpha_{5x}} \end{cases} \tag{2.112}$$

After noticing the relation,

$$\arctan(\cot\theta) = \frac{\pi}{2} - \theta + m\pi, \quad (m = 0,\ 1,\ 2,\ \dots) \tag{2.113}$$

(2.112) can be finally rewritten as:

$$2\beta_{1x}a = m\pi - \arctan\left(\frac{n_4^2}{n_1^2}\frac{\beta_{1x}}{\alpha_{4x}}\right) - \arctan\left(\frac{n_5^2}{n_1^2}\frac{\beta_{1x}}{\alpha_{5x}}\right), \ (m = 1,\ 2,\ 3,\ \dots) \tag{2.114}$$

To solve (2.114), one needs to employ the dispersion relation expressions,

$$\begin{cases} \beta_{1x}^2 + \beta_y^2 + \beta_z^2 = \omega^2\mu_0\varepsilon_0 \cdot n_1^2 \\ -\alpha_{4x}^2 + \beta_y^2 + \beta_z^2 = \omega^2\mu_0\varepsilon_0 \cdot n_4^2 \\ -\alpha_{5x}^2 + \beta_y^2 + \beta_z^2 = \omega^2\mu_0\varepsilon_0 \cdot n_5^2 \end{cases} \tag{2.115}$$

rewritten as:

$$\begin{cases} -\alpha_{4x}^2 = \omega^2\mu_0\varepsilon_0(n_1^2 - n_4^2) - \beta_{1x}^2 \\ -\alpha_{4x}^2 = \omega^2\mu_0\varepsilon_0(n_1^2 - n_4^2) - \beta_{1x}^2 \end{cases} \tag{2.116}$$

After substituting (2.116) into (2.114), we can eventually solve the transcendental equation to obtain the values of β_{1x}, α_{4x} and α_{5x}.

Similarly, the H_z and E_x can be derived as:

$$\begin{cases} H_{z1} = \frac{1}{\mu}\beta_y A_1\, cos(\beta_{1x}x + \xi_1)\, sin\big(\beta_y \cdot y + \eta\big)e^{-j\beta_z z} \\ H_{z2} = -\frac{1}{\mu}\alpha_{2y} A_2\, cos(\beta_{2x}x + \xi_2)\, exp\big(\alpha_{2y} \cdot y\big)e^{-j\beta_z z} \\ H_{z3} = \frac{1}{\mu}\alpha_{3y} A_3\, cos(\beta_{3x}x + \xi_3)\, exp\big(-\alpha_{3y} \cdot y\big)e^{-j\beta_z z} \end{cases} \tag{2.117}$$

and

$$\begin{cases} E_{x1} = j\frac{1}{\mu\omega\varepsilon_1}(\beta_1^2 - \beta_{1x}^2)A_1\, cos(\beta_{1x}x + \xi_1)\, cos\big(\beta_y \cdot y + \eta\big)e^{-j\beta_z z} \\ E_{x2} = j\frac{1}{\mu\omega\varepsilon_2}(\beta_2^2 - \beta_{2x}^2)A_2\, cos(\beta_{2x}x + \xi_2)\, exp\big(\alpha_{2y} \cdot y\big)e^{-j\beta_z z} \\ E_{x3} = j\frac{1}{\mu\omega\varepsilon_3}(\beta_3^2 - \beta_{3x}^2)A_3\, cos(\beta_{3x}x + \xi_3)\, exp\big(-\alpha_{3y} \cdot y\big)e^{-j\beta_z z} \end{cases} \tag{2.118}$$

Further approximation needs to be made, since $\beta_1 \gg \beta_{1x}$, $\beta_2 \gg \beta_{2x}$, and $\beta_3 \gg \beta_{3x}$, which brings (2.118) into:

$$\begin{cases} E_{x1} = j\frac{\beta_1^2}{\mu\omega\varepsilon_1} A_1 \cos(\beta_{1x}x + \xi_1)\cos\big(\beta_y \cdot y + \eta\big)e^{-j\beta_z z} \\ E_{x2} = j\frac{\beta_2^2}{\mu\omega\varepsilon_2} A_2 \cos(\beta_{2x}x + \xi_2)\exp\big(\alpha_{2y} \cdot y\big)e^{-j\beta_z z} \\ E_{x3} = j\frac{\beta_3^2}{\mu\omega\varepsilon_3} A_3 \cos(\beta_{3x}x + \xi_3)\exp\big(-\alpha_{3y} \cdot y\big)e^{-j\beta_z z} \end{cases} \tag{2.119}$$

By enforcing the boundary conditions at $x = \pm b$, we have

$$\begin{cases} A_1 \cos\big(\beta_y \cdot b + \eta\big) = A_3 \exp\big(-\alpha_{3y} \cdot b\big) \\ \beta_y A_1 \sin\big(\beta_y \cdot b + \eta\big) = \alpha_{3y} A_3 \exp\big(-\alpha_{3y} \cdot b\big) \\ A_1 \cos\big(\beta_y \cdot b - \eta\big) = A_2 \exp\big(-\alpha_{2y} \cdot b\big) \\ \beta_y A_1 \sin\big(\beta_y \cdot b - \eta\big) = \alpha_{2y} A_3 \exp\big(-\alpha_{2y} \cdot b\big) \end{cases} \tag{2.120}$$

and

$$\beta_{1x} = \beta_{3x} = \beta_{2x} \stackrel{\text{def}}{\equiv} \beta_x;\ \xi_1 = \xi_2 = \xi_3 \stackrel{\text{def}}{\equiv} \xi \tag{2.121}$$

Again, by eliminating the amplitude A, (2.120) can be simplified as:

$$\begin{cases} \cot\big(\beta_y \cdot b + \eta\big) = \frac{\beta_y}{\alpha_{3y}} \\ \cot\big(\beta_y \cdot b - \eta\big) = \frac{\beta_y}{\alpha_{2y}} \end{cases} \tag{2.122}$$

By applying (2.113), (2.122) can be rewritten as:

$$2\beta_y b = n\pi - \arctan\left(\frac{\beta_y}{\alpha_{2y}}\right) - \arctan\left(\frac{\beta_y}{\alpha_{3y}}\right),\ \ (n = 1,\ 2,\ 3,\ \ \ldots) \tag{2.123}$$

The dispersion relation,

$$\begin{cases} \beta_x^2 + \beta_y^2 + \beta_z^2 = \omega^2\mu_0\varepsilon_0 \cdot n_1^2 \\ \beta_x^2 - \alpha_{2y}^2 + \beta_z^2 = \omega^2\mu_0\varepsilon_0 \cdot n_2^2 \\ \beta_x^2 - \alpha_{3y}^2 + \beta_z^2 = \omega^2\mu_0\varepsilon_0 \cdot n_3^2 \end{cases} \tag{2.124}$$

can be rewritten as:

$$\begin{cases} \alpha_{2y}^2 = \omega^2 \mu_0 \varepsilon_0 (n_1^2 - n_2^2) - \beta_y^2 \\ \alpha_{3y}^2 = \omega^2 \mu_0 \varepsilon_0 (n_1^2 - n_3^2) - \beta_y^2 \end{cases} \tag{2.125}$$

After substituting (2.125) into (2.123), we can eventually solve the transcendental equation to obtain the values of β_y, α_{2y} and α_{3y}.

Table 2.1 gives the comparison of effective indices of different TM modes calculated by COMSOL® and the transcendental equations analytically derived in this section. The rectangular dielectric waveguide is assumed to have a width of 750 nm and a height of 500 nm. The index of the waveguide is assumed to be 2.6 for instance. As can be noticed from the Table 2.1, the "Marcatili" method, by decoupling the fields in the *x* and the *y* direction, is capable of providing an accurate enough approximation. With the increase of mode order in general, field coupling between two directions becomes much stronger, resulting in a large difference of effective indices by COMSOL® and the "Marcatili" method.

Table 2.1 Comparison of effective indices of TM modes in rectangular dielectric waveguide

n_{eff}	TM^x_{11}	TM^x_{21}	TM^x_{12}	TM^x_{22}	TM^x_{31}	TM^x_{13}	TM^x_{32}
COMSOL®	2.5343	2.4614	2.4041	2.3262	2.3355	2.1736	2.1858
"Marcatili"	2.5344	2.4615	2.4043	2.3274	2.3355	21.740	2.1936
Relative Variation	0.039‰	0.041‰	0.083‰	0.52‰	0.001‰	0.18‰	3.6‰
n_{eff}	TM^x_{23}	TM^x_{41}	TM^x_{14}	TM^x_{51}	TM^x_{15}	TM^x_{42}	TM^x_{24}
COMSOL®	2.086	2.1454	1.8152	1.8791	1.2657	2.0036	1.7057
"Marcatili"	2.0887	2.1478	1.8159	1.8825	1.2682	1.9926	1.7128
Relative Variation	1.3‰	1.1‰	0.39‰	1.8‰	2.0‰	5.5‰	4.2‰

2.3.5 Analytical Analysis of 2D Circular Dielectric Cavity

Nano-ring lasers will be another important type of nanolasers discussed in this dissertation. Their simplified model, 2D circular dielectric cavities, will be analytically studied in this section.

The vector potentials of the fields in a 2D circular dielectric cavity, ψ^A and ψ^F, take the form:

$$\psi_m^A(\rho,\phi) = \begin{cases} A_i \cdot J_m(\rho n\beta)e^{im\phi} & (\rho < R) \\ A_o \cdot H_m^{(1)}(\rho\beta)e^{im\phi} & (\rho > R) \end{cases} \tag{2.126}$$

$$\psi_m^F(\rho,\phi) = \begin{cases} F_i \cdot J_m(\rho n\beta)e^{im\phi} & (\rho < R) \\ F_o \cdot H_m^{(1)}(\rho\beta)e^{im\phi} & (\rho > R) \end{cases} \tag{2.127}$$

where m is the angular order number, ρ and ϕ are the coordinates in a polar system, A_i, A_o, F_i and F_o are the amplitudes of the vector potentials inside and outside the circular cavity, J_m and $H_m^{(1)}$ are the Bessel function and the Hankel function of the first kind, respectively, β is the wave vector in 2D case and n is the refractive index inside the circular cavity.

The non-zero components of the electric and magnetic fields of TM modes are given by [45]

$$\begin{cases} E_\rho = -\frac{1}{\varepsilon}\frac{1}{\rho}\frac{\partial\psi_m^F}{\partial\phi} \\ E_\phi = \frac{1}{\varepsilon}\frac{\partial\psi_m^F}{\partial\rho} \\ H_z = -j\frac{\beta^2}{\omega\mu\varepsilon}\psi_m^F \end{cases} \tag{2.128}$$

and the non-zero components of the electric and magnetic fields of TE modes are given by

$$\begin{cases} H_\rho = -\frac{1}{\mu}\frac{1}{\rho}\frac{\partial \psi_m^A}{\partial \phi} \\ H_\phi = -\frac{1}{\mu}\frac{\partial \psi_m^A}{\partial \rho} \\ E_z = -j\frac{\beta^2}{\omega\mu\varepsilon}\psi_m^A \end{cases} \tag{2.129}$$

After substituting the boundary condition at $\rho = R$ (R is the diameter of circular cavity), where the tangential components of both the electric and magnetic fields obey the continuities, we have [47]

$$nJ_{m-1}(n\beta R)H_m^{(1)}(\beta R) - J_m(n\beta R)H_{m-1}^{(1)}(\beta R) = 0 \tag{2.130}$$

for TM mode and

$$nJ_m(n\beta R)H_{m-1}^{(1)}(\beta R) - J_{m-1}(n\beta R)H_m^{(1)}(\beta R) = \frac{m}{\beta R}\left(n - \frac{1}{n}\right)J_m(n\beta R)H_m^{(1)}(\beta R) \tag{2.131}$$

for TE mode. By solving β in (2.130) and (2.131), the solutions of TM and TE mode can be obtained, respectively. The quality factor Q of a certain mode can be further acquired by [48]

$$Q = \frac{Re(\beta nR)}{-2Im(\beta nR)} \tag{2.132}$$

Figure 2.15 presents the results of the analytical study of a 2D circular dielectric cavity. Figure 2.15a shows the electric field distribution of a TE_{17} mode, using (2.129), with a cavity diameter of 1.4 μm and the resonance wavelength of 1570 nm. A comparison between cavity quality factors calculated by using the finite-difference time domain (FDTD) method and the analytical expressions in (2.132) are demonstrated in Fig. 2.15b. The resonance wavelength in the comparison is close to 980 nm. As one may notice, for a circular cavity with a large diameter, it is very difficult to apply the FDTD method to get the quality factor accurately enough, even using very fine mesh space.

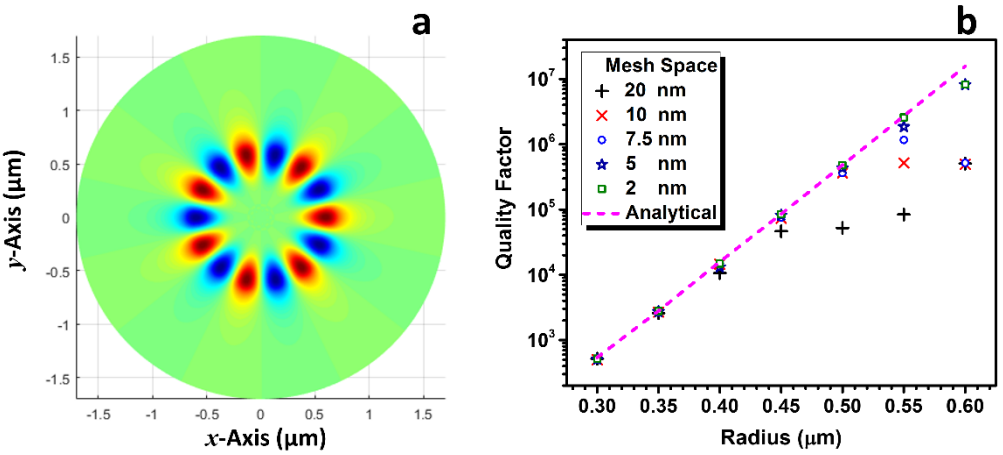

Figure 2.15 Analytical analysis of 2D circular dielectric cavity. (a) electric field distribution of a TE_{17} mode. (b) comparison of cavity Q calculation between FDTD and analytical approach.

Thus, the above analytical study is preferred for an analysis of circular dielectric cavities in 2D cases.

CHAPTER 3

TWO-COLOR LASING IN A MONOLITHIC *CdSSe* NANOSHEET

3.1 Introduction

A multi-color or multi-wavelength laser, by definition, is a device that provides discrete lasing lines at several wavelengths. Such laser devices have a wide range of applications like laser lighting and illumination [35], multicolor laser display [36], multicolor holographic imaging [51], biological and chemical sensing [38], and on-chip wavelength-division multiplexing [53], [54]. But to realize multi-wavelength lasing in a wide spectrum is fundamentally challenging. Lasing with multi-mode is one typical way to achieve multi-wavelength lasing. For a given composition of semiconductor material, the gain bandwidth is normally smaller than 30 nm [55]-[61], under a reasonable excitation condition. Mode separation of multiple modes or wavelength tunability of a single mode is thus limited by such a bandwidth.

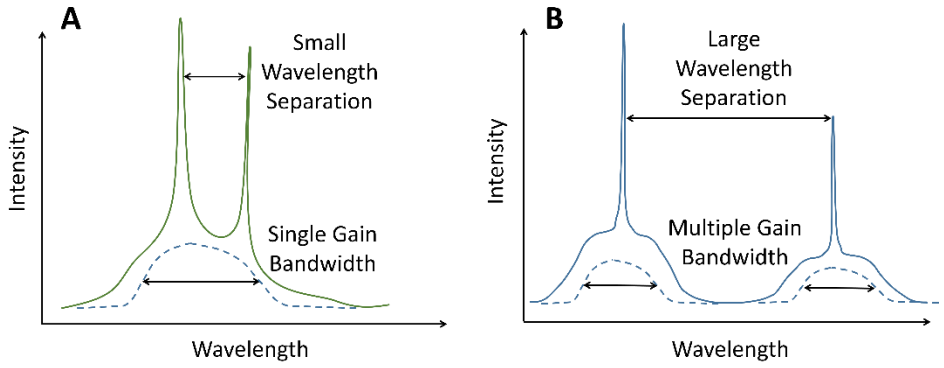

Figure 3.1 Schematic comparison of lasing spectra between (a) single composition material and (b) two heterogeneous composition material

Therefore, to have emission bandwidth significantly broader than that of a single composition, heterogeneous integration or growth of different semiconductors is necessary.

Figure 3.1 schematically shows the lasing spectrum difference between single composition semiconductor material (in Fig. 3.1a) and heterogeneously multiple composition semiconductor materials (in Fig. 3.1b). Obviously, with multiple gain bandwidth, the wavelength separation of multi-wavelength lasing can be greatly extended. However, the integration of heterogeneous materials will bring a large variation or significant mismatch of the lattice constants for semiconductors with distinct material compositions. Epitaxial growth of such structures on a single substrate becomes extremely difficult.

Semiconductor NWs and NBs grown using the metal-catalyzed VLS mechanism are promising candidates for multi-wavelength laser. One of the important features of NWs and NBs is their ability to grow different materials with different lattice constants without introducing too many defects to degrade optical properties. Since such features can automatically address the integration problem of heterogeneous materials and the lattice mismatch issue due to the intrinsic property of low dimension material, semiconductor NWs, and NBs or nanosheets have introduced great new possibilities for multi-color emission. With very different alloy compositions, NWs and NBs can achieve light emission in a wide range [62]-[66].

However, to make monolithic multi-color or dual-color lasers, merely heterogeneous integration or growth of different light-emitting materials together is not enough, even if such heterogeneous integration could be achieved by nanomaterial growth technique as mentioned. It is still a challenge to design a certain cavity structure to support multiple lasing wavelengths. This is because the short-wavelength light is strongly absorbed by the narrow gap semiconductors involved, such that only the long-wavelength light can eventually reach the threshold and become lasing. Therefore, appropriate design

of cavity structure to minimize the absorption of shorter-wavelength light by narrower bandgap material and to support dual wavelength feedback to simultaneously overcome the laser threshold is highly required

Various attempts have been made recently to overcome the challenges of extending the spectral range of light emission beyond the gain bandwidth of a single material and to achieve multi-color or dual-color lasing, such as by placing multiple NWs within a microfiber [67], by fabricating multi-section quantum dot distributed feedback lasers [68], or by using fast-switching of different dyes in a microfluidic channel [69]. These multi-color lasers are either achieved in separate devices, or with wavelength separation still limited within the gain bandwidth of a single semiconductor material. Gain materials such as organic semiconductor [70] and size dispersed quantum dots can have a larger gain bandwidth more than 50 nm [71]. However, multicolor lasing is still challenging in these materials due to the gain saturation and re-absorption problem in the in-line cavities.

In the following sections, I will present my solutions to multi-color lasers with the help of nanomaterials. Simultaneous red and green wavelength lasing has been achieved from a single monolithic CdSSe heterostructure nanosheet. The nanosheet was obtained by the bend-to-fracture method from a longer CdSSe heterostructure NB which was synthesized through a two-step chemical vapor deposition (CVD) approach. There is a spatial composition change from CdS-rich to CdSe-rich stripe along the width direction of the NB. The uniqueness of the nanosheet which enabled dual wavelength lasing is that it contains two rectangular, coupled cavities structure in a side-by-side arrangement. This arrangement will minimize the interaction between short wavelength mode and narrower band material, and therefore ensure, both of the two wavelength modes can reach their

respective lasing thresholds.

3.2 Theoretical Analysis of Side-by-side Cavity Structure

Although the NW or NB technology makes it possible to monolithically grow semiconductor material with two or even more different compositions together, bypassing the significant mismatch of the lattice constants and its related defect problems, it remains a question about how to properly design the cavity structure so that both short and longer wavelength can simultaneously achieve the lasing threshold, which is also a major issue for semiconductor multicolor lasing devices in a compact form.

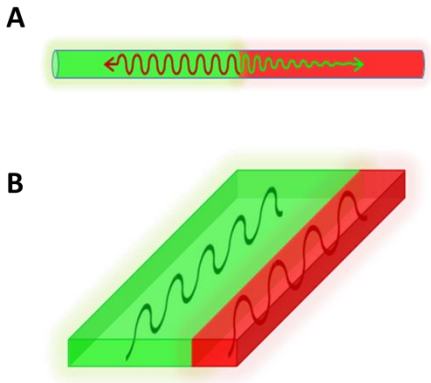

Figure 3.2 Sketch of two cavity configuration (a) In-line cavity structure. (b) Side-by-side cavity structure.

There are basically two possible configurations facilitated by NW or NB growth technology: i) in-line cavity structure, which is empowered through axial growth of heterostructure NW technique; and ii) side-by-side cavity structure, which is empowered through lateral growth of heterostructure NB or nanosheet technique. It is recently demonstrated that the in-line cavity structure has been realized in a single $CdS_{1-x}Se_x$ heterostructure NW [72], [73], as schematically shown in Fig. 3.2a. Such in-line cavity, however, suffers serious shortcomings for the multi-color lasing purpose, since the short-

wavelength light is strongly absorbed by the narrow bandgap materials and eventually only the long-wavelength light can reach the threshold. Theoretical calculation [74] has been applied showing that, without further manipulation, the loss of short-wavelength light by narrow bandgap materials is larger than 1×10^5 cm^{-1}. Comparing to in-line cavity, the side-by-side cavity would reduce the interaction between short wavelength light and narrow bandgap material, as schematically shown in Fig. 3.2b, and may provide a better opportunity to achieve two-color lasing. To confirm that intuitive idea, theoretical calculations were performed to estimate the loss of short wavelength light by narrow bandgap material in side-by-side cavity structure. We simplified the structure as two juxtaposed sides combined together (see Fig. 3.4a), with pure CdS part (emission wavelength at 496 nm) on the left and pure CdSe part (emission wavelength at 704 nm) on the right. The width of the CdSe segment is assumed to be fixed at 1.2 μm and the width of CdS segment is varying from 100 nm to 10 μm, in order to examine the variation range of the losses. All optical parameters used in calculation (Table 3.1) are obtained from Ref [75].

Table 3.1 Refractive indices and extinction coefficient of CdS and CdSe

Wavelength	CdS Segment	CdSe Segment
495 nm	2.826	2.706-0.3i
704 nm	2.427	2.824

Figure 3.3 shows the calculated loss of shorter wavelength as a function of the width of the CdS part for two fundamental mode E^x_{11} and E^y_{11}. Material gain has not been included in this calculation since pure loss mechanism needs to be investigated here without any gain compensation. It is clear that each of the modal loss increases in an exponential way as the CdS width decreases. For CdS width larger than 2 μm, the modal loss is less than 10 cm^{-1},

which is much smaller than the value, 1×10^5 cm^{-1} for in-line cavity structure as stated before, regardless of the length of the material.

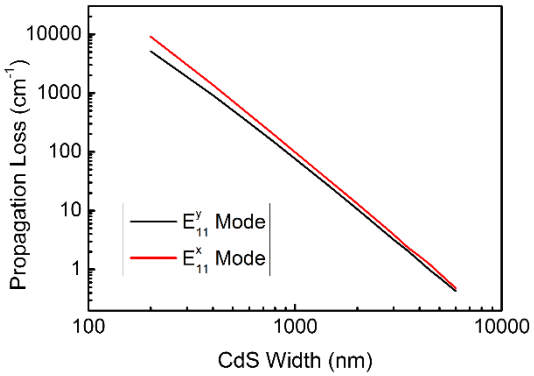

Figure 3.3 Calculation of modal losses at 496 nm versus width of CdS segment.

A rough conclusion can therefore be drawn that the side-by-side cavity is more inclined to support simultaneous two-color lasing than the in-line cavity, while a wider width of the CdS part is essential to reduce the loss of short-wavelength light.

To further demonstrate the better opportunity of simultaneous two-color lasing in the side-by-side cavity structure, extended 2D simulation has been performed by COMSOL® RF Module, with material gain taken into consideration additionally.

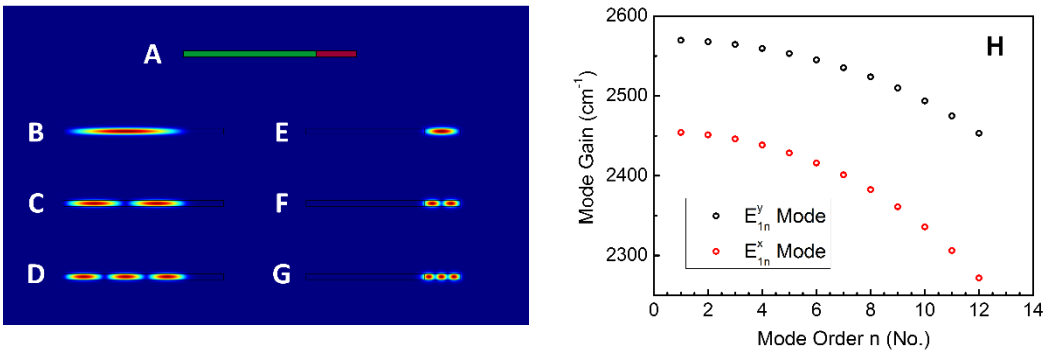

Figure 3.4 2D simulations of side-by-side structure. (a) The cross-section sketch of side-by-side structure. (b-d) Electric field distribution of first three modes at 496 nm. (e-g) Electric field distribution of first three modes at 704 nm. (h) Mode gain versus mode order.

The width of the CdS and the CdSe part are assumed to be 4 μm and 1.2 μm respectively and the thickness of the cavity is assumed to be 200 nm. The gain coefficients in active regions of both CdS and CdSe material are calculated at the carrier-density level of 1×10^{19} cm^{-3}.

Figure 3.4 shows the results of 2D simulation. The image of electric field distribution on the cross-section plane reveals that both the modes at 496 nm (Fig. 3.4b-d) and 704 nm (Fig. 3.4e-g) are well spatially separated and confined in their own active regions, which provide a more concrete evidence that the side-by-side cavity can reduce the interaction between the short wavelength light and the narrow bandgap material. Due to the relatively large width of both the segments compared to the wavelength in material, not only fundamental mode, but many higher order modes can also be supported in cavities. As examples, Fig. 3.4b-d and Fig. 3.4e-g demonstrate the first three order modes in the CdS part at 496 nm and in the CdSe part at 704 nm respectively. In addition, the difference of the modal gain among different order of mode has been calculated in Fig. 3.4h. It shows that the mode gain only slightly decreases with the mode order, which is attributed to the decline of the confinement factor and the increment of modal loss. Since the mode gain does not vary too much among different modes, it is reasonable that large number of modes can experience enough gain and reach the threshold to lase in the side-by-side structure. In summary, according to the above optical analysis, side-by-side cavity offers less interaction, lower loss of short wavelength to narrow bandgap material than in-line cavity, and thus appropriately caters to multi-color or two-color lasing purpose. Furthermore, wider width of the short-wavelength emitting part is necessary to prevent high level loss in side-by-side cavity.

Besides optical analysis, another important issue that needs to be settled is the carrier in larger bandgap material depleted by narrow bandgap material. Since we are monolithically creating different gain material together, heterostructure interface is inevitable. Thus, as typical Type-I band alignment across the CdS and CdSe interface,

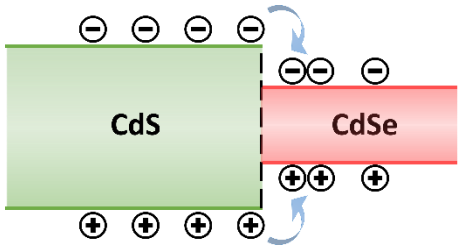

Figure 3.5 Illustration of carrier depletion by narrow bandgap material

electrons and holes in wider bandgap material (CdS) tend to cross the hetero-junction interface and fill into narrow bandgap material (CdSe) as indicated in Fig. 3.5.

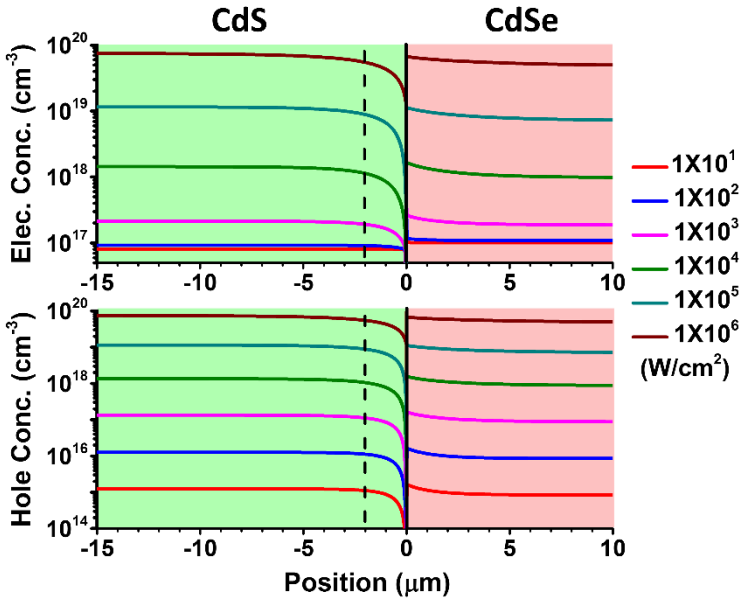

Figure 3.6 Electrons and holes depletion across CdS and CdSe heterojunction interface.

This mechanism might be significant at a high carrier density regime, where the depletion of carrier may influence the radiative recombination process in wider bandgap material and

therefore sharply decrease the material gain and increase the lasing threshold of the short wavelength light.

To systematically evaluate the impact of the carrier depletion, 2D Silvaco® simulation has been conducted at different optical injection levels. In the simulation, the bandgap values of CdS and CdSe material are 2.485 eV [76] and 1.756 eV [77], accordingly. The CdS and CdSe material are assumed to be both intrinsically n-type doped with doping concentration of 8×10^{16} cm^{-3} [78] and 1×10^{17} [79], respectively. Figure 3.6 shows the calculated electron and hole concentration near the CdS and CdSe heterojunction interface. Although under various pumping densities, most of the depletion happens only within 2 μm near the heterojunction interface, whereas away from the interface, electron and hole concentration keeps almost constantly without any significant depletion. The result again emphasizes the importance of sufficient segment width for the wider bandgap material to avoid the carrier depletion.

In conclusion, both optical and electric analysis above indicate that with sufficient segment width for wide bandgap material, side-by-side cavity structure is more catered to realizing multi-color lasing than in-line cavity structure.

3.3 Growth and Structural Characterization of CdSSe Heterostructure Nanobelts

To monolithically achieve side-by-side cavity structure, a lateral growth technique dominated by VS mechanism was employed to create CdSSe heterostructure NBs. The NBs were synthesized in a CVD system with CdS and CdSe powders as source materials and Si as substrate covered by 10 nm Au catalyst film. The synthesis process was through a two-step growth, in which CdS-rich sections were followed by the CdSe-rich sections

growth. In the first step, only CdS powder was thermally evaporated at 880 ℃ for one hour. Subsequently, CdSe source was introduced into the furnace, while the temperature was gradually lowered to 840 ℃ and held for 40 minutes to grow the CdSe-rich sections. The growth processes is similar to that of Ref. [80], but we reversed the growth sequence from CdSe/CdS to CdS/CdSe in order to achieve wide enough CdS-rich parts. Such sequential growth ensures a wide CdS-rich center section surrounded by CdSe-rich edges (see Fig. 3.7b). As discussed earlier, the large width of CdS-rich sections is especially significant as it needs to be wide enough to achieve sufficient optical confinement and less propagation loss for the shorter wavelength lasing modes.

Figure 3.7a shows the transmission electron microscopy (TEM) image of a CdSSe heterostructure nanosheet piece, which is from a longer as-grown NB sample by the bend-to-fracture method [81]. The nanosheet has a total width of 11.2 μm and length of 41.4 μm, with the thickness of ~200 nm. Figure 3.7b shows the real color photoluminescent (PL) image of the same heterostructure nanosheet. As seen in the image, the nanosheet consists of three stripes with green emission in the center (grown initially with CdS rich composition) and red/orange emission on both edges (grown subsequently with CdSe rich composition). Clearly the green stripe and the wider red/orange stripe form two rectangular, coupled cavities in a side-by-side arrangement. With proper end facets, the three stripes can form three coupled cavities capable of supporting various propagating modes along the length direction. Of particular interest are the two wider stripes (the green one in the center and the red one on the right side) which form two rectangular, coupled cavities, as also schematically shown in Figure 3.8c. Detailed characterization of the composition and

interface of the nanosheet was achieved by an energy dispersive X-ray spectroscopy (EDS) line scan across the nanosheet, as indicated by the white dashed line in Fig. 3.7a.

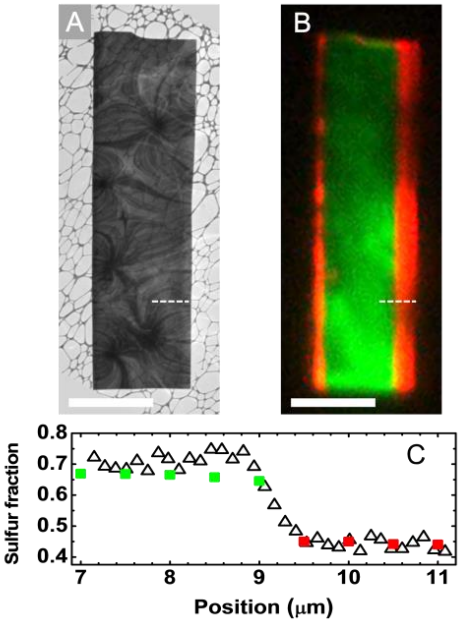

Figure 3.7 Structual characterization of a CdSSe heterostructure nanosheet (a) TEM image of the CdSSe lateral heterostructure nanosheet. (b) Real-color PL image of the same nanosheet. The scale bars in (a) and (b) are 10 μm. (c) Comparison of sulfur molar fraction between EDS scan (hallow triangles) and micro-PL scan (solid squares) along the white dashed line in (a) and (b).

Shown as hallow triangles in Fig. 3.7c, the sulfur molar fraction was plotted as a function of the spatial position across the width of nanosheet. The clear reduction of the sulfur molar fraction from ~70% to ~42% provides direct evidence of the existence of the heterojunction between the CdS-rich and CdSe-rich stripes. To confirm the EDS scan results, we also performed micro-PL scan measurements on the same nanosheet. The 405 nm excitation laser beam was focused down to a spot size less than 2 μm and was scanned across the width of the nanosheet to excite light emission from different points along the sample. The PL peak positions vary abruptly from green emission at 559 nm to orange emission at 602

nm at the location corresponding to the interface between stripes as identified by EDS. Furthermore, the sulfur molar fraction of the CdS_xSe_{1-x} ternary alloy can also be extracted from the wavelength of the PL peaks by band gap interpolation between the two binary endpoints, CdS and CdSe:

$$E_g(\mathrm{CdS}_x\mathrm{Se}_{1-x}) = xE_g(\mathrm{CdS}) + (1-x)E_g(\mathrm{CdSe}) \tag{3.1}$$

Due to the relaxations of the effective strain resulting from the single crystallinity of the nanosheet, here we neglect the bowing effect according to Ref. [82]. The filled squares plotted in Fig. 3.7c show the sulfur molar fraction calculated from the micro-PL scan measurement as described. The composition values are consistent between EDS and micro-PL scans.

3.4 Simultaneous Two-color Lasing in CdSSe Heterostructure Nanosheet

Figure 3.8a shows a PL image of another lateral heterostructure nanosheet. The dimensions of this nanosheet are 25.0 μm (length) × 17.4 μm (width) × 200 nm (thickness). The nanosheet was cleaved from a longer piece by the bend-to-fracture method [81]. By this method, high-quality end facets were created, which play the role of facet reflectors and define the laser cavities. The widths of the CdS-rich (green) and CdSe-rich (orange) sections are 14.8 μm and 2.6 μm, respectively. The PL emission peaks from the CdS-rich and CdSe-rich sections are at 546 nm (green) and 591 nm (orange), respectively. As shown in the PL image, there is broken nanosheet debris surrounding the nanosheet of interest, observable by the lighter orange areas within the belt and the excess green areas outside of the nanosheet perimeter.

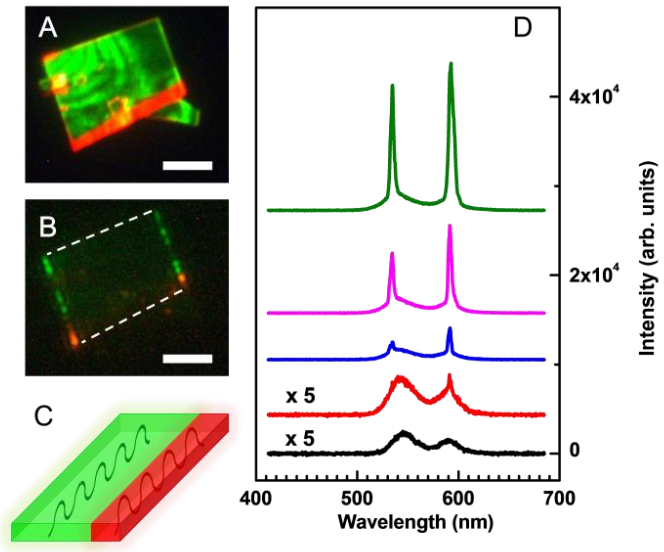

Figure 3.8 Real-color PL image of the nanosheet under low pumping power density at room temperature (a) and under 409 kW/cm^2 at 77K (b). The dashed lines in (b) denote the side edges of the nanosheet. The scale bars in (a) and (b) are 10 μm. (c) Schematic diagram of the nanosheet waveguide structures. (d) PL spectra at 77K under increasing levels of pumping power density of 77, 173, 241, 338 and 668 kW/cm^2 from bottom to top.

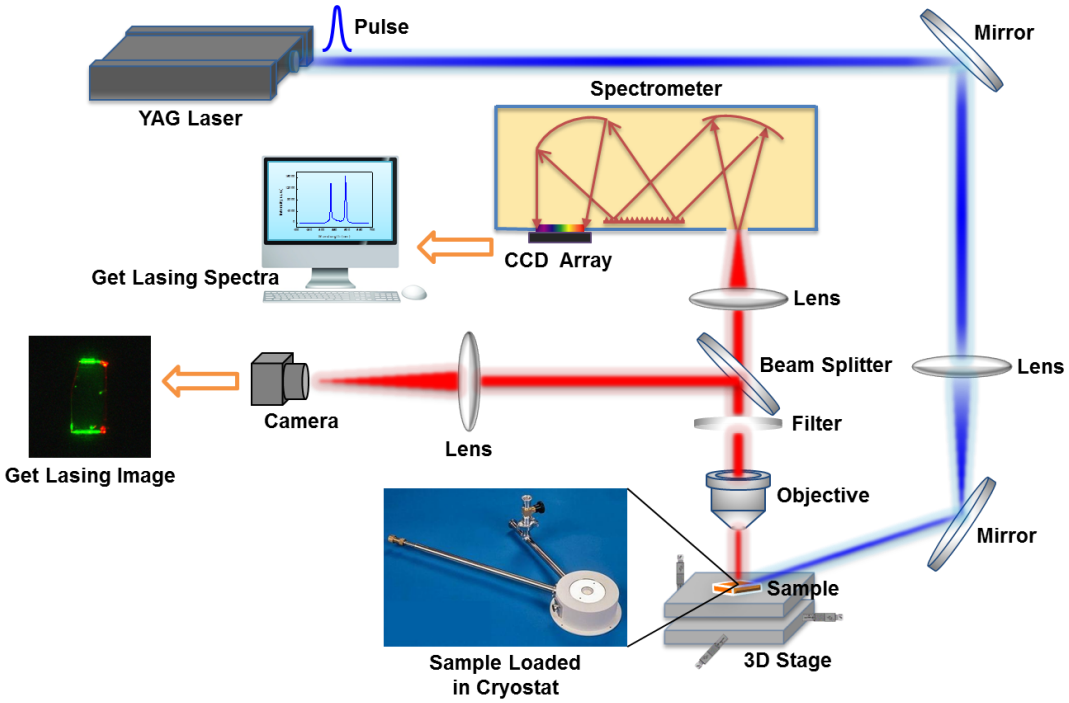

Figure 3.9 Experiment setup for two color lasing measurement.

To demonstrate the capability of dual-color lasing, we optically pump the nanosheet by the third harmonics of a Q-switched Nd: YAG laser (355 nm, 10 Hz, 9 ns) under increasing levels of pumping power, as schematically shown in Figure 3.9. The nanosheet was first placed onto a sapphire substrate by using the fiber tip and then loaded into a cryostat for low temperature measurement. The pump laser was focused onto a 120 μm × 60 μm ellipse on the sample at an angle of 60° of sample normal direction.

Figure 3.8b shows the real-color image of a single pulse induced dual-color lasing at a higher pumping level at 77 K. As can be seen clearly, the largely uniform emission of Fig. 3.8a is now replaced by the green and orange bright spots along the end facets, signifying the occurrence of lasing. Due to the gain-guiding and the refractive index guiding effect as mentioned in Chapter 2, green and orange emissions can be well-separated and confined in their own cavities, which is schematically shown in Fig. 3.8c. This is also reflected in Fig. 3.8b, where green and red emissions from the end facets are from the respective segments of CdS-rich or CdSe-rich materials. The interaction between the green and orange modes is minimized in this structure. As described in the introduction part of this chapter, short-wavelength emissions from the wide bandgap region (CdS rich) can be significantly absorbed by the narrow bandgap region (CdSe rich), which is a severe challenge for multi-wavelength lasing. Such absorption will increase the threshold for the short wavelength lasing, very often to a degree that is too high to achieve lasing. The side-by-side arrangement is an important geometry since it minimized such undesired absorption and allowed for reaching the respective lasing thresholds of both colors.

Figure 3.8d shows the single pulse PL spectra evolving with increasing pump power density. At lower pumping levels, only broadband spontaneous emissions from the CdS-

rich and CdSe-rich sections are observed. With increasing pump pulse power, a narrow peak appears at 592 nm at an excitation level of 173 kW/cm^2, indicating the onset of lasing for the orange color in the CdSe-rich section. The same is observed for green color lasing at 534 nm in the CdS-rich section when the excitation level reaches 241 kW/cm^2. The 58 nm separation of the two lasing peaks is much larger than the gain bandwidth of a typical Zn-Cd-S-Se semiconductor materials system, including CdS or CdSe. The narrowest linewidths of the two colors in Fig. 3.8d are around 4 nm, significantly broader than the typical linewidth of a single mode semiconductor laser. Detailed examination proves such broad linewidths of both sections under higher excitation intensities is due to the well-known multi-mode lasing behavior [83]-[87] and spectrometer resolution limitation. We performed high resolution measurement for the orange lasing peak to compare with the low resolution measurement (shown in Fig. 3.10) to examine the detailed mode features.

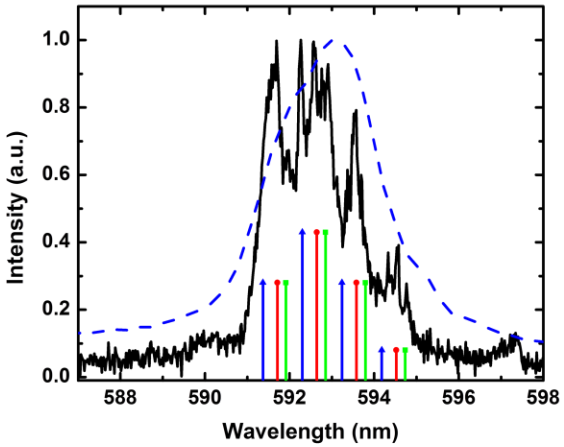

Figure 3.10 High resolution (black solid) and low resolution (blue dash) spectra of the orange lasing peak at 424 kW/cm^2. The green, red and blue vertical lines represent the wavelength of TE_{10}, TE_{20} and TE_{30} transverse modes. Each transverse mode has 4 associated longitudinal modes. The intensity of vertical lines of each group is calculated by the Gaussian convolution.

The high resolution measurement reveals that the wide peak in low resolution

measurement actually consists of multiple peaks with individual linewidths as narrow as 0.1-0.3 nm. The multiple lasing peaks can be divided into four groups and each group consists of a series of closely spaced peaks. The four groups of lasing peaks can be identified as the longitudinal modes of different orders with each group consisting of several closely spaced transverse modes. The wavelengths of three transverse modes TE_{10}, TE_{20}, TE_{30} and the corresponding longitudinal modes are also calculated and labeled in Fig. 3.10 for comparison. The mode spacing between the transverse modes is typically smaller than the longitudinal mode separation and can be as small as 0.2 nm, which almost reaches the resolution limitation of our spectrometer system. We attribute the multimode lasing features to the large size of the nanosheet structures in both directions, as compared to the wavelengths. With increasing pump intensity, more modes are excited above the threshold. Their close proximity to each other results in broader peaks as observed in low resolution measurements.

The LILO relations are presented in Fig. 3.11 on both linear and log-log scales to corroborate the spectral features and to further establish the lasing behavior at two distinct wavelengths. Shown in the inset of Fig. 3.11, the lasing intensity of both colors increase linearly with pump power after threshold (260 kW/cm^2 for the green modes and 230 kW/cm^2 for the orange modes). The total spontaneous emission output increases much more slowly than the lasing modes in the high excitation region, demonstrating the typical behavior associated with the lasing threshold. The log-log scale of the lasing output as a function of the excitation power features the well-known S-like behavior with three significantly different regions. At low pumping, the spontaneous emission is dominant, so the mode intensities increase linearly with slopes of 1.1 for orange and 1.3 for green.

Around the thresholds, the output intensities of both lasing modes show super-linear increases with slopes of 5.1 for orange and 4.7 for green. With a further increase of the excitation power, the slopes of both curves return to 1.1, indicating the above-threshold lasing operation of both colors.

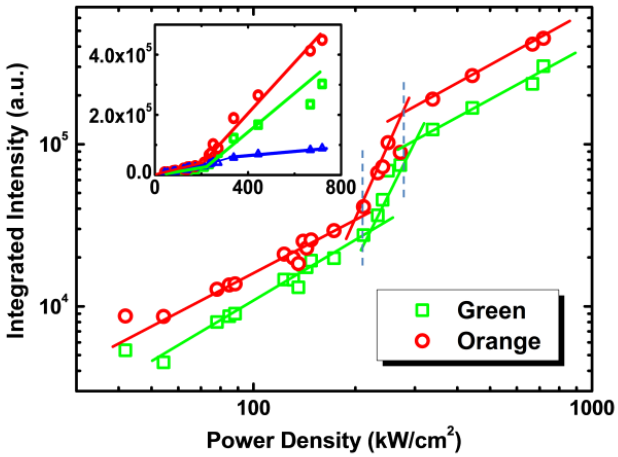

Figure 3.11 Output intensities of the two lasing colors versus pumping power density at 77 K in double-log scale. The inset shows the plots in linear scale, showing also the saturation of spontaneous emission (blue triangles).

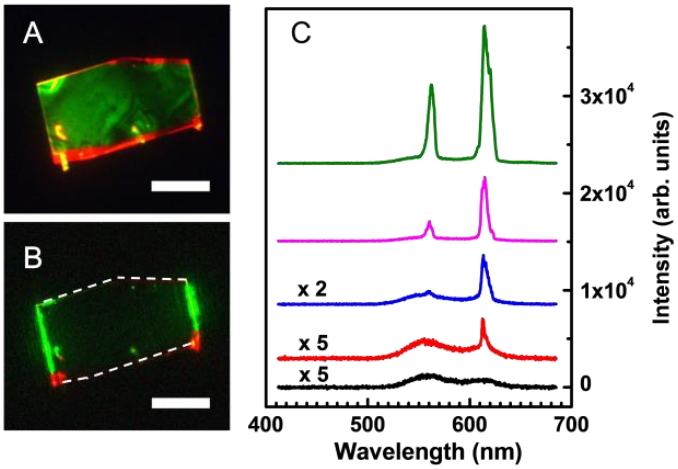

Figure 3.12 Real-color PL image of the nanosheet at RT under low pumping power density (a) and under 667 kW/cm^2 (b). The scale bars in (a) and (b) are 25 μm. (c) PL spectra at RT under increasing levels of pumping power density of 114, 184, 257, 310 and 546 kW/cm^2 from bottom to top respectively.

RT lasing has also been achieved on a larger nanosheet (66.5 μm in length, 33.0 μm in width, and 200 nm in thickness). As shown in Fig. 3.12a, the widths of the green and the wider orange stripes are around 30 μm and 3 μm, respectively. The real color image of the nanosheet above the threshold and PL spectra evolution are shown in Fig. 3.12b and 3.12c, respectively. The lasing wavelengths of the orange and green peaks are 613 nm and 562 nm, respectively, with a wavelength separation of 51nm. The estimated thresholds are 300 kW/cm^2 for the green modes and 227 kW/cm^2 for the orange modes. The lasing sequence for the two colors at RT is consistent with the result at 77K, both exhibiting higher thresholds for the green modes than for the orange modes. In addition, other features are also similar to the results demonstrated at low temperature. The wavelength separation of two lasing colors from CdSSe nanosheet can be further expanded by improving the growth methods.

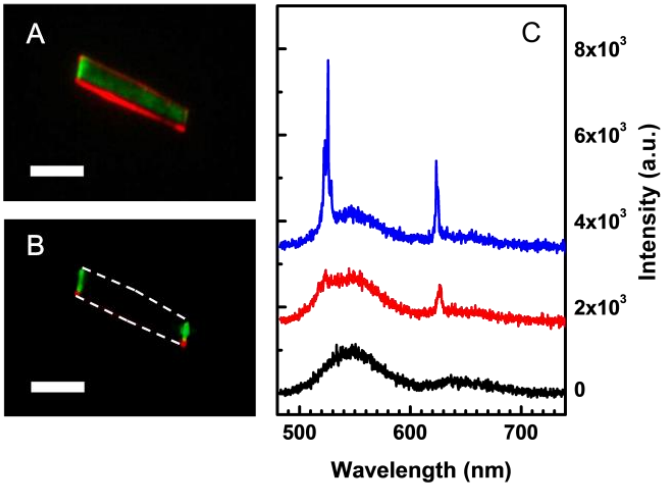

Figure 3.13 Real-color PL image of the nanosheet at RT by changing growth method under low pumping power density (a) and under high pumping power density (b). The scale bars in (a) and (b) are 10 μm. (c) PL spectra at RT under increasing levels of pumping power density of 196, 243 and 306 kW/cm^2 from bottom to top respectively.

The improved growing steps are the same as described previously, except that we totally

terminated the CdS source supply before introducing the CdSe source. By doing this, the ions exchange between sulfur and selenium can be minimized during the second step of the growth and as a result, the wavelength separation of two color lasing can be further expanded. Figure 3.13 demonstrates the two color lasing results of the nanosheet by changing the growth method. The lasing wavelengths are 526 and 623 nm, respectively, with a separation of 97 nm. The longer wavelength has now been fully expanded into the red color range. The dimensions of the nanosheet in Fig. 3.13a are 23.5 μm (length) × 5.2 μm (width) × 200 nm (thickness), much smaller than that of the nanosheets demonstrated before. As a result, less significant multimode behavior is shown in Fig. 3.13c. Other features are similar to the previous ones.

3.5 Summary

To summarize, the simultaneous lasing in two distinct visible colors from a single monolithic CdSSe lateral heterostructure nanosheet has been demonstrated. This was achieved by utilizing an important progress made in the growth of nano-materials using the metal-catalyzed VLS CVD growth. The key material enabler is the virtually substrate-insensitive growth of heterostructures with wide composition variation within a single nanosheet. The side-by-side geometry overcomes the challenging issues of multi-color lasing: the absorption of short-wavelength light by the narrow gap semiconductors. The dual-color lasing was identified by different measurements. The multimode lasing behavior has been clearly shown in high resolution measurements. One of the key quantities is the wavelength separation between the two colors as large as 97 nm in RT, much larger than the typical gain bandwidth of semiconductor materials (< 30 nm) in this wavelength range.

Lasing in such widely separated colors from a single semiconductor structure can be important for a variety of applications as mentioned at the beginning of the chapter.

CHAPTER 4

SIMULTANEOUS RGB LASING AND WHITE LASING IN A MONOLITHIC *ZnCdSSe* NANOSHEET

4.1 Introduction

As introduced in Chapter 3, multi-color lasers have a wide range of applications. Among all of those applications, laser illumination and multicolor display are poised to become the most profound and attractive area. As a solid state illuminant, lasers offer higher energy conversion efficiencies, higher output powers and potentially less energy consumption than white light-emitting diodes (LEDs) and other traditional illuminants. It has been recently demonstrated that illumination with four monochromatic lasers can also provide high color-rendering quality, visually equivalent to a continuous-spectrum white reference illuminant as seen by the human eye [49]. Therefore, a single monolithic semiconductor structure or device capable of lasing in RGB-wavelength to form a white laser as illuminating source would have a fundamental impact to the ultimate solution of efficient lighting. As a multicolor displayer, lasers, due to their high monochromaticity, can generate light of component colors with chromaticity coordinates approaching the boundary (known as spectral locus) of color space. Therefore, lasers can provide wider achievable color gamut (more than 90% of all colors perceptible to human eyes) than traditional display such as cathode ray tube (CRT), LED-backlit liquid crystal displayer (LCD) or organic LED (OLED) based on broadband incoherent light sources. Figure 4.1 shows the difference of color gamut of LED-backlit LCD, OLED and lasers. As it has been presented, with decrease of spectra width of three component colors, RGB (Fig. 4.1a), the chromaticity

coordinates of RGB move to the spectra locus of color space, resulting in the expansion of the triangle area, or color gamut (Fig. 4.1b) from originally 96% coverage of standard sRGB by LED-backlit LCD to 200% coverage of sRGB by laser, and leading to generating more achievable colors.

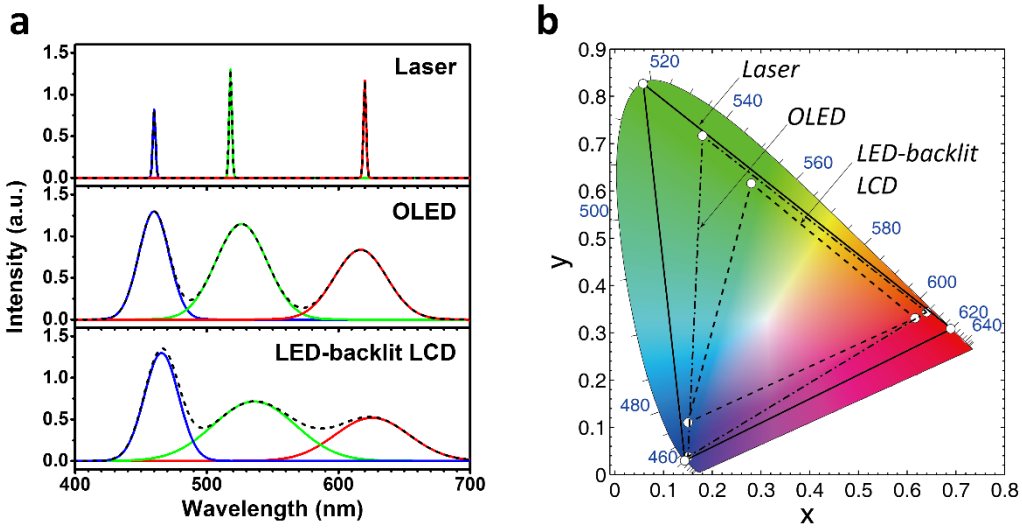

Figure 4.1 Comparison of spectra and color gamut of three different display system. (a) Spectra of LED-backlit LCD, OLED and laser (b) Color gamuts of LED-backlit LCD, OLED and laser.

The nature of lasers, such as high intensity and monochromaticity, caters to display demands in higher contrast ratio, better color saturation and a more vivid color.

Despite the great efforts made to achieve multi-color lasing using a variety of approaches, a single monolithic semiconductor laser capable of lasing with all three elementary colors, RGB, has not yet been realized due to several significant challenges. First, most of the previous approaches use non-semiconductor materials such as nonlinear optical crystals [88], rare-earth doped materials [89], dye-doped polymers [90] or liquids [69], or microfibers [67], as mentioned in Chapter 3. Such set-ups are bulky, inefficient and incompatible with electrical injection, an important ultimate requirement for many

applications. Second, semiconductor-based approaches [67], [68] combine several discrete devices in a heterogeneous manner, thus increasing the volume, complexity and cost of the overall system. Producing emissions covering all visible wavelengths in a single structure requires the growth of potentially dissimilar semiconductors into a monolithic structure with high crystal quality. This has been a goal pursued by the crystal growth community for decades and remains a challenging one, especially using conventional planar epitaxy techniques because of the large lattice mismatch involved. As an alternative to standard planar epitaxial structures, developments in nanotechnology over the last two decades have demonstrated the use of quantum dots [91] and NWs [64], [92]-[93] as means of producing emissions in a wide spectral range, but serious issues remain. For quantum dots made with solution-based techniques [94], control of their spatial distribution to avoid the absorption of short wavelength emission by narrow-gap dots remains difficult. More importantly, electrical injection remains a fundamental challenge for lasers, despite successful demonstrations of full-color LEDs [95], [96]. Beyond material growth, it is also critically important to realize a growth-compatible cavity structure in which the lasing of all three elementary colors can be supported simultaneously.

In the efforts to realize monolithic RGB lasers or white lasers as an ultimate goal, we have already demonstrated two-color lasing from a single monolithic two-segment CdSSe nanosheet in Chapter 3, and the side-by-side cavity geometry has been proven as the superior solution for two-color lasing rather than a longitudinal heterostructure. On the basis of the simultaneous green and red lasing, we have attained a third segment capable of blue lasing could be further added to a nanosheet structure to form a monolithic RGB laser or white laser. In order to achieve this third segment, a wider bandgap material is

required to be combined into the current ternary alloy system, CdSSe. As an ideal candidate, ZnS is the most compatible material known to alloy in various combinations with Cd, S and Se, and it would extend the bandgap to allow blue emission. However, the introduction of ZnS via nanomaterial growth mixing into a quaternary alloy will create two major problems, which are required to be settled. First, it is unclear whether the composition of the quaternary alloy in each color emitting segment is able to provide not only desired wavelength emissions but also the adequate index contrast for sufficient optical confinement, which minimizes the absorption of the short-wavelength light by narrow bandgap materials and support simultaneous RGB lasing in three-segment nanosheet structure. Second, due to the low vapor pressure and low supersaturation of ZnS, Zn-dominant blue emitting segments typically grow into NWs or thin nanoribbons form [97] with very high length–width aspect ratios [98]-[100]. This is why, up to date, ultraviolet and blue lasing in this material system has only been demonstrated in NWs [18] and nanoribbons [64] with high aspect ratios (>20). Such structures are intrinsically incompatible with the low-aspect-ratio nanosheet morphology for sufficient width of the blue and the green emitting segment required to achieve simultaneous RGB lasing. Whether it is possible to find a solution to overcome the intrinsic morphology of Zn-rich material with high length–width aspect ratios grown by low vapor pressure source and to make satisfactorily wide enough blue emitting segment to accommodate blue wavelength lasing.

In this chapter, I will present our efforts to realize monolithic semiconductor RGB and white lasers by resolving the two issues posed above. To settle the first issue regarding optical confinement, I have made theoretical analysis systematically with numerical

simulation to better understand the wave confined in three-segment nanosheet with the presence of index contrast and gain or absorption guiding. The results show, although the composition of quaternary alloy in each color emitting segment fails to support satisfactory index contrast in real part, it gives different indices in an imaginary part, and therefore makes complex index contrast sufficiently large enough for gain or absorption guiding in each segment of nanosheet. This guarantees the feasibility of simultaneous RGB lasing in three-segment nanosheet structure. To overcome the second issue and to produce desired morphology of blue emitting segments, we have developed a novel CVD growth method which has led to the successful growth of ZnCdSSe multi-segment heterostructure nanosheets with both appropriate morphology and composition, enabled by controlling the interplay of various growth mechanisms, including the VLS, VS mechanisms, and gas-phase dual-ion exchange reaction. Simultaneous RGB wavelength lasing has been achieved from a single monolithic ZnCdSSe multi-segment heterostructure nanosheet. By independently controlling the optical pumping power to each segment, we successfully demonstrate full-color tunable lasing over the entire triangular color gamut and white color lasing, in particular. The wavelength spans 191 nm which is the largest ever reported from a monolithic structure.

4.2 Theoretical Analysis of Feasibility of RGB Lasing in Three-segment Nanosheet

4.2.1 Band Lineup and Refractive Index of Three-segment Nanosheet

To investigate the feasibility of simultaneous RGB lasing, we consider a three-segment nanosheet as shown in Fig. 4.2. We assume that the three segments, emitting at 455, 530,

and 590 nm, correspond to the compositions of the three segments, $Zn_{0.7}Cd_{0.3}S_{0.3}Se_{0.7}$, $Zn_{0.4}Cd_{0.6}S_{0.15}Se_{0.85}$, and $Zn_{0.25}Cd_{0.75}S_{0.05}Se_{0.95}$, respectively.

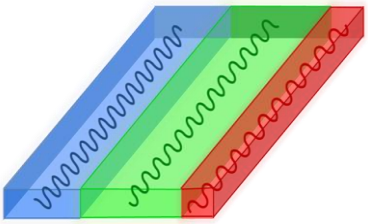

Figure 4.2 Schematic of a side-by-side cavity structure where modes are propagating mainly along the length direction within each segment.

To understand the details of waveguiding properties of the three-segment nanosheet structure, we need to determine first the bandgaps and refractive indices (the real parts of complex refractive indices) of these segments. As we know, the relative bandgap alignment or bandedge profiles between the neighboring segments determine the absorption of waves propagating in the structure, while the refractive index profile impacts the mode confinements within a given segment.

To determine the band edge lineups of the quaternary alloys across the hetero-junctions in the three-segment nanosheet using the atomic orbitals (LCAO) theory [101], we take the linear combination of all the involved binaries: ZnS, ZnSe, CdS, and CdSe, to calculate the valence band energies, E_v. Linear interpolations [82], [102] were also used to determine the band lineup of different quaternary alloy compositions, E_v, E_g (bandgap energy) and E_c (conduction band energy), summarized by the following equations:

$$E_v\left(Zn_xCd_{1-x}S_ySe_{1-y}\right) = E_v(ZnS)\cdot xy + E_v(CdSe)\cdot(1-x)(1-y)$$

$$+E_v(CdS)\cdot(1-x)y + E_v(ZnSe)\cdot x(1-y) \qquad (4.1)$$

$$E_g\left(Zn_xCd_{1-x}S_ySe_{1-y}\right) = E_g(ZnS)\cdot xy + E_g(CdSe)\cdot(1-x)(1-y)$$

$$+E_g(CdS)\cdot(1-x)y + E_g(ZnSe)\cdot x(1-y) \qquad (4.2)$$

$$E_c\left(Zn_xCd_{1-x}S_ySe_{1-y}\right) = E_c(ZnS)\cdot xy + E_c(CdSe)\cdot(1-x)(1-y)$$

$$+E_c(CdS)\cdot(1-x)y + E_c(ZnSe)\cdot x(1-y) \qquad (4.3)$$

For the refractive indices of the quaternary alloys, we also use linear interpolation from the binaries as follows:

$$n\left(Zn_xCd_{1-x}S_ySe_{1-y}\right) = n(ZnS)\cdot xy + n(CdSe)\cdot(1-x)(1-y) + n(CdS)\cdot$$

$$(1-x)y + n(ZnSe)\cdot x(1-y) \qquad (4.4)$$

Figure 4.3 shows the calculated band lineup and the profile of the refractive index (real part) along the width of the three-segment nanosheet. The band alignment at both interfaces (blue-green, green-red) are type I. The direct result of bandedge alignment across hetero-interfaces is the carrier confinement or redistribution, since carriers diffuse to locations with the lowest energy. In the red-emitting segment, carriers are confined in the interfacial region. For the blue-emitting segment, carrier confinement near the interface is poor due to the existence of lower bandgap material (the green emitting region) next to it. Based on measurements of ZnSSe thin film material in Ref [103], the estimated diffusion length or the depletion width of blue emitting material is less than 1-2 μm, which is consistent with the simulation results of the 2-μm depletion width calculated in Chapter 3, even at a highest pumping level. As long as the full width of the blue emitting segment is wide enough, i.e. up to 10 μm, merely minor issues with carrier diffusion or poor carrier confinement would occur. The green-emitting segment has the least partial carrier

confinement at the interface with the blue segment, and the carrier depletion only happens close to the red segment, with typical depletion width calculated as 2 μm. Such carrier depletion is also negligible as long as the segment width is adequate. In conclusion, from an electric point of view, the carrier confinement of the wide band gap semiconductor by the narrow band gap semiconductor should not be the primary concern, if the segment of the wide band gap semiconductor has sufficient width.

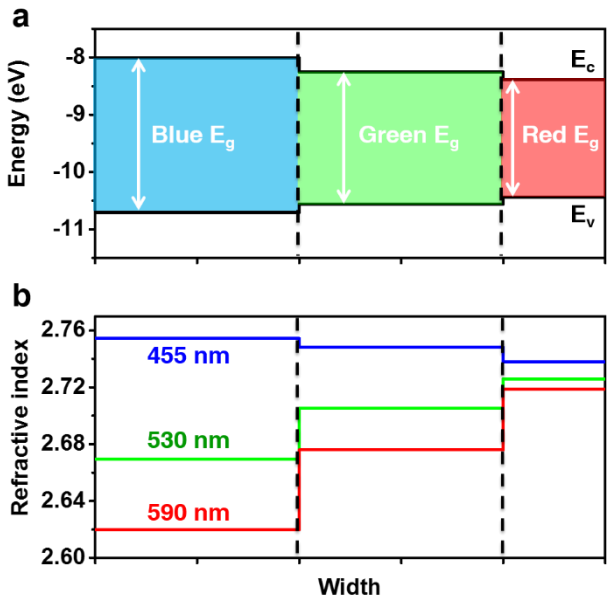

Figure 4.3 Band lineup and refractive index profiles of three segment nanosheet. (a) Band lineup across three segments of heterostructure nanosheet. (b) Refractive index profile at 455 nm, 530 nm and 590 nm wavelength, respectively.

According to the calculated refractive indices plotted in Fig 4.2b, we see that the blue and red wavelengths (the blue and red curves) have the highest refractive indices in their respective emission regions (left and right segments, respectively). Such index profiles should favor the confinement of the blue and the red light in the left and right segments. The refractive index profile at 530 nm is, however, highest in the red emitting

region. Thus it is important to know if and how well the green light is confined in the middle segment.

4.2.2 Analysis of Wave Confinement by Refractive Index Profile

To understand wave confinement in various cases of the index profile in such structures, we consider the waveguiding in more general cases. We consider a three-segment structure with index profiles shown in Fig. 4.4a. It is interesting to know if and how well modes are confined in the middle segment (core of the waveguide).

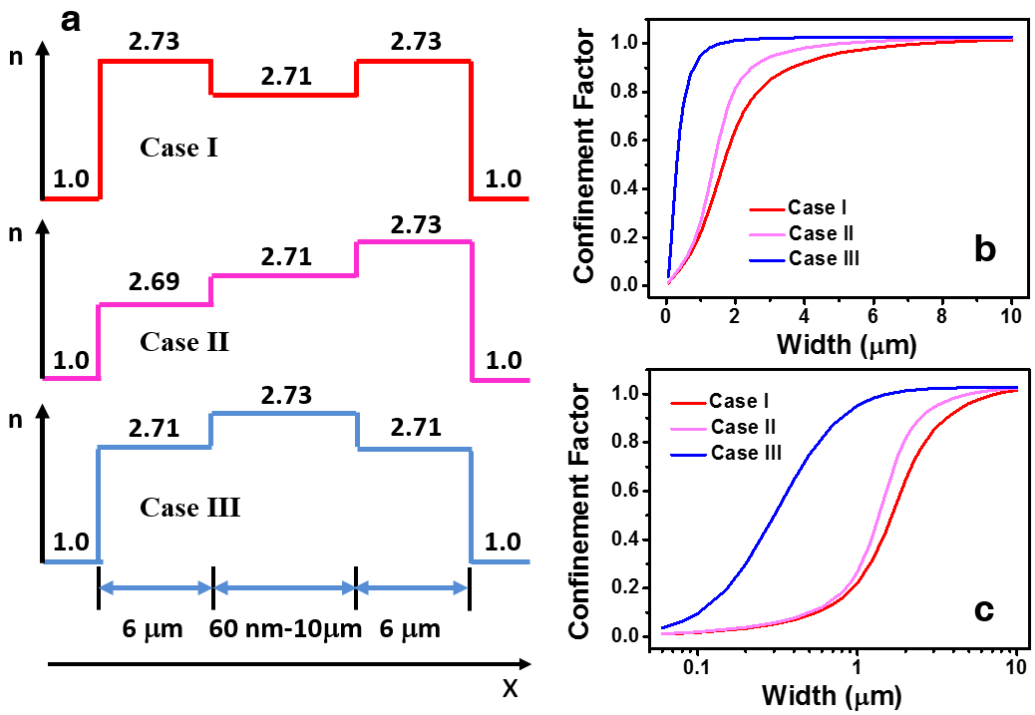

Figure 4.4 Refractive index profiles and the confinement factors in more general case. (a) Refractive index profiles across the three segments in a heterostructure nanosheet of the three cases considered, where values of the indices labeled above the profile. (b) and (c) Corresponding confinement factors for the middle segment for the three cases with against the width of the middle segment on linear scale (b) and log-scale (c).

To be more specific, we fix the widths of the two side segments (cladding layers of waveguide) and vary the width of the middle segment from a very small value of 0.2 μm to 10 μm. Case I is typically known as an anti-guiding waveguide where the index is lower in the core of the waveguide, whereas Case III corresponds to a standard waveguide design. Case II is an intermediate situation, namely a half anti-guiding waveguide, and is similar to our actual case presented in Fig. 4.3 for the green mode. We consider a problem where the modes are confined in the x and y direction and propagate into the paper plane (z direction). For laser cavities, the most important quantity is the confinement factor that describes how a mode is confined and amplified in the gain (core) layer of a waveguide. We calculate the confinement factor in the core (middle segment) of the waveguide using the expression [104]:

$$\Gamma_m = \frac{2\varepsilon_0 c n_b \iint dxdy|\boldsymbol{E}|^2}{\iint dxdy[\boldsymbol{E}\times\boldsymbol{H}^*+\boldsymbol{E}^*\times\boldsymbol{H}]} \tag{4.5}$$

Figure 4.4b and 4.4c show the calculated values of the confinement factors for the three cases. First of all, case III is the standard design of a core-cladding waveguide with a high index in the middle. The confinement factors approach one when the core layer is very wide and decreases to a quite large value (about 0.8), even when the core width is down to a half-micron. Case I is the opposite case of Case III, and is sometimes called anti-guided structure. But it is important to notice from Fig. 4.4 that the confinement factors for Case I and Case II also approach 1 when the width of the middle segment is very large (i.e. around 10 microns), even though the middle section in both of the cases does not have the largest index of refraction. This is because the degree of confinement of the modes in the middle segment is mostly determined by the reflectivities at the two interfaces in the case of large width, where propagational character dominates over refractive character. The reflection

coefficient depends mainly on the differences of the refractive indices on both sides of the interface. Therefore, the modes can still be well confined in the middle segment in Case I and II if the middle segment is sufficiently wide, despite not always having the largest index of refraction among the three segments. It is worth noting that the aforementioned theoretical analysis is performed under the presence of the real part of complex indices (refractive indices) only. With the consideration of imaginary parts in complex indices of the three-segment nanosheet in an actual situation, the reflectivities of middle segment at two interfaces will further increase, resulting in a better wave confinement and a lower requirement for adequate width of the middle segment.

4.2.3 Optical Gain and Absorption in Three-segment Nanosheet

In addition to refractive index contrast, the variation of imaginary parts in complex indices at segment interface can also provide optical confinement by intentionally presenting a spatial profile (or variation) of optical gain and/or absorption, where optical modes can be preferentially amplified or attenuated in differential spatial regions. As described in Chapter 2, such a confinement through gain or absorption profile is often called gain or absorption guiding. The variations of bandgaps and bandedges in the three-segment structure are shown in Fig. 4.3a. As it can be inferred, modes of blue and green wavelengths will be absorbed by the neighboring narrow bandgap segments near the interface regions. Such an absorption limits the spread of these modes into the neighboring regions and provides an additional confinement mechanism. In addition, modes in each of the three segments are amplified by the corresponding optical gain in their respective segments, which can also produce optical confinement, since the imaginary parts increase the

reflectivities of light at both interfaces. Therefore, to determine the mode confinement through the gain or absorption profile, we need to firstly determine the absorption or gain coefficients for each wavelength of the three-segment nanosheet.

To this end, the absorption or gain coefficients of three different wavelengths at 455, 530, and 590 nm were calculated for the corresponding three-segment quaternaries, $Zn_{0.7}Cd_{0.3}S_{0.3}Se_{0.7}$, $Zn_{0.4}Cd_{0.6}S_{0.15}Se_{0.85}$, and $Zn_{0.25}Cd_{0.75}S_{0.05}Se_{0.95}$ respectively, as shown in Fig. 4.3. All calculations were performed by a free-carrier model [105], assuming that interband transition is the dominant mechanism at RT. We neglect all other absorption mechanisms for simplicity.

Table 4.1 Band structure parameters used in calculation for absorption or gain coefficients

	*Band structure parameters of binary alloys			
	E_g (eV)	Δ_0 (eV)	m_e/m_0	m_{hh}/m_0
h-ZnS	3.77	0.088	0.28	0.49
h-ZnSe	2.83	0.478[107]	0.21[108]	0.60[108]
h-CdS	2.49	0.063	0.23	0.70
h-CdSe	1.76	0.405	0.12	0.45
	Band structure parameters of interpolated quaternary alloy			
	E_g (eV)	Δ_0 (eV)	m_e/m_0	m_{hh}/m_0
$Zn_{0.7}Cd_{0.3}S_{0.3}Se_{0.7}$	2.6949	0.3604	0.2011	0.5527
$Zn_{0.4}Cd_{0.6}S_{0.15}Se_{0.85}$	2.3101	0.38	0.1701	0.5259
$Zn_{0.25}Cd_{0.75}S_{0.05}Se_{0.95}$	2.0573	0.4070	0.1466	0.494

* All parameters for the binaries are taken from [106], except where referenced. Those for the quaternaries are obtained from linear interpolation. m_e and m_{hh} are electron and heavy hole masses respectively, while Δ_0 is split-off energy.

Bandgap energy E_g, spin-orbit splitting Δ_0, and effective mass of electrons m_e and holes m_{hh} in three different segments have been listed in Table 4.1, which are interpolated by Vegard's law with negligible bowing parameters [82]. The intrinsic carrier density for the absorption calculation was assumed to be less than 10^{17} cm^{-3}, and the carrier density for the gain calculation was assumed to be 10^{19} cm^{-3}, corresponding to a high level injection.

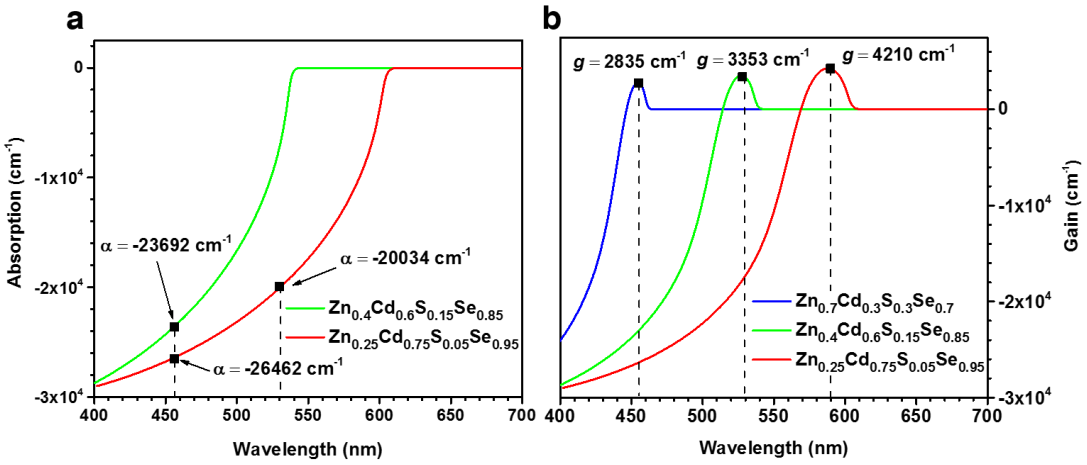

Figure 4.5 Calculated absorption and gain spectra. (a) Absorption spectra and coefficients of blue and green emission wavelengths by two quaternaries $Zn_{0.25}Cd_{0.75}S_{0.05}Se_{0.95}$ (red emitting segment) and $Zn_{0.4}Cd_{0.6}S_{0.15}Se_{0.85}$ (green emitting segment). (b) Gain spectra and coefficients of red, green and blue emissions in their associated quaternaries.

Table 4.2 Absorption and gain coefficients

	455 nm	530 nm	590 nm
$Zn_{0.7}Cd_{0.3}S_{0.3}Se_{0.7}$	2835 cm^{-1}	0	0
$Zn_{0.4}Cd_{0.6}S_{0.15}Se_{0.85}$	-23692 cm^{-1}	3353 cm^{-1}	0
$Zn_{0.25}Cd_{0.75}S_{0.05}Se_{0.95}$	-26462 cm^{-1}	-20034 cm^{-1}	4210 cm^{-1}

The calculated absorption and gain spectra of three quaternaries, $Zn_{0.7}Cd_{0.3}S_{0.3}Se_{0.7}$, $Zn_{0.4}Cd_{0.6}S_{0.15}Se_{0.85}$, and $Zn_{0.25}Cd_{0.75}S_{0.05}Se_{0.95}$, are shown in Fig. 4.5, while the absorption and gain coefficients at 455nm, 530nm and 590nm are listed in Table 4.2. The positive values represent gain and negative values represent absorption. According to Table 4.2, the red-emitting segment has the highest, and the blue-emitting segment has the lowest, material gain for their relevant emissions among all three segments, if equal pumping levels are assumed.

4.2.4 Analysis on Wave Confinement by Both Refractive Index and Gain (Absorption) Guiding in Three-segment Nanosheet

In the following discussion, I will show through simulation that distinct modes of blue, green and red emissions can be confined in their respective segments of the nanosheet, through combined mechanisms of both refractive index guiding and gain/absorption guiding. We have shown that the refractive index profile in Fig. 4.4 alone can serve as a good waveguide if the widths of wide band gap semiconductors, such as blue and green emitting segment, are sufficient. The additional gain/absorption guiding improves the wave confinement of the three-segment nanosheet even further. To demonstrate such combined effects more quantitatively, we perform 2D simulations in the cross sectional plane of the three-segment nanosheet structure by COMSOL®. The geometric parameters we used in the simulations are typically achievable in a two-segment CdSSe nanosheet as stated in the previous chapter. We set the thickness of the nanosheet to be 200 nm, and the width of the red and the green emitting segment to be 5 and 10 μm respectively. The width of the blue emitting segment is assumed to be 10 μm originally and then decreased down to 200 nm to examine the variation of modal gain (or loss). The emission wavelengths are 455, 530 and 590 nm, corresponding to alloy compositions of $Zn_{0.7}Cd_{0.3}S_{0.3}Se_{0.7}$, $Zn_{0.4}Cd_{0.6}S_{0.15}Se_{0.85}$, and $Zn_{0.25}Cd_{0.75}S_{0.05}Se_{0.95}$ respectively, as shown in Fig. 4.3. In the simulation, we use both the real and the imaginary part of a complex index instead of using a real part previously. The imaginary part of the refractive index *k*, also known as extinction coefficient, is related to the absorption or gain coefficient through:

$$k = \frac{\lambda}{4\pi} \cdot \alpha \tag{4.6}$$

where α is the absorption or gain coefficient and λ is the vacuum wavelength. We designate

k to be negative when it is absorption and positive when it is gain.

Table 4.3 Complex refractive indices

Wavelength	Blue segment	Green segment	Red segment
455 nm	2.754+0.01i	2.748-0.086i	2.738-0.096i
530 nm	2.669	2.705+0.014i	2.726-0.085i
590 nm	2.620	2.676	2.719+0.02i

Table 4.3 summarizes the calculated complex refractive indices of the three-segment nanosheet for three different wavelengths. The red, green and blue wavelengths all have optical gain in their associated color emitting segments, indicated by positive k values. The two shorter wavelengths, on the other hand, have absorption in longer wavelength-emission segments adjacently, indicated by negative k values.

Figure. 4.6 shows the final simulation results. With the presence of imaginary parts in complex indices due to gain and loss mechanisms, the mode distribution shown in Fig. 4.6a1-a6 reveals good confinement of all three wavelengths in their respective segments, especially the blue and green modes. It is worth noticing that the green modes at 530 nm show a strong optical confinement in Fig. 4.6a3 and 4.6a4, consistent with our earlier analysis in Section 4.2.2, despite the larger refractive index (real part of complex index) in the red-emitting segment than in the green-emitting segment. To further investigate the influence of gain or loss guiding out of the refractive index to the lasing threshold, the modal loss (material loss times the confinement factor) of the green mode at 530 nm was calculated as a function of the width of the green-emitting segment with different refractive indices of red emitting segment at 2.6, 2.75 and 2.9. From Fig. 4.6b, we can see that the modal loss reaches the maximum when the index of the red segment ($n_r = 2.75$) is close to that of the green segment ($n_g = 2.705$). When the index of red segment is lower than that of the green segment ($n_r = 2.6 < n_g$), less energy leaks into the absorbing red segment due

to refractive index guiding, similar to a regular waveguide, and therefore the modal loss is lower.

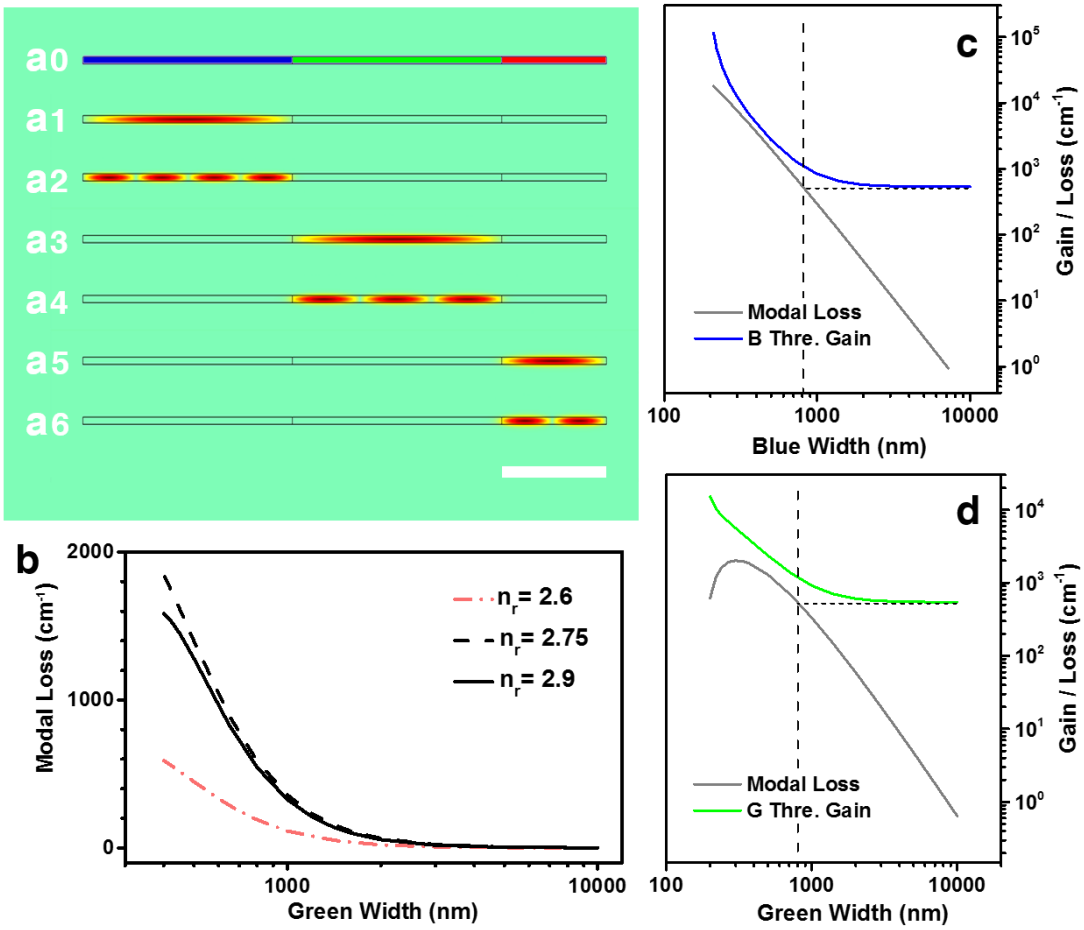

Figure 4.6 Theoretical analysis of mode profile and modal gain/loss with complex indices. (a0) Schematic of the cross-section of the side-by-side three-segment nanosheet structure in Fig. 4.2 (colors represent the emission color of each segment). Scale bar, 5 μm. (a1), (a3), (a5) The fundamental modes in the blue, green, and red emitting segments at 455 nm, 530 nm and 590 nm, respectively. (a2), (a4), (a6) The higher order Ex component dominated modes E_x^{14}, E_x^{13} and E_x^{12} in the blue, green, and red emitting segment at 455 nm, 530 nm, and 590 nm, respectively, where n in E_x^n indicates the number of maxima in E_x. (b) Modal absorption as a function of the width of the green segment in three cases of corresponding indices. (c), (d) The calculated relationship between segment width and threshold gain of the fundamental E_x^{11} modes, for the blue (455 nm) and the green (530 nm) emitting segments, respectively. For comparison, we also show the modal loss by the neighboring narrow gap segment in each case.

When the index of the red segment is higher than that of the green segment ($n_r = 2.9 > n_g$), the modal loss is also slightly lower than the case where n_r equals to 2.75, owing to the higher reflectivities by better index contrast, despite its half anti-guiding type. It is noticed that in all the cases, the modal loss decreases dramatically as the width of the green segment increases. When the width of the green segment is larger than 2 μm, the difference of modal loss among all the three cases is not noticeable. If the actual width of the green-emitting segment in a nanosheet structure is larger than 10μm, the modal loss in all three cases are quite low, and thus would not have dramatic influence on lasing thresholds, no matter whether it is a guiding or a half anti-guiding type of waveguide.

To further investigate the importance of the segment width, we calculated the threshold gain of the fundamental mode as a function of segment width for blue emission at 455 nm and green emission at 530 nm, as shown in Fig. 4.6c and 4.6d, respectively. The threshold gain includes the contribution of propagation loss due to the existence of neighboring narrow gap segments and the facet transmission loss at the end of the three-segment nanosheet, which is estimated using Fresnel's equations and the effective refractive index difference between the nanosheet and air, as well as the contribution of modal confinement factor, which has been defined in Eq. (4.5). As evident from the figures, the threshold increases as the width of the wide bandgap segments decreases. Therefore, it is critically important to grow the blue- and green-emitting segments wide enough to overcome the absorption loss in the neighboring narrower-bandgap segment. The plots in Fig. 4.6c and 4.6d can be divided into two domains, indicated by dashed lines. For segment widths narrower than 0.8 μm, the threshold dominated by absorption loss in the neighboring narrow-gap segment rapidly increases, indicating that such wide-gap segments

can hardly lase due to its narrow width. This justifies that ribbon-like structures with narrow width are not suited to support multi-color lasing. As the width increases from 1 to several microns, the absorption in the neighboring narrow-gap segment drops exponentially with the width. The main contribution to the threshold gain is then determined by the transmission loss at the two end facets of the nanosheet. The required threshold gains decrease to several hundred cm^{-1}, compared to >1000 cm^{-1} material gain for a typical bulk semiconductor, low enough for lasing at short wavelengths. Therefore, a judicious choice of material system is not enough to ensure lasing, and special attention must be paid to the shape, size, and arrangement of various segments in a multi-segment nanosheet structure.

4.3 Growth and Structural Characterization of Multi-segment Nanosheets

4.3.1 Growth of Multi-segment Nanosheets

The multi-segment nanosheets were grown on a SiO_2/Si substrate by CVD using a combination of VLS, VS and dual-ion exchange growth mechanisms. Temperature-dependent composition control was applied to grow the alloy semiconductors with different segments [62], [64], [93], [109]. The essence of this technique is to manipulate the position of the substrate along the axial temperature grading in the reactor to optimize the substrate temperature for the desired alloy composition. Due to the low vapor pressure of ZnS and ZnSe consequently leading to low levels of supersaturation condition, the CVD growth is typically dominated by VLS mechanism, and all attempts to grow blue-emitting nanosheet segment with sufficient width (low aspect ratio) results in narrow NW or nanoribbon (high aspect ratio), which is consistent with common understanding that the catalyst-led VLS

mechanism prevails in growth at low levels of supersaturation, producing a wire-like morphology, while the VS mechanism prevails in growth at high levels of supersaturation, producing 2D belts or sheets morphology. Thus, direct growth of desired blue-emitting nanosheet segment (requirement on composition) with wide width (requirement on morphology) is not possible. Alternatively, we decouple the realization of the desired composition and morphology by two separate procedures instead of one single step. More specifically, we first obtained the desired morphology in low aspect ratio by considering the CdSe-rich nanosheets as morphology templates with further alloy-changing potential [109], [110], [111]. Subsequent growth was performed to obtain the desired alloy composition via transferring the originally CdSe-rich into Zn-rich ZnCdSSe alloy capable of blue emission through simultaneous anion and cation exchange in the vapor phase, without significantly modifying the initial morphology. By utilizing such highly non-equilibrium exchange process, both the desired morphologies and compositions could be achieved indirectly, which may serve as a more general strategy for other materials.

The detailed growth procedure is described in the following part and is also shown in Fig. 4.7. Before growth, the SiO_2/Si substrate (serving only as a mechanical support) was cleaned and then coated with a 10 nm layer of sputtered Au. The multi-segment nanosheets are otherwise grown as freestanding structures without epitaxial connection with the substrate, since the original growth substrate can be amorphous or non-lattice-matched crystals. We use CdSe and ZnS powders (Sigma Aldrich 99.99% Metal Basis) as the source materials and a single zone CVD horizontal tube (1.5 inches wide, 4 foots long) as the reactor. The temperature profile inside the reactor was pre-measured as shown in Fig. 4.8 to determine the temperature grading and also to identify certain temperature regions

by the distance to the edge of the furnace. After placing ZnS (at the reactor center, T = 980 °C), CdSe (12 cm upstream from the reactor center, $T \approx$ 840 °C) and the substrate (16 cm downstream from the reactor center at R3, $T \approx$ 640 °C) inside the reactor, as shown in Fig. 4.7 and 4.8, the system was evacuated to 30 mtorr.

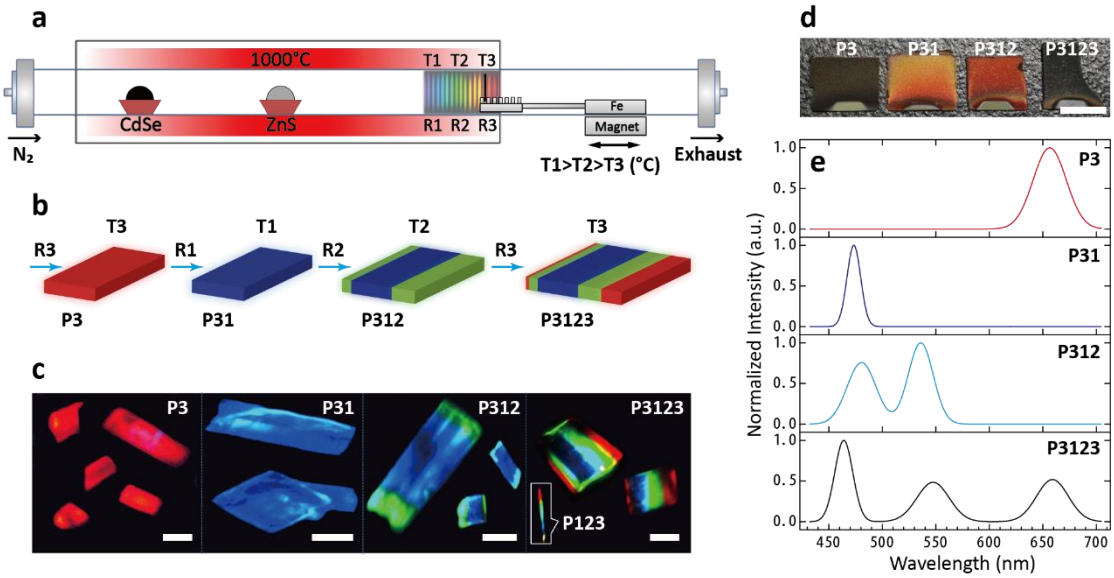

Figure 4.7 Growth procedure of multi-segment nanosheets. (a) Schematic of the CVD setup with a temperature gradient of 66 ℃ cm^{-1} in the region used for positioning the substrate (see Figure 4.8 for more detail). (b) Illustration of the growth procedure. Samples were grown starting at position R3, then at positions R1, R2 and finally back to R3, with corresponding temperatures labelled T1, T2 and T3. The associated product samples after these steps are labelled P3, P31, P312 and P3123, respectively, where the numbers following 'P' represent the growth products by sequence at various locations. For example, P312 represents a product grown first at R3, followed by growths at R1 and then at R2. (c) Photoluminescence images of individual structures after the corresponding growth sequences. Note that the images were taken after the structures were transferred onto a glass substrate from their as-grown ones using a contact printing method. Inset in the rightmost panel, a multi-segment NW structure resulting from the P123 growth sequence. Scale bars, 15 μm. (d) Optical images of the samples under ambient lighting. Scale bar, 1 cm. (e) Photoluminescence spectra of the samples shown in (c), (d).

A 10 s.c.c.m N_2 inert gas flow was introduced for 30 min to purge the reactor from O_2. The

system pressure was then set to 10 torr with backfilled N_2 and the furnace was turned on. First, CdSe-rich ZnCdSSe nanosheet structures (P3) were grown at a low temperature region R3, where the temperature (T3 ≈ 640 °C) was optimized for the growth of alloys capable of red emission and also suited for nanosheet morphology with low aspect ratio. The substrate was then moved to the higher-temperature region R1 (T1 ≈ 780 °C) using a connected iron rod driven by an external magnet to further promote diffusion processes [112]. This caused the structures to transform uniformly into a Zn-rich ZnCdSSe alloy through dual-ion exchange mechanism with no appreciable change in morphology.

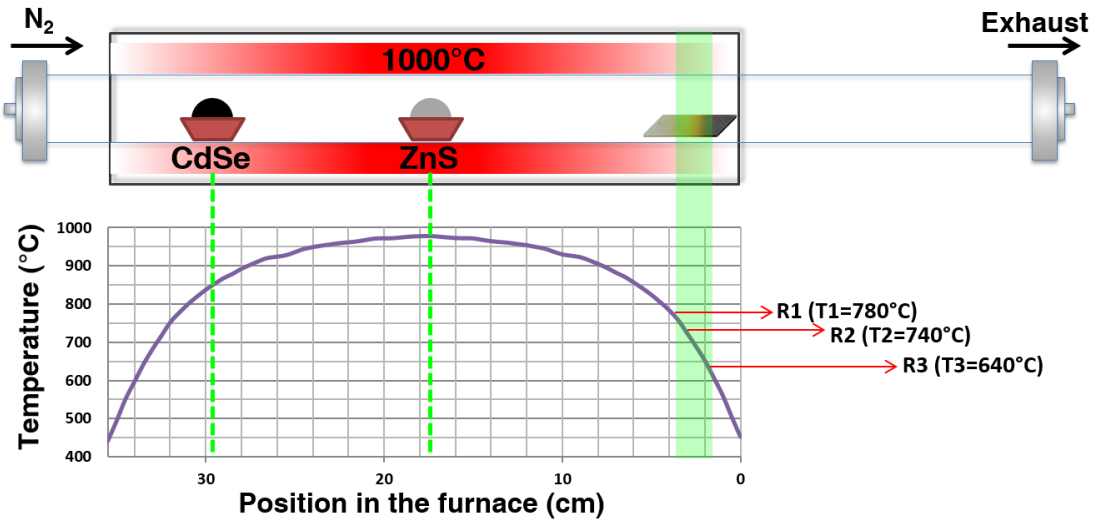

Figure 4.8 Growth setup and temperature profile within the 1-zone furnace. Schematic diagram of the setup used to grow multi-segment nanosheets, and the associated temperature profile measured by an external thermocouple along the length of the reactor tube. The measured maximum temperature of 980 ℃ (set value, 1000 ℃) is in the center of the furnace, and the temperatures at both ends of the furnace are 450 ℃. The green band on the substrate indicates the region used for growing segmented nanosheets, with a temperature gradient of ~66 ℃/cm. The positions R1, R2 and R3 indicated by arrows are optimized position for the growth of blue, green and red light emitting segments of the nanosheet, respectively.

Such processes do not change the wurtzite crystal and resulting crystal quality, as can be

seen from PL spectra in Fig. 4.7e, where the red PL peak from P3 is entirely converted to a blue peak from P31 (Fig. 4.7e) with defect-free PL features in P31.

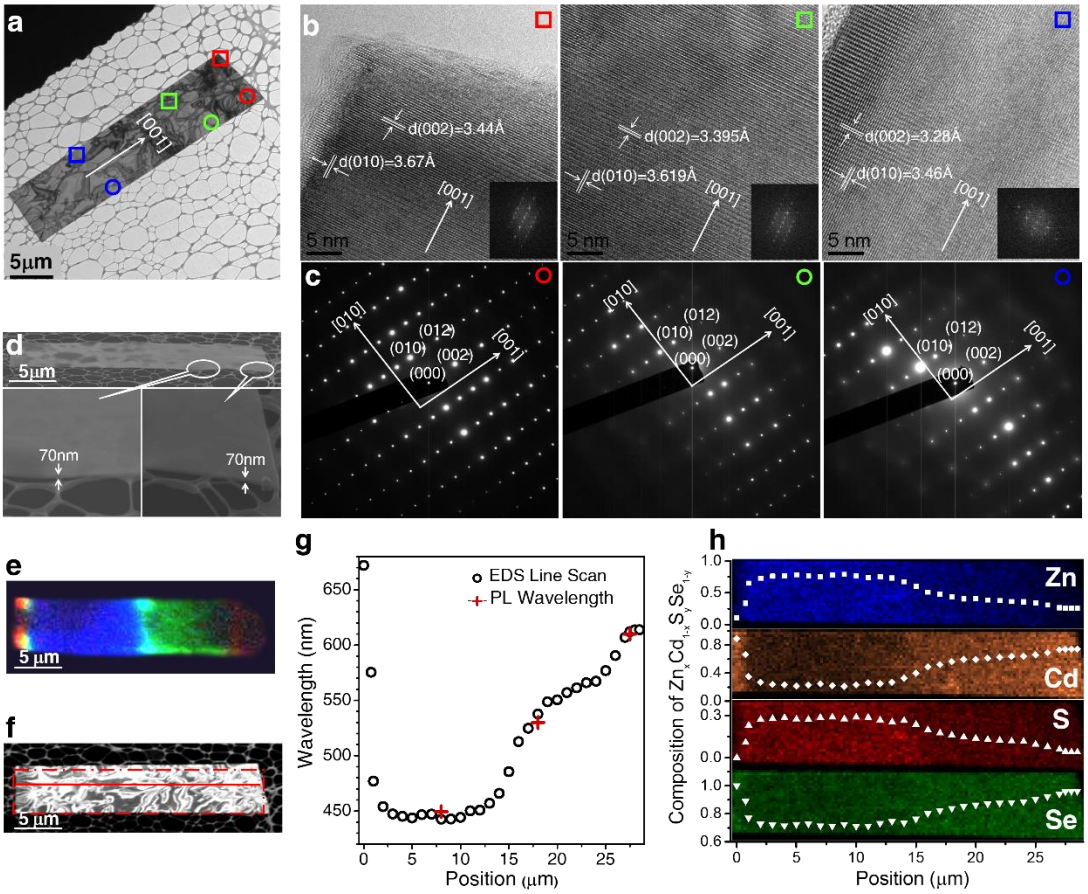

Figure 4.9 Structural characterization of a multi-segment nanosheet. (a) Low-resolution TEM image of a multi-segment nanosheet. (b) HRTEM images of the regions inside the colored squares in (a), with the corresponding color code. (c) Indexed SAD patterns of the regions inside the corresponding colored circles in (a). The HRTEM images having a 30 ° rotation compared to the SAD patterns due to image rotation at higher magnifications. (d) A 60 ° tilted SEM image of the structure with close-up views of the cross-section. The thickness was measured to be 70 nm after compensating for the tilt angle. (e) PL image of the structure. (f) TEM image of the structure. (g) Correlation of PL emission wavelengths and the extrapolated wavelengths from EDS line scan performed along the solid line in (f). (h) Correlated EDS mapping inside the dashed rectangular in (f), with atomic percentages gathered from the EDS line scan.

This indicates the high crystal quality of the transformed structures, since imperfect wide-

gap semiconductors typically show strong emission below bandgaps. Further evidence for high crystal quality after dual-ion exchange can be found in the TEM in Fig. 4.9b, 4.9c (next section). The growth process of P31 was then followed by growth at region R2 (T2 ≈ 740 °C) and the second segment was synthesized by incorporating more Cd ions to add green emission segments (P312 in Fig. 4.7b). The final growth step at region R3 added the red emitting segments, resulting in the final multi-segment nanosheets potentially capable of simultaneous RGB lasing (P3123 in Fig. 4.7b). At regions R2, and later R3, the lower substrate temperatures favor the VS mechanism for nanosheet growth, as ion transport is dominant over the ion exchange processes [113]. After completion of the growth, the furnace was turned off and allowed to cool naturally to RT while continuing the 10 s.c.c.m. N_2 flow. The growth time in each step of the experiment was shorter than 12 minutes to prevent source depletion.

4.3.2 Structural Characterization of Multi-segment Nanosheets

Structural characterization of the multi-segment nanosheet was carried out using a JEOL 2010F TEM equipped with a Link energy-dispersive X-ray spectroscopy detector at 200 kV. An FEI XL30 environmental scanning electron microscopy (SEM) at 15kV was also used for dimensional measurement. Nanosheet samples were first dispersed from as-grown structures onto a glass substrate via contact-printing [114] for dimension estimation. SEM images show that the dispersed nanosheets typically have lengths of up to 60 μm, widths of up to 45 μm and thicknesses in the range of 60-350 nm, as shown in Fig. 4.9d. A nanosheet sample was then deliberately chosen from a larger broken nanosheet piece for TEM characterization to eliminate bending issue, which could have introduced difficulties

in finding the zone axis, and moved onto a TEM grid using a homemade tapered fiber. The high-resolution TEM (HRTEM) images and selected area diffraction (SAD) pattern in Fig. 4.9b and 4.9c show that each segment of the structure is a high-quality wurtzite monocrystal, with no visible defects or strains detected. EDS analysis of the representative nanosheet in Fig. 4.9h shows that it is composed of Zn, Cd, S and Se, and the concentration of those elements changes along the red solid line in Fig. 4.9f. As one moves from the blue-emitting towards the red-emitting region, the concentrations of Cd and Se increase while those of Zn and S decrease. A good agreement has been achieved between the extrapolated wavelengths based on EDS scan and PL peak wavelengths, as shown in Fig. 4.9g.

4.4 Simultaneous RGB Lasing, Color Tunable Lasing and White Lasing from Multi-segment Nanosheet

4.4.1 Simultaneous RGB Lasing from Multi-segment Nanosheet

To demonstrate the capability of simultaneous RGB lasing, we optically pump a multi-segment nanosheet by the third harmonics of a Q-switched Nd: YAG laser (Spectra Physics, 355 nm, 10 Hz, 9 ns) with a uniform single beam at an angle of 15° from the sample normal. The source beam was directed through a convex lens and then pumped onto the nanosheet sample. We intentionally defocus the pumping beam to enlarge the beam size up to 180 μm to create a more uniform pumping area to cover the sample. The resulting emission was collected through a dark-field objective lens (Olympus LMPlanLF ×50, numerical aperture of 0.5) at an angle of 45° from the sample normal to improve the absorption of the pumping laser by the nanosheet. The tilt of the samples can also help enhance the collection efficiency of stimulated emission and reduce the spontaneous emission background.

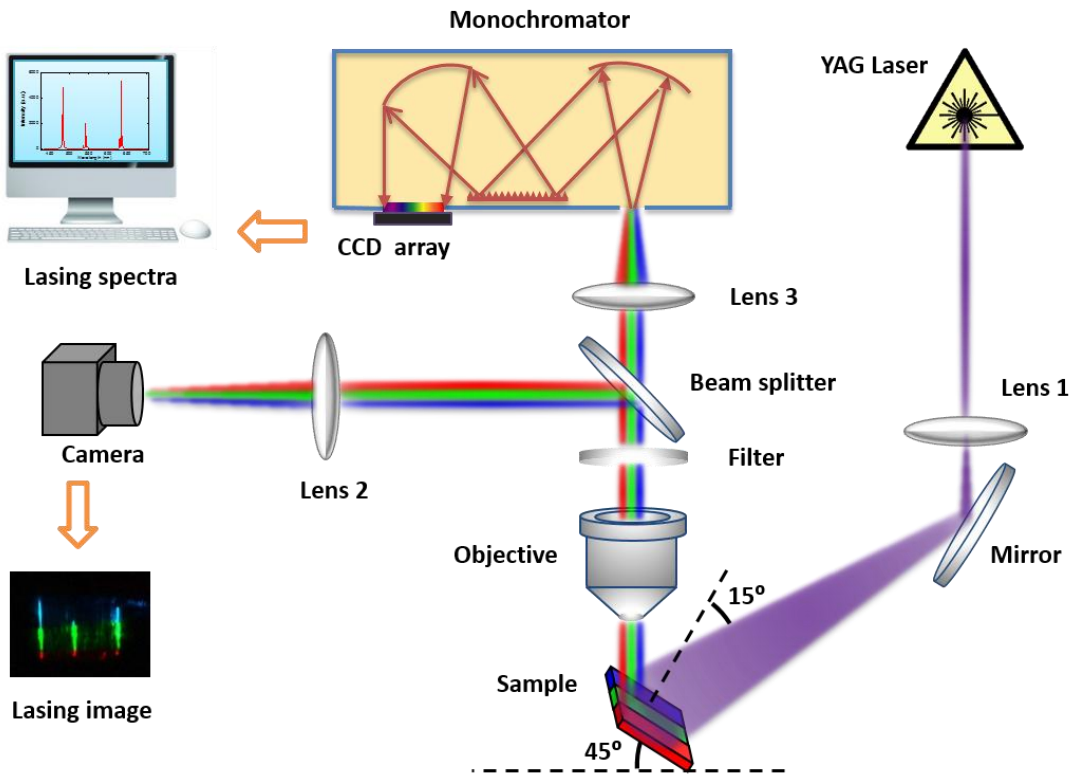

Figure 4.10 Schematic of the uniform pumping and PL collecting system.

The collected light was then passed through a 420 nm longpass filter (Semrock EdgeBasic) to remove the pump laser wavelength from the spectra. To simultaneously record both the PL image and spectra of the nanosheet, a beam splitter was used to divide the emitted light into two separate parts, one of which was collected by a CCD camera (Lumenera Infinity 2-1R) to record the real color image, while the other part was guided into a monochromator (Triax 320) equipped with a Si array detector (Jobin Yvon), cooled by liquid N_2. A 300 g/mm grating and a 2400 g/mm grating were used in the monochromator to obtain low and high resolution spectra, respectively. All optical measurements were performed at RT.

Figure 4.11 shows simultaneous multi-color lasing behavior from a representative sample under uniform pumping. The sample was intentionally cleaved from an as-grown piece by the bend-to-fracture method [81]. High-qulity end facets were thus created as

partially reflective mirrors. The main part of the multi-color lasing cavity (enclosed by the white dashed box in Fig. 4.11a) had dimensions of 28.0 μm × 18.0 μm × 0.3 μm.

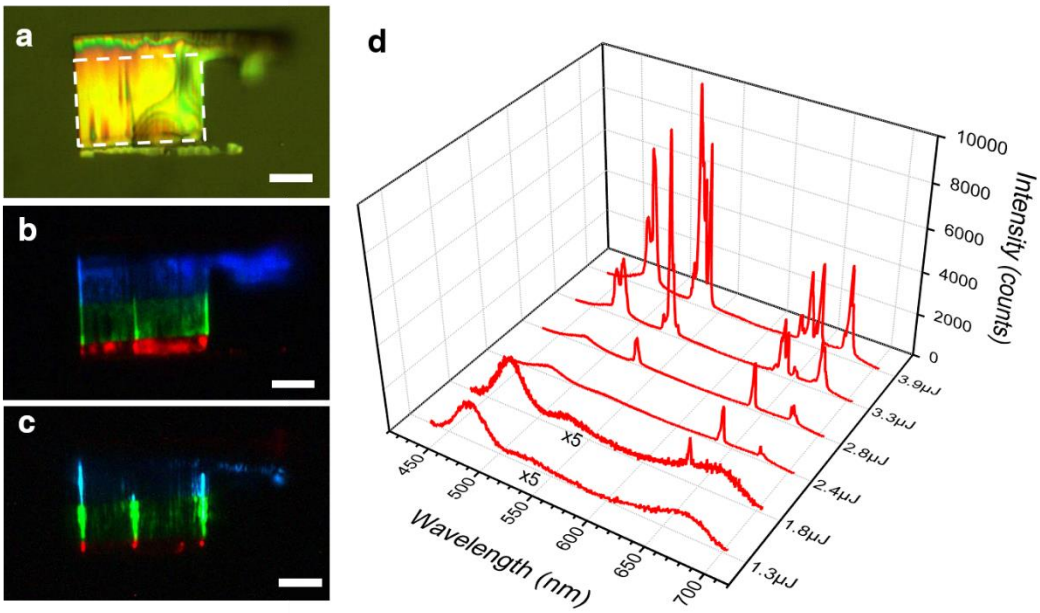

Figure 4.11 Simultaneous RGB lasing from a single multi-segment heterostructure nanosheet. (a) Bright-field optical microscope image. The dashed white box indicates the main part of the cavity. (b), (c) Real color PL images below and above the threshold with a single beam pumping (180 μm in diameter), respectively. Scale bar, 10 μm. The three strong vertical lines indicate significant scattering from the two edges and from the bent edge in the center. (d) Spectra at different pumping levels (as labeled on the lower right side of the figure). The intensities of the first two spectra have been multiplied by a factor of 5 to show the details.

This particular nanosheet also featured narrow protruding segments of irregular shape extending to the right side of the white box, indicating that the nanosheet was imperfectly detached from the as-grown piece. After the fracture, the sample was then transferred onto a MgF_2 substrate (refractive index of ~1.38) for enhanced optical confinement using a homemade tapered fiber. Figure 4.11b presents a PL image under a single pulse pumping at 1.2 μJ. Larger uniform spontaneous emissions can be seen, with scattering emissions from the edges as well. There is an additional line in the middle of the nanosheet across the

green- and light-red-emitting segments, indicating a bent edge created during the transfer of the nanosheet. Figure 4.11c shows the emissions at 4.0 μJ pulse energy. It is clear that the uniform emissions have been replaced by more pronounced scattering lines and a significantly diminished background, indicating that the transition from spontaneous emission to lasing has occurred. The spectral evolution with increasing pulse energy is shown in Fig. 4.11d. At the lowest pumping energy of 1.3 μJ, only broadband spontaneous emission is observed. Upon increasing the pumping energy from 1.8 μJ to 3.3 μJ, narrow peaks appear sequentially at red (642 nm and 675 nm), green (530 nm) and blue (484 nm) colors. Both the intensity and the number of peaks of each color increase with increasing pumping energy, which can be attributed to the well-known multimode lasing behavior [83].

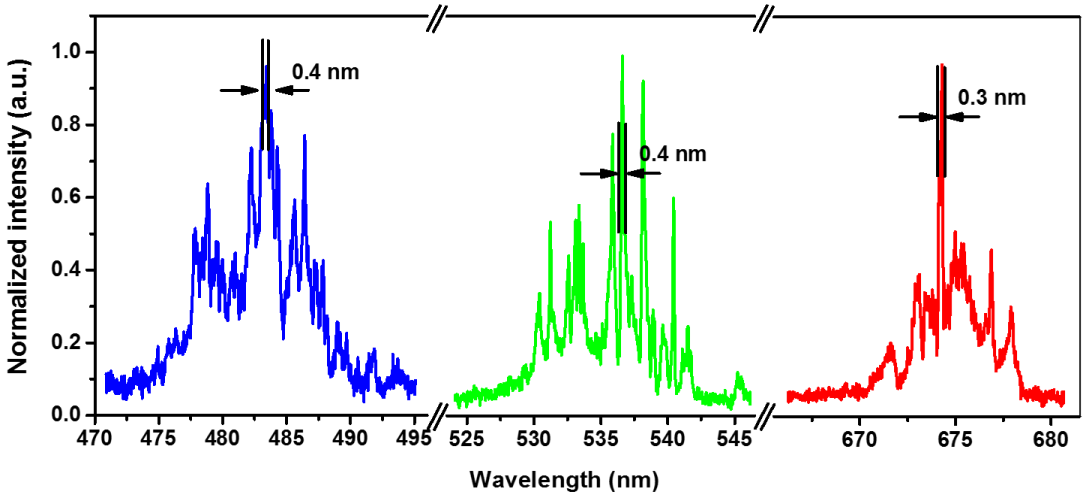

Figure 4.12 High resolution lasing spectra from the multi-segment nanosheet in Fig. 4.11

A lasing wavelength span of 191 nm, much larger than the gain bandwidth of any reported monolithic semiconductor, can be observed. The light-red lasing (642 nm) was generated from the red-emitting segment as shown in Fig. 11b and 11c. The deep-red lasing (675 nm) was generated from the edge part next to the blue-emitting segment, which is undetectable

in Fig. 4.11b, and 4.11c, because of the weak response of our camera at 675 nm (see the Infinity2-1R Camera Datasheet at http://www.lumenera.com/). Due to the large size of the nanosheet structures, different longitudinal and transverse modes cause very close mode spacing [115], so more modes are excited above the threshold with an increasing pumping intensity.

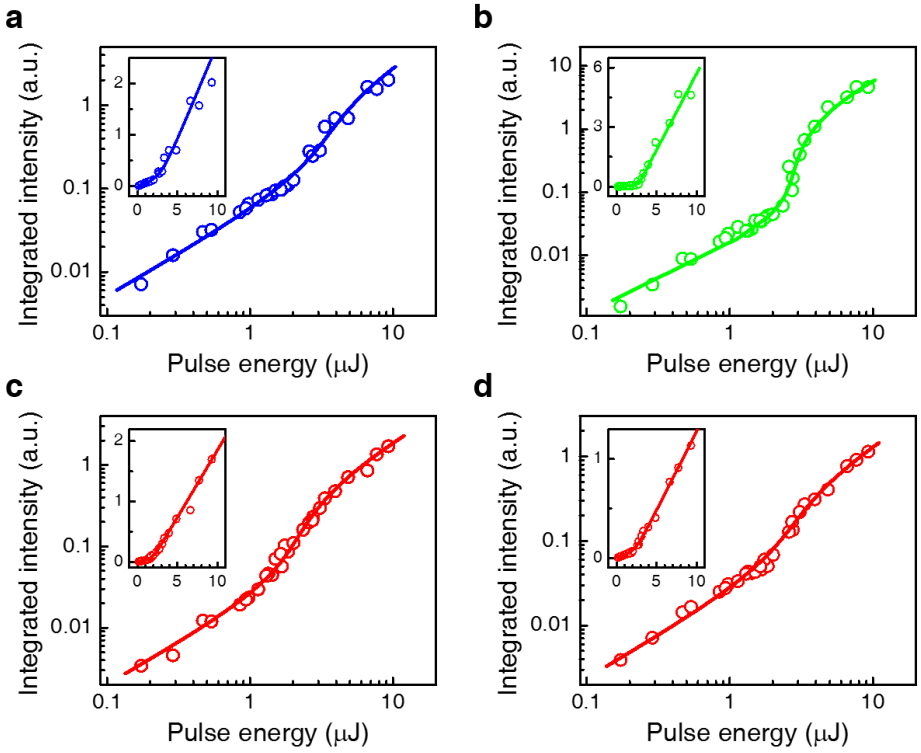

Figure 4.13 Light-in-light-out curves with multimode lasing fitting. (a)-(d) Light-in-light-out curves of the 484, 530, 642 and 675 nm lasing peaks on a log-log scale. Insets: plots on a linear scale. Circles represent direct measurements and solid lines are correlative fittings by using multimode rate equations.

At a pumping level of 3.9 μJ, multimode lasing can be clearly observed. High-resolution PL measurements were done by decreasing the entrance slit of the monochromator down to 0.1 mm and switching to the 2400 g/mm grating. The resolution limit of the spectrum system is estimated to be 0.1 nm. As shown in Fig. 4.12, distinctive multimode peaks

within the spectral band of each color, with individual linewidths of 0.2-0.4 nm, have been detected at the excitation level above the lasing threshold.

Further evidence for the multi-color lasing behavior can be seen for each of the four wavelength ranges in Fig. 4.12d, plotted into the LILO curves in Fig. 4.13a-d, reinforced by the theoretical fittings based on multimode lasing equations [87]. Typical S-like curves covering the three regimes of operation are clear in the double-log-scale plots. For all four colors, both the spontaneous emission regime, dominating at a lower pumping intensity, and the stimulated emission regime, dominating at a higher pumping intensity, have slopes of ~1. The maximum slope of the superlinear transition regime, in which amplified spontaneous emission is the dominant process, varies by color. These transition slopes are 2.1, 7.3, 2.7 and 2.2 for blue, green, light red and deep red, respectively. Because the maximum slope of the superlinear regime represents the most dramatic transition from spontaneous emission to lasing, this is often used to define the lasing threshold [116]. Based on the four individual LILO plots, the thresholds by single pulse excitation for blue, green, light red and deep red lasing are 3.3, 2.9, 2.0 and 3.0 μJ, respectively, corresponding to power densities of 1,441, 1,266, 873 and 1,310 kW/cm^{-2}, respectively.

4.4.2 Full-color Range Tuning and White Lasing from Multi-segment Nanosheet

To illustrate the potential of our multi-segment nanosheet for general illumination and display, we studied dynamic tuning of the mixed colors in the full-color range and white color lasing in particular. This required a simultaneous generation of three laser beams shaping into long, narrow, parallel stripes to pump one of the three segments each. The power of each pumping beam was adjustable individually to allow for precise, independent

tuning of the lasing intensity of each color. Therefore, a unique system was designed for three beam pumping, as shown in Fig. 4.14. The third harmonic of a Q-switched Nd: YLF laser (Spectra Physics, λ = 349 nm, repetition rate of 10 Hz, pulse width of 5 ns) was used as an excitation source, capable of providing better pulse-to-pulse stability. The lasing was first directed through a concave cylindrical lens (CL1) and a convex cylindrical lens (CL2). The length-to-width ratio of the laser beam became adjustable after the set of cylindrical lenses by changing the distance between CL1 and CL2.

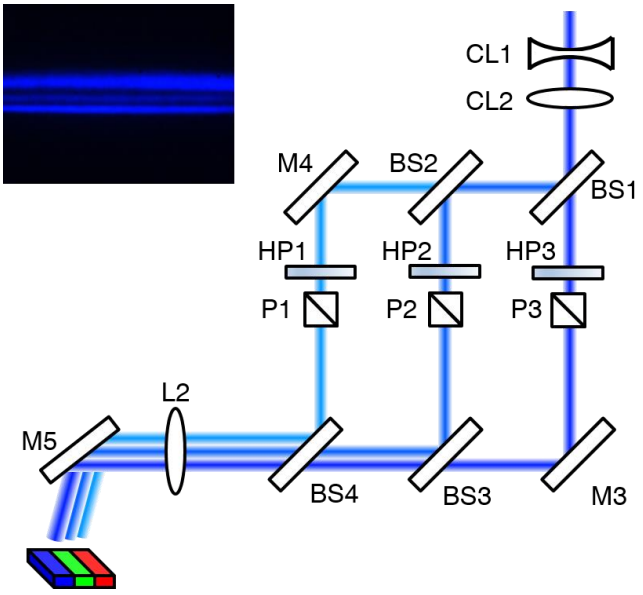

Figure 4.14 Three beam pumping system. Inset: three long, narrow, parallel stripe-like beam spots generated by the pumping system.

Two beam splitters (BS3, BS4) were then used to create three separate beams. Each beam was directed through a set comprising a half wave plate (HP1, or HP2, or HP3) and a polarizer (P1, or P2, or P3), allowing the intensity of each beam to be fine-tuned independently. Two additional beam splitters (BS3, BS4) were used to recombine the three beams and a spherical lens (L2) was used to focus three stripe-like beams parallel to the segment length direction of multi-segment nanosheet, with spot size of 260 μm × 5 μm.

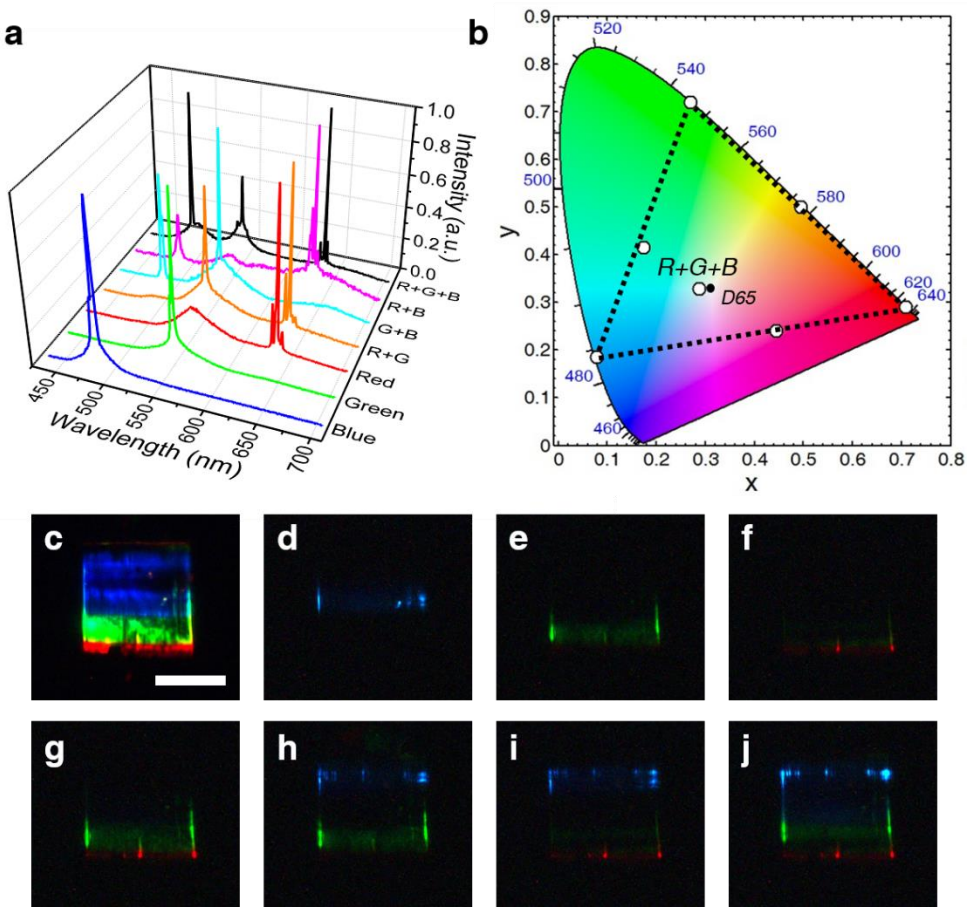

Figure 4.15 Full-color range tunable and white lasing. (a) Lasing spectra when the blue (B), green (G), red (R), red and green (R+G), green and blue (G+B), red and blue (R+B) and red, green and blue (R+G+B) segments were pumped above their respective thresholds. (b) Chromaticity of the lasing peaks extracted from the spectra in (a), shown as seven white circles. The chromaticity of the R+G+B lasing is close to the CIE standard white illuminant D65. Dashed lines indicate the range of the achievable color gamut for this particular nanosheet. (c)-(j) Real color images under low pumping (c) and above-threshold pumping (d)-(j) for the various color cases corresponding to the seven spectra in (a). Scale bar, 20 μm.

Alignment of each beam relative to the targeted segment of nanosheet was performed by adjusting the reflection angles of M3, BS3, and BS4 separately to guarantee each beam only pumped one segment. As a result, the mixed lasing color was controllably varied in the full-color range and the desired white color was achieved.

Figure 4.15 shows the PL spectra and images of full-color range tuning and white lasing from a single multi-segment nanosheet. The same collection setup in Fig. 4.10 was used for spectra and image recording, with only the collection angle of the objective being changed. An additional CCD camera (Nikon D60) was used to take ×1 magnification photographs to demonstrate the far-field color mixing, presented later in this section. The laser pump angle, objective collection angle and camera collection angle were 60°, 0°, and 75°, respectively, from the sample normal. By pumping one, two and all three of the segments above their lasing thresholds, we demonstrated independent lasing of each RGB color, simultaneous two-color lasing of any two of the three primary colors, and finally simultaneous RGB lasing (shown in Fig. 4.15d–j). Figure 4.15a presents the emission spectra for all seven cases.

To study the chromaticity of mixed color of the multi-color lasing in Fig. 4.15, the wavelengths and intensities of each lasing line must be known. The spectral features of spontaneous emission were unavoidably recorded, since the spectral collection direction in our setup is normal to the multi-segment nanosheet surface, which provided the maximum collection efficiency of the spontaneous emission but minimized collection efficiency of the stimulated emission, as shown in Fig. 4.16. The photographing collection direction, however, had the collection efficiency of the stimulated emission close to the maximum but the collection efficiency of the spontaneous emission was negligibly low. Thus, to calculate the mixed lasing color in far field, the pure lasing spectra representing the stimulated emission alone were extracted from the overall spectra by removing the contribution of spontaneous emission. Figure 4.16b illustrates how the lasing peak intensities were extracted from the measured spectra.

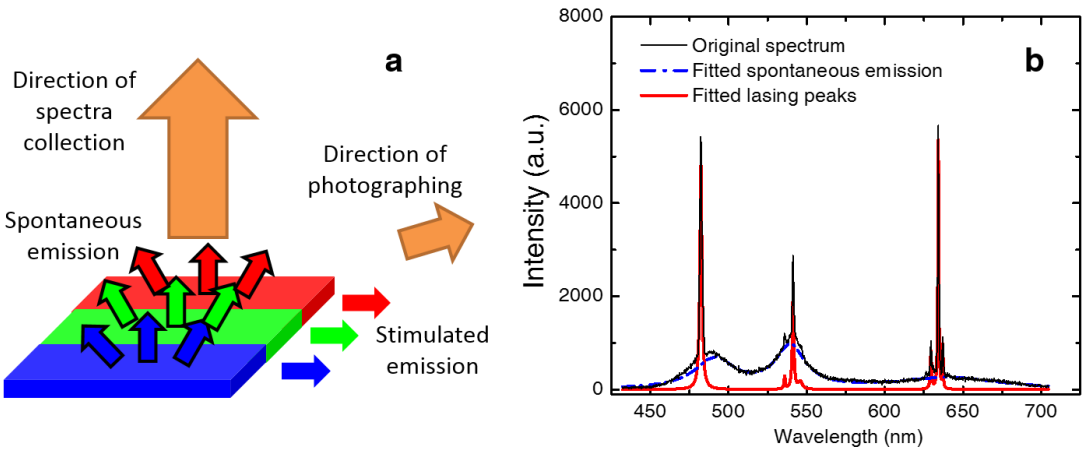

Figure 4.16 Extraction of lasing peak intensities. (a) Illustration of spectra collection direction and far-field photographing direction. (b) Lorentzian fitting of the lasing peaks and spontaneous emission spectra in Fig. 4.15a.

Multi-peak Lorentzian fitting was used to determine both the lasing peak intensity and the broadband spontaneous emission spectra. By removing the spontaneous emission background, the extracted lasing spectra can more accurately depict the color mixed solely by stimulated emission, which is the case of our far-field photography that the result is much closer to the chromaticity calculated by the extracted lasing spectra other than the raw spectra. To conclude the chromaticity point of extracted lasing spectra on the CIE 1931 color diagram, three following formulas were used to first determine the tristimulus values by the following expressions,

$$X = \int_{380}^{780} I(\lambda)\bar{x}(\lambda)d\lambda \tag{4.7}$$

$$Y = \int_{380}^{780} I(\lambda)\bar{y}(\lambda)d\lambda \tag{4.8}$$

$$Z = \int_{380}^{780} I(\lambda)\bar{z}(\lambda)d\lambda \tag{4.9}$$

where $I(\lambda)$ is the extracted lasing spectra, $\bar{x}(\lambda)$, $\bar{y}(\lambda)$, and $\bar{z}(\lambda)$ are the color matching function [117]. The chromaticity point of the mixed lasing color from the extracted lasing

spectra can be then specified with x and y coordinates on the diagram by simply using [117]:

$$x = \frac{X}{X+Y+Z} \tag{4.10}$$

$$y = \frac{Y}{X+Y+Z} \tag{4.11}$$

Figure. 4.15b shows the calculated chromaticity for these lasing spectra on the CIE1931 color diagram (red, green, blue, magenta, yellow, cyan and white). The chromaticity of the carefully balanced white lasing is very close to that of the white point, the CIE standard white illuminant D65 [117] (shown in Fig. 4.15b).

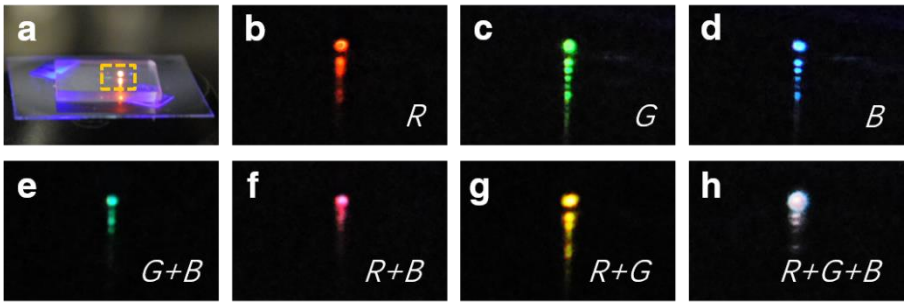

Figure 4.17 Color photographs of full-color range tuning and white lasing. (a) Photograph of the mixed emission color from a multi-segment nanosheet. (Note that the blue emission visible is from the adhesive between the MgF2 substrate and then glass slide.) (b)-(h) Photographs of the enlarged dashed-box region in (a) when the different combinations of segments are pumped as indicated by the labels inside each figure, creating the mixed far-field emission colors red, green, blue, yellow, cyan, magenta and white. The top dots in each photograph are the direct image of laser emission, while the tails under these dots are the reflection from the substrate.

To show the far-field mixing of colors from our multi-color lasers, real color photographs (Fig. 4.17) of the laser output were taken through the camera as mentioned previously, while using dynamic differential pumping (corresponding to the cases of Fig. 4.15) to control the lasing color. Figure 4.7b-d show independent red, green and blue lasing achieved by pumping each color segment individually. Yellow, cyan and magenta mixed lasing emissions were produced by pumping two of the segments, as shown in Fig. 4.17e-

4.17g. Finally, with three beams pumping all three color segments, simultaneous RGB lasing emissions were mixed together using balanced intensity ratio from a single multi-segment heterostructure nanosheet to render as a white-like color (in Fig. 4.17h). The idea is also illustrated in Fig. 4.18.

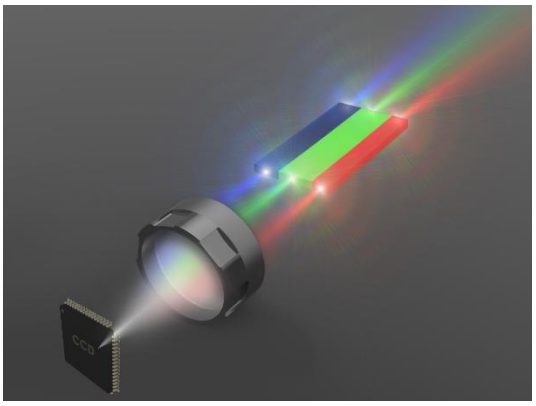

Figure 4.18 Illustration of the white laser idea. RGB lasing from the multi-segment nanosheet, collected by the camera lens was mixed at far field as white color and imaged on CCD plane.

This color mixing demonstration provides an experimental proof-of-concept for the use of our multi-color lasing structure in illumination and display applications.

4.5 Other Lasing Properties of Multi-segment Nanosheets

4.5.1 Color Gamut of Multi-segment Nanosheet Lasers

As mentioned earlier, RGB lasers enable a larger color gamut, higher contrast ratio, better color saturation, and more vivid colors than LED displays due to the narrow linewidth of the stimulated emission. The colors from single wavelength source such as lasers, which generate chromaticity coordinates at the spectra locus of the CIE map (in Fig. 4.1), can provide chromaticity in full saturation and thus cover more space in the CIE map. In contrast, colors of the broadband sources with wide spectral widths (such as those from

LEDs or thermal sources) are away from the spectra locus, which is less saturated and can only cover limited color space. Additionally, the contrast of the laser display is, of course, higher than the contrast of broadband sources. As a result, colors generated by combining three laser sources with narrow spectral lines are capable of providing more vivid colors than that generated by broadband light sources [118].

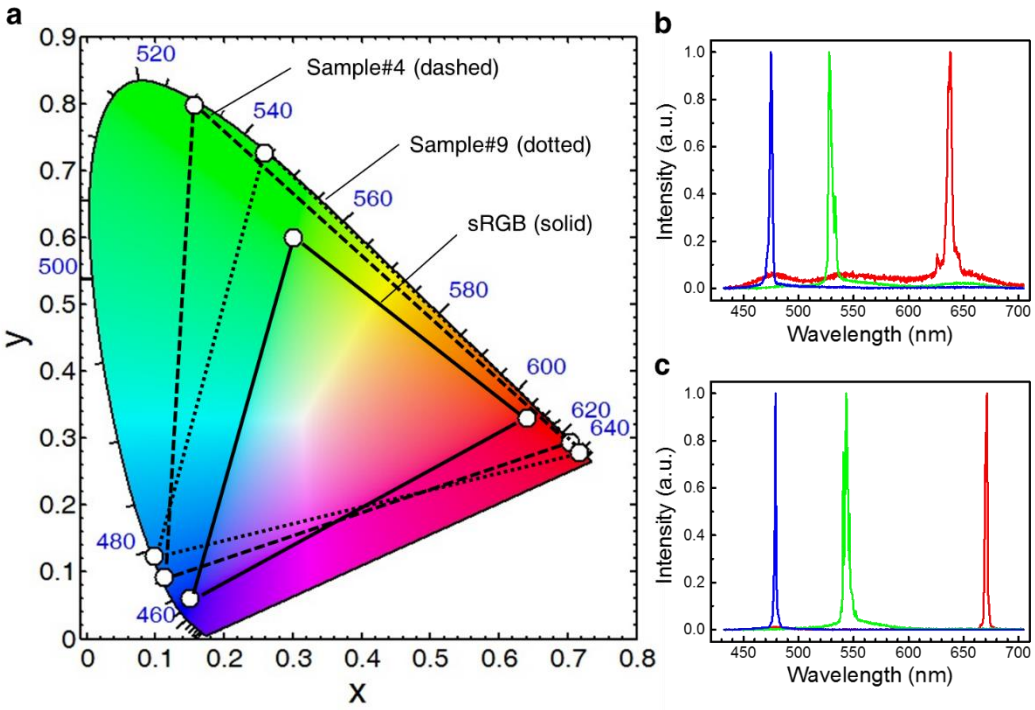

Figure 4.19 Color gamut of multi-segment nanosheets (a) Color gamut of Sample #4 (dashed) and Sample #9 (dotted) compared to the sRGB color space. (b), (c) The lasing spectra of Sample #4 and Sample #9 when the three color emitting segments of the nanosheets are excited independently.

Figure 4.19 shows the comparison of the color gamuts produced by two of our multi-segment nanosheet samples (#4 and #9), in comparison with the standard sRGB color space, which is widely used in the industry [119]. Due to the flexibility and control of alloy composition enabled by nanomaterial growth technique and the narrow linewidth of stimulated emission (shown in Fig. 4.19b and c), the three primary lasing colors of the

multi-segment nanosheet can be controlled to allow a larger color gamut to be achieved. Comparing to sRGB, the sample #4 and sample #9 cover 70% and 50%, respectively, more perceptible colors specified by the CIE LAB color space [120].

4.5.2 Estimation of the Output Power and Efficiency of Multi-segment Nanosheet Lasers

Directly accurate determination of the total emitted power from the multi-segment nanosheet by integrating contributions from all directions is challenging.

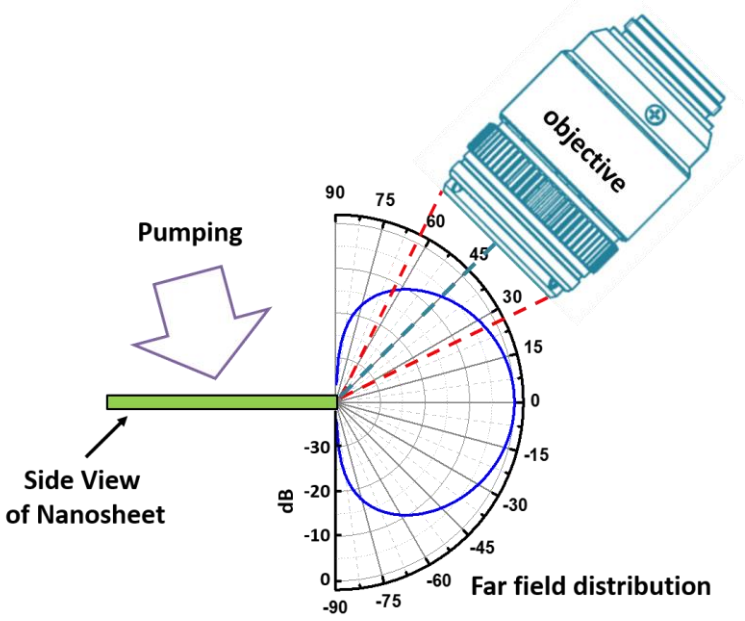

Figure 4.20 Schematic of the lasing output power estimation of a multi-segment nanosheet. The blue solid curve is a plot of the far field distribution. The thickness of the multi-segment nanosheet is assumed as 300 nm and the numerical aperture of the collection objective is 0.4.

A preferable method is to use integrating sphere. However, to perform localized optical pumping inside the integrating sphere becomes extremely difficult. Instead, we estimate the total output power by calculating the far field distribution of lasing emission as schematically shown in Fig. 4.20. The sample is mounted at 45° to the collection direction

of the objective with numerical aperture of 0.4. The collection efficiency is calculated as 6.6% according to the far field distribution (This is the same pumping and collecting configuration used in Fig. 4.10).

Table 4.4 Peak output power and the laser efficiency of multi-segment nanosheets

Sample #	Peak Output Power	Efficiency
Fig. 4.11	310 mW	1.2 %
#G-02	121 mW	0.9 %
#C-16	387 mW	4.3 %
#F-04	419 mW	1.7 %
#F-01	224 mW	3.2 %

We then estimated the peak output power from the lasing spectra shown in Fig. 4.11 and the lasing spectra of a few additional multi-segment nanosheets which were not presented previously. The peak output power and the calculated laser efficiency of different samples are listed in Table 3.4.

Absolute values of lasing output power and lasing efficiency from nano scale structure are rarely reported in literature. Geburt et al. [121] reported the peak output power of 3.5 mW in a single CdS NW with 355 nm YAG laser pumping. The reason that our multi-segment nanosheets have much larger output power than the CdS NW is mainly due to the larger volume of the nanosheet structure than the NW structure, indicating the potential of the multi-segment nanosheets in high power illumination applications. They reported 5% lasing efficiency, which is close to but slightly higher than what we achieved.

4.5.3 Lasing Threshold of Multi-segment Nanosheet Lasers

We studied the lasing thresholds of the multi-segment nanosheet sample in Fig. 4.11 and five additional samples. The results are presented in Fig. 4.21a, showing that the thresholds vary from 400 kW/cm^2 to 1400 kW/cm^2. These values are consistent with various values

of thresholds in a wide range for nanolasers made of wires, belts and sheets, as we present later. Generally, the larger threshold in blue comparing to that in green or red is likely attributed to two aspects: i) possibly lower crystal quality in the blue section, as a result of imperfect dual-ion exchange mechanism and ii) the absorption of blue wavelength light by narrower bandgap segments. Similarly, for green segments, the threshold is also dependent on its width, due to the absorption of the emission by the neighboring red segments. In addition, the differences in the absorption coefficients of pump beams by the segments with different bandgaps also increase the threshold variations.

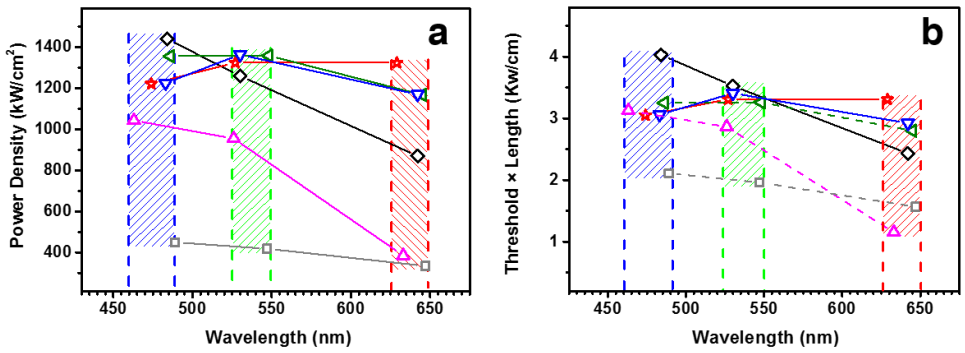

Figure 4.21 Lasing threshold of the multi-segment nanosheets (a) Threshold variations of the multi-segment nanosheets in different wavelengths. (b) Variations of threshold scaled by the length of the multi-segment nanosheets in different wavelengths

The lasing thresholds and whether a given nanostructure can lase are very sensitive to the quality of the end facets and the length of a nanosheet. In our attempt to achieve white lasers, we did not intentionally try to control the lengths of the multi-segment nanosheets during growth. In addition, further contact-printing dispersion method to select the nanosheets from the original growth substrate resulted in additional length variations.

Table 4.5 Comparison list of lasing thresholds of nanostructure material*

Refs.	Material	Morphology	Dimensions			Threshold (kW/cm^2)	Pumping Source		
			Length (μm)	Width (μm)	Thickness$ (nm)		Type	Wave-length	Pulse Width
This paper	ZnCdSSe	Nanosheet	28	18	300	400-1400	Nd:YAG	355nm	9ns
[122]	CdSe	NB	>10	-	100-800	100	Nd:YAG	355nm	6ns
[123]	ZnO	NW	12.2	-	250	270	Nd:YAG	355nm	6ns
[124]	ZnO	NW	15	-	150	150	Nd:YAG	355nm	5ns
[124]	ZnO	Nanosheet	15	-	150	50	Nd:YAG	355nm	5ns
[17]	CdS	NW	30-50	-	150	10^4	Ti:Sapphire	405nm	350fs
[121]	CdS	NW	15	-	175	10	Nd:YAG	355nm	100ns
[125]	ZnSe	Nanoribbon	>100	10	60-80	65	Nd:YAG	266nm	-
[126]	CdSSe	Nanoribbon	127	-	200	10^4(Red) 6.8×10^4(Green)	Nd:YAG	532nm	5ns
[85]	ZnO	NW	4	-	120	350	Ti:Sapphire	310nm	200fs
[8]	CdS	NW	8-43	-	>200	~ 10^4	Ti:Sapphire	405nm	100fs
[127]	CdSSe	Nanoribbon	20	5	200	80(red) 200(green)	Nd:YAG	355nm	-
[19]	ZnO	NW	2-10	-	70-150	40	Nd:YAG	266nm	3ns
[16]	GaN	NW	40	-	300	3.5×10^3	Ti:Sapphire	400nm	200fs
[128]	CdS	NW	~ 30	-	50-200	~ 10^5	Ti:Sapphire	266nm	-
[64]	ZnCdS	Nanoribbon	>100	2-5	50-80	35-190	Nd:YAG	266nm	6ns
[115]	CdSSe	Nanosheet	66	33	200	200(red) 300(green)	Nd:YAG	355nm	9ns

* All references are performed under RT except [17] at 250 K and [8] <10K;
$ Thickness or Diameter

To take into account the effects of length variations, we plot each product of the threshold power density and the length of the multi-segments nanosheets as presented in Fig. 4.21b. A decreased variation of the threshold-length product can be observed from the plot obviously. The relative standard deviations (RSD) of the lasing thresholds or threshold-length products at red, green and blue wavelengths decrease from originally 29.1%, 28.9% and 41.8% in Fig. 4.21 to 19.7%, 17.7% and 31.9% in Fig. 4.21b respectively, reflecting more consistency of the materials and structures. Other factors such as facet quality and material quality still have contribution to influence the lasing threshold variations.

For comparison, we listed the lasing thresholds of the multi-segment nanosheets and other reported values from semiconductor nanostructure lasers as shown in Table 4.5.

The reported values of the thresholds under nanosecond laser pumping varies from 10 kW/cm^2 to 60 MW/cm^2. We also listed some threshold values by femtosecond laser pumping as additional references. The thresholds of our multi-segment nanosheets are within the reported range of the values and are comparable to the similar ternary alloy material in literature.

4.5.4 Pumping Polarization Dependence of Multi-segment Nanosheet Lasers

It is known that the absorption of pump laser and thus the output efficiency of the multi-segment nanosheets are strongly influenced by the polarization of pump laser.

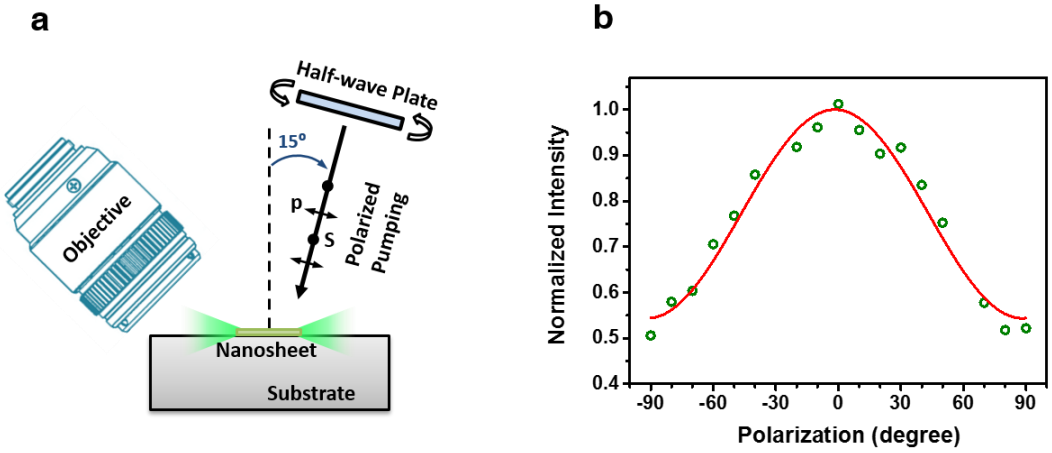

Figure 4.22 Pumping polarization-dependent experiment (a) Schematic of the experimental setup. (b) Normalized laser output from the multi-segment nanosheet as a function of half-wave plate rotation angle, with ±90 °and 0 °corresponding to the s and p polarization, respectively. Red curve is the sin^2 fitting.

To study such an influence and to maximize the efficiency of the RGB and white lasers, pumping polarization dependent experiment has been performed on a multi-segment nanosheets.

As schematically shown in Fig. 4.22a, the pump laser (Spectra Physics, Nd: YLF

laser at 349 nm) was incident on the multi-segment nanosheets at 15° from the normal, which is the same configuration as we used in Fig. 4.11 and Fig. 4.20. Due to the physical limitation of the setup, we did not attempt to use a normal incidence. But the transmission of the pump power at this incident angle is 97% of the maximum value at the normal incidence. The cavity of a multi-segment nanosheet was aligned along the incident plane, as shown in Fig. 4.22, and the green segment of the nanosheet was driven above the lasing threshold. The lasing output was collected from the end of the multi-segment nanosheet. The polarization of the pumping laser is continuously changed by a half-wave plate. The *s* and *p* polarizations are defined as usual as being in perpendicular and parallel to the incident plane, respectively. Fig. 4.22b shows the normalized lasing intensity from the multi-segment nanosheet laser as a function of the polarization angle. ±90° and 0° correspond to the *s* and *p* polarization, respectively. The polarization-dependent lasing intensity follows a $\sin^2$ functional dependence with the maximum at p polarization and minimum at s polarization. Due to the small incident angle (15°), the reflection difference in *s* and *p* polarizations of the pump laser at the air-nanosheet interface can be neglected. The main reason of the polarization-dependent pumping efficiency is the absorption anisotropy in NWs and nanosheets with aspect ratio larger than 1. The absorption coefficient of a nanostructure-waveguide is higher when the pumping polarization is parallel to the waveguide (along the length direction, or *p* polarization in this case) [129]. In all of the lasing demonstration above, the pumping laser was controlled at *p* polarization. Thus, the polarization of pump lasers in all the measurements has been optimized.

4.5.5 Power Stability of Multi-segment Nanosheet Lasers

In order to study the lasing stability of the multi-segment nanosheets, we continuously pumped a nanosheet structure with a UV laser (Spectra Physics, Nd: YLF laser at 349 nm). The output lasing intensity as a function of operation time is shown in Fig. 4.23, where we can see that the variation of the output lasing intensity is fluctuating at 5% for all the lasing colors, consistent with the noise level of the pump laser applied in the measurement. The systematic decrease of the lasing intensity at all three colors is less than 5%, indicating a negligible degradation of the lasing intensity in 20 minutes of operation.

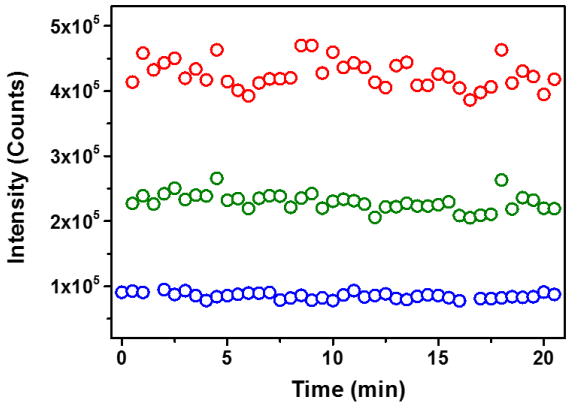

Figure 4.23 Lasing intensities of red, green and blue colors from a multi-segment nanosheet as a function of operation time.

Such power stability is even close to some of the commercial optical pumped solid state lasers, revealing a huge practical potential of the multi-segment nanosheets.

4.6 Summary

In this chapter, I have demonstrated simultaneous RGB lasing from single monolithic ZnCdSSe nanosheets at RT. White and tunable lasing over the full range of visible colors has been achieved through controlled pumping of different segments in a multi-segment

nanosheet of ZnCdSSe quaternary alloys. The demonstration lies in a combination of the comprehensive cavity analysis, the detailed characterizations and the thorough understanding of the growth mechanism. The exploitation of the interplay among the VLS, VS and dual-ion exchange enables the growth of nanosheets composed of several parallel segments with the desired alloy compositions, geometry and crystal quality. The designed parallel cavity arrangement significantly reduces the absorption of shorter-wavelength photons by the narrower-bandgap material, compared to composition-graded one-dimensional nanostructures [74]. As a result, lasing over a wavelength range of 191 nm in a single monolithic structure, the largest ever reported, has been observed, facilitating the realization of the monolithic white laser ultimately. Finally, it is important to note that the term ‘white laser’, which associates concepts linked to broadband and monochromatic emission, might at first appear self-contradictory. The above results demonstrate that the apparently contradictory terms ‘white’ and ‘lasing’ can both be realized in a single monolithic structure, which greatly simplifies the process of creating monolithic laser structures with dynamically color-controllable emissions, and make an important first step towards the realization of an electrically driven white-color and full-color nanolaser from a single monolithic structure.

CHAPTER 5

MID-INFRARED LASING IN A *PbS* SUBWAVELENGTH WIRE

5.1 Introduction

MIR lasers in the wavelength range of 2-5 μm have a wide range of applications, such as molecular spectroscopy [130], materials processing [131], chemical sensing [132], medical diagnosis [133], and so on. Due to the much weaker radiative processes in narrow gap materials, lasing from one-dimensional semiconductor structures such as SWWs or NWs has been mainly limited to UV and visible wavelengths, with few reports in near infrared wavelengths from 870, 980 nm [134]. The longest wavelength reported so far is around 1.6 μm in GaSb wires [135]. Yet, MIR range lasing in SWWs has never been demonstrated. On the other hand, semiconductor SWWs or NWs are expected to be good candidates in integrated photonic fields, since they can naturally function as gain materials, optical waveguides or laser cavities, simultaneously. Therefore, developing SWWs laser in 2-5 μm range would have a great impact on the optical integration for sensing and detection applications in MIR.

PbS, as an important narrow bandgap material, has the great potential for very efficient MIR emission. It has direct bandgap with bandgap energy less than 0.5 eV. Due to the nearly symmetric conduction and valence bands [136], PbS has similar effective masses of electrons and holes near the band edge, which increase the efficiency of electron-hole recombination by reducing the probability of Auger recombination, as one of the critical non-radiative mechanisms compete with radiative recombination in narrow gap semiconductors. Thus, very high luminescence efficiency can be achieved in PbS

compared to other narrow bandgap semiconductor materials in III-V group. Another distinctive feature of PbS material (or any lead salts material) is its expansion of bandgap with temperature. Due to the positive lattice expansion [137], [138], the spectra of spontaneous emission or gain profile of the PbS material has blue shift rather than red shift with temperature increasing, in contrast to most of the common semiconductors.

In this chapter, I will present MIR lasing from single PbS SWWs at wavelength more than 3 μm. The PbS SWWs were grown by CVD. The morphology of both as grown and individual SWWs is observed through SEM. Single PbS SWW was removed from as grown substrate for optical characterization. Lasing is demonstrated by identifying the transition from spontaneous emission to stimulated emission with clear threshold behavior. The temperature-dependent experiment has been performed showing a continuous blue switching of the lasing emission from one resonance mode to another while temperature increases. Single-mode lasing at temperatures up to 180 K has also been achieved. The volume of the wires can be smaller compared to the wavelength cubic, which represents a new way to realize MIR lasing from subwavelength structure.

5.2 Growth and Structural Characterization of PbS Subwavelength Wires

The PbS SWWs were grown by CVD approach in a three zone furnace using PbS powder as source material. Si substrates without deposited catalysts were placed on a quartz plate at a low temperature zone of 400 °C. The system was evacuated to a pressure lower than 100 mTorr. During growth, 50 sccm argon, including 5% hydrogen, was introduced into the growth chamber which raised the pressure to ~15 Torr. After the furnace reached the target temperature, the PbS source boat was inserted into the center of the furnace at a high

temperature zone of 600 °C via a magnetic loading rod. The PbS source powder was sublimated in the high temperature zone and deposited onto the substrates in the low temperature zone about 10 cm downstream. A detailed description of the growth of PbS wires was in Ref. [139].

To study the crystal structure of the PbS SWWs, HRTEM and SAD pattern measurements were conducted by a JOEL 2010 field emission TEM operating at 200 kV.

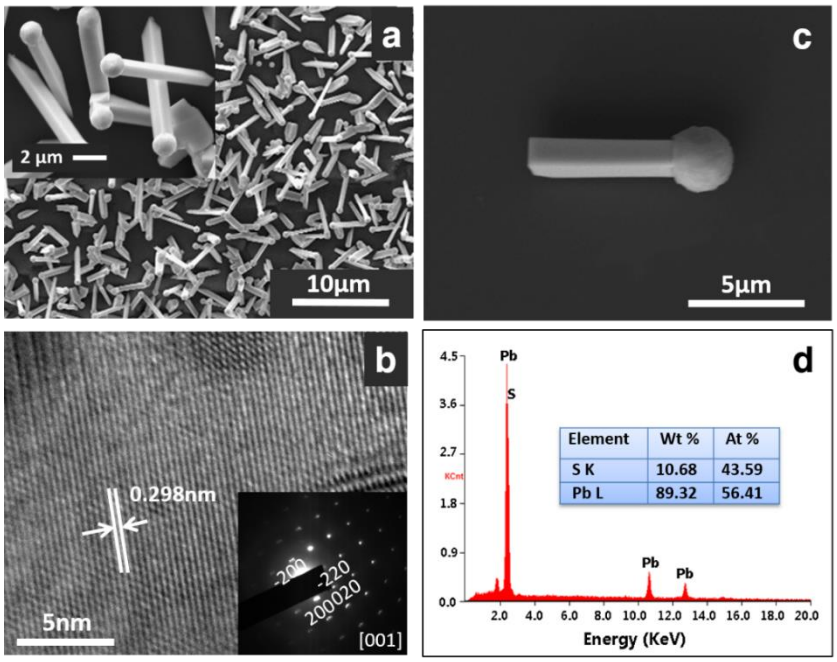

Figure 5.1 Structural characterization of PbS wires. (a) SEM images of as-grown PbS wires. Inset: zoomed-in SEM images of typical as-grown PbS wires. (b) HRTEM of a PbS wire. Inset: SAD pattern of TEM. (c) SEM image of a single PbS wire with dimension of 6.3 μm by 1.3 μm by 1.3 nm. (d) EDS results of PbS wires.

The SEM and the EDS analysis were also carried out in environmental ESEM (FEI XL30) for morphology and elemental composition analysis. Figure 5.1a shows the morphology of as-grown PbS wires. The wires are randomly oriented. The cross section of the PbS wire is approximately 1.5 μm square shaped and the length is around 5-10 μm. Each wire is

attached to a lead sphere at one end, as a result of the VLS mechanism. The diameters of the lead sphere tips are around 1.5-2.5 μm. The HRTEM image in Fig. 5.1b shows a lattice spacing around 0.298 nm, which matches with the [200] lattice spacing of PbS. The SAD pattern of a typical wire (Fig. 5.1b inset) has a [001] zone axis and a rock-salt structure. The EDS analysis in Fig. 5.1d features the peaks corresponding to elements lead and sulfur with an atom ratio of 56:43. More measured lead than sulfur is attributed to the lead rich ball-shaped tip of the wire, clearly shown in the zoomed-in SEM image (Fig. 5.1a inset).

To examine individual wires in detail, single PbS SWWs were removed from the as-grown Si substrate and transferred onto a sapphire wafer for optical and SEM measurement. Figure 5.1b shows the SEM image of a single PbS SWW as an example. The dimensions of the single PbS wire are 6.3 μm × 1.3 μm × 1.3 nm. One can clearly see the regular cuboid structure of the SWW, which is very important to achieve high Q factor of the cavity and reduce the lasing threshold.

5.3 Mid-Infrared Lasing in a Single PbS Subwavelength Wire

To demonstrate the capability of PbS wire lasing, we optically pumped a PbS SWW. The setup is similar to what has been shown in Chapter 2, but here we use a passively mode-locked Ti: sapphire laser (790 nm, 80 MHz, 150 fs) as excitation and all the other optical elements in the experiment are designed for MIR range. The laser beam was pre-chopped and focused into a 5 μm spot size. The PL emission was collected by a spectrometer equipped with an InSb photodiode detector. The sample was loaded into a cryostat for low temperature measurements. Figure 5.2 shows the PL spectra of a typical PbS SWW under different excitation powers at 77K. The size of the wire is 7.4 μm × 1.3 μm × 1.2 μm. At

low pump power only broad spontaneous emission is observed. As the pumping power increases to 38 mW, a narrow peak appears at 2.97 μm, indicating the occurrence of population inversion and the start of the amplified spontaneous emission.

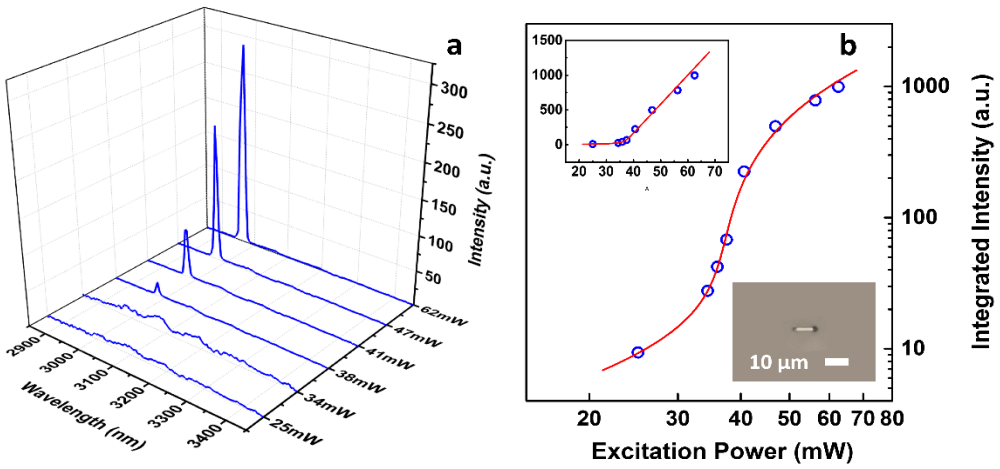

Figure 5.2 Single mode lasing from a PbS SWW. (a) PL spectra of a SWW under different excitation power at 77K. (b) LILO curves with fitting on log-log scale at 77 K. Top inset: LILO curves on linear scale; Bottom inset: optical image of the measured PbS wire.

Eventually at high pumping power above 60 mW, the linewidth of narrow peak decreases further down to 7 nm with the intensity several orders of magnitude higher than the spontaneous background. The volume of the wire is as small as 0.44 λ^3. Due to the subwavelength volume of the PbS wire, only single mode lasing is observed in Fig. 5.2a. More significant evidence of lasing is provided in the LILO curve in Fig. 5.2b, showing a clear kink behavior on linear scale (Fig. 5.2b top inset) and a typical S-shape curve on double-log scale. Three different regimes of PL emission, from spontaneous emission (with a slope of ~1), through threshold transition (with a slop of ~19), and finally to stimulated emission or lasing (with a slope back to ~1) have been identified in Fig. 5.2b. It is worth noting that the scaling power index of superlinear regime reaches the maximum of 14.9, indicating a very dramatic lasing threshold behavior. The lasing threshold is defined to be

36.9 mW, extracted from the LILO curve on log-log scale at the maximum slope in transition regime.

Temperature-dependent PL measurement was also performed on PbS SWWs. We firstly examined the PL emission from as-grown PbS SWWs under constant low level pumping, in order to explore how spontaneous emission varies with different temperatures. Figure 5.3 displays the related results. The PL peaks obviously show continuous blue shift with the increase of the temperature from 77 K to 180 K, which consistent with the instinct feature of bandgap expansion in lead salts material discussed in the introduction part.

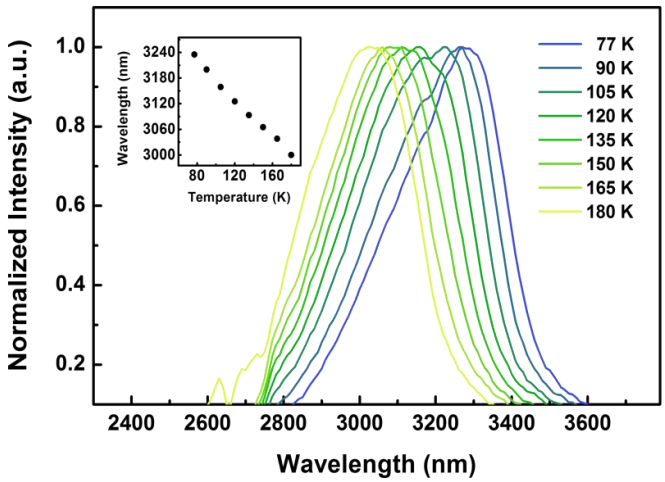

Figure 5.3 Temperature-dependent PL spectra (normalized) of as-grown PbS SWWs. Inset: PL peaks versus temperature.

We then examine the lasing behavior of a single PbS wire at different temperature under constant high level of pumping above the threshold. The dimensions of the wire are 6.7 μm × 1.8 μm × 1.4 μm. The lasing peak wavelength varies from 3.26 μm to 2.99 μm as temperature increases, shown in Fig. 5.4a, while the highest lasing temperature is achieved at 180 K. It is interesting to see the switching of lasing modes to shorter wavelengths with the increasing temperature, which is due to the blue shift of the gain profile leading to

successive turn-on of the shorter wavelength modes.

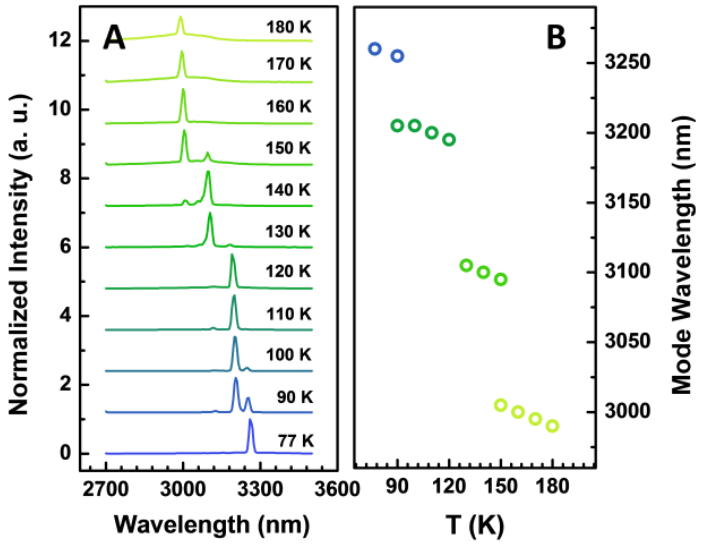

Figure 5.4 Temperature dependent lasing from a single PbS SWW (a) Temperature-dependent lasing spectra of the PbS SWW. (b) Lasing mode wavelengths versus temperature

Figure 5.4b shows how the wavelengths of various modes change with temperatures.

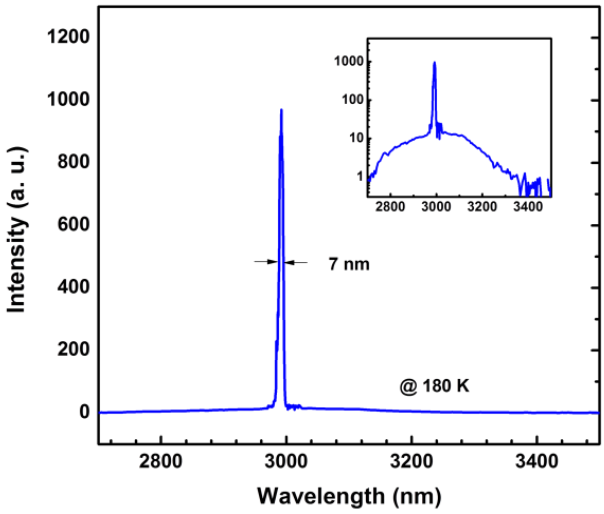

Figure 5.5 High resolution lasing spectrum at 180 K in linear scale and semi-log scale (inset).

It is clear that not only do modes switch from one to another, but also the mode positions have blue shift as a result of a negative thermo-optic coefficient. In addition, due to the

subwavelength sizes, the mode separation can be as large as 90 nm. As a result, single mode lasing is easily achieved in such SWWs.

Figure 5.5 shows the spectrum at 180 K under high resolution measurement. The FWHM of the lasing peak is 7 nm with a central wavelength of 3 μm, corresponding to a Q factor of 430, which is more than 3 times larger than the estimated cavity Q based on the amplified spontaneous emission below the laser threshold.

5.4 Summary

In this chapter, high quality PbS SWWs were grown on Si substrate using the CVD method, which shows strong band edge emission even at RT. Single mode MIR lasing from individual PbS SWWs at wavelength range around 3 μm was observed. The volume size of the PbS SWW is less than the wavelength cubed of $0.44\lambda^3$. Clear lasing threshold behavior has been demonstrated with a scaling power index as large as 19. The temperature-dependent experiment has been performed under both low pumping levels on as-grown PbS SWWs and under high pumping levels on single PbS SWWs. It shows a continuous blue shift of spontaneous emission peaks and a blue switching of different modes in the range of 2.9 μm to 3.3 μm with the temperature increasing from 77K to 180K. Single mode lasing at temperatures up to 180K with narrow linewidth has also been achieved, with corresponding Q factor of 430. Such SWWs lasers, grown on Si substrate with good crystal quality and large cavity Q factor, will have a wide range of applications. We believe the results pave the fundamental step towards electrical driven RT subwavelength PbS lasers and allow for high-density integration of photonic integrated circuits.

CHAPTER 6

MEMBRANE TRANSFERRED SEMICONDUCTOR NANO-RING LASERS

6.1 Introduction

As introduced in Chapter 1, Si-based nanolasers have long been pursued [140] due to their potential applications for on-chip interconnects in the future of large-scale photonic integrated circuits, among many other applications. Yet, the development of Si-based light source is greatly hindered by the fundamental fact that Si is an indirect bandgap material. Optical transition in Si is far less efficient, since both energy conservation and momentum conservation need to be held. That is why, up to date, most semiconductors lasers, especially nanolasers, are attained by compound semiconductors. Methods of heterogeneous integration to combine compound semiconductors with Si substrates are highly demanded. Various attempts have been made to achieve heterogeneous integration on a Si platform. Among them, membrane transfer approach is considered to be the one of the promising techniques and has attracted great deals of interest ever since the first demonstration in 2006 [32]. The use of the transfer method is based on that the adhesion energy between a semiconductor membrane and an elastomeric stamp has a peel-speed dependency. High peel-speed is employed for lifting the membrane from the donor substrate to stamp, while low peel-speed is employed for releasing the membrane from stamp onto the receiving substrate. For laser applications, the membrane transfer approach not only provide an alternative avenue for eventual Si-based integrated photonic systems, but also allows the membrane to be transferred on a metallic surface for more efficient heat dissipation. Thus, empowered by membrane transfer approach, laser devices with various

kinds have been successfully demonstrated [3], [4], [33], [141]. Although significant progress has been made, challenges remain with the release process of the membrane to different substrates. The success of the membrane transfer approach often depends on the surface properties of the receiving substrates and is sensitive to the peel-speed of the stamp, making it difficult to release and transfer membranes in a controllable and reproducible manner, for different receiving substrates with high yield. In addition, most of the lasers demonstrated so far are large devices with lateral sizes over tens of microns.

In this chapter, an alternative membrane transfer approach is applied by using an intermediate layer between the membrane and the polydimethylsiloxane (PDMS) stamps. Successful demonstration of semiconductor membrane layers transferred onto MgF_2 substrates with high controllability and high yield has been attained. Subsequent fabrication of devices based on the transferred membranes verify the overall success of this approach. Nano-ring lasers as small as 1.5 μm in diameter with radial width of 400-500 nm and thickness of 260 nm have been fabricated. Single mode lasing is achieved on individual nano-ring lasers at RT under optical pumping, with emission wavelength of ~980 nm.

6.2 Membrane Characterization and Nano-ring Laser Fabrication

The design of the wafer used for membrane transfer is shown in Fig. The wafer includes a 250 nm semiconductor membrane layer and a 10 nm AlAs sacrificial layer for lateral etching, epitaxially grown on top of a GaAs substrate. The membrane has a p-i-n structure, including an intrinsic core layer as an active region sandwiched by a n- and p-doped InGaP contact layers, each including a protective cap layer. The core layer consists of five quantum wells of $In_{0.15}Ga_{0.85}As$ and $GaAs_{0.88}P_{0.12}$ layers as barriers. It is crucial for a careful

wafer design to compensate for strain through the fine tuning of thickness and composition between the quantum well and barrier layers, and the overall symmetric structure are accomplished.

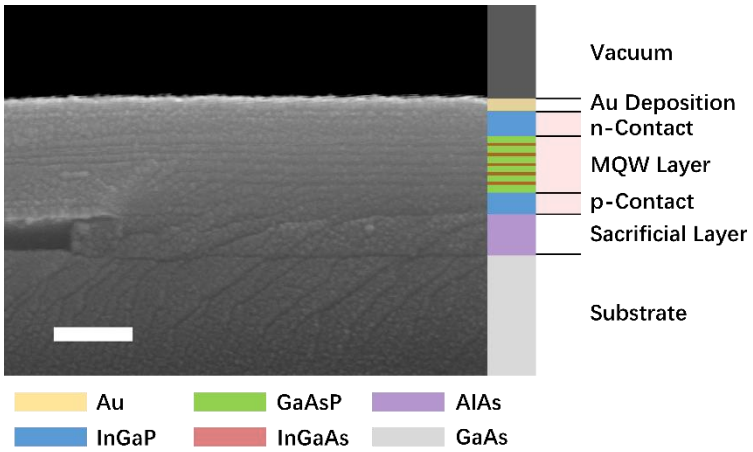

Figure 6.1 Cross-section SEM image of the membrane layer and wafer in use with structural illustration. The total thickness of the membrane for transfer is indicated by the light red column between Au deposition and sacrificial layer. Scale bar 200 nm.

The strain compensation is critical for transfer step in preventing the membranes from curling after the sacrificial etching. The wafer structure is characterized by cross-section SEM. A Au deposition layer was applied on top of the wafer vertical to the cross-section plane to increase the conductivity of the sample for better image quality. The actual thickness of the membrane structure was measured to be 260 nm, as shown in Fig. 6.1.

The membrane release and transfer process, including device fabrication, is schematically shown in Fig. 6.2. After cleaning, the wafer was patterned into 250 μm × 250 μm squares by AZ3312 photoresist (PR) (Fig. 6.2b). A two-minute ICP etching step with 2.5 sccm Cl_2 and 35 sccm BCl_3 at 4 mTorr in a STS all general etch tool was followed to create 40 μm-wide trenches on the wafer (Fig. 6.2c). The sample was then immersed in a 2% HF solution for 16 minutes to selectively under-etch the AlAs layer and the residual

PR served to anchor the membrane mesas to the GaAs substrate preventing them from free floating (Fig. 6.2d).

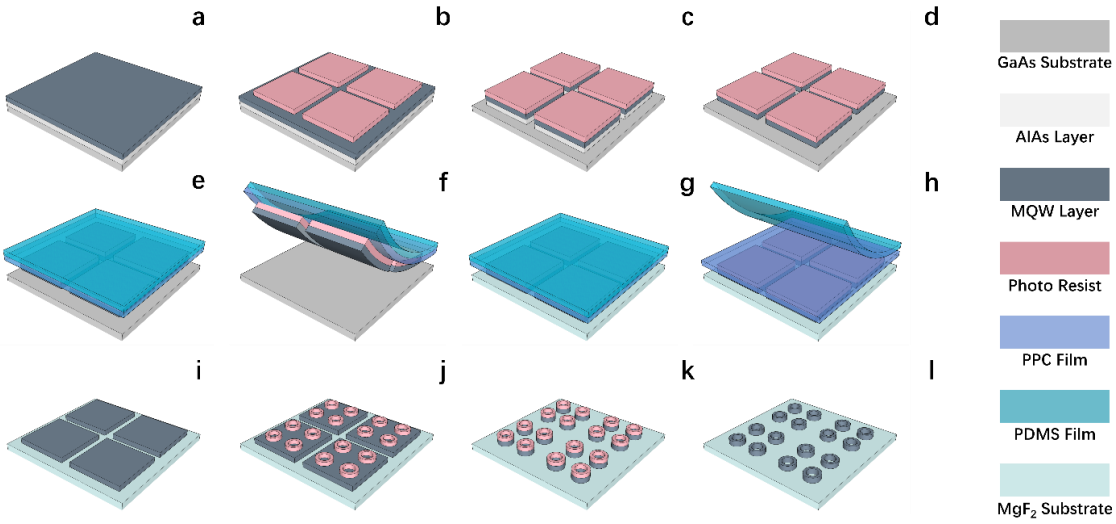

Figure 6.2 Membrane transfer and device fabrication process: (a) starting wafer as shown in Fig. 6.1. (b) patterning with PR AZ3312 to define 250 μm × 250 μm squares over the entire wafer. (c) ICP etching down through the AlAs sacrificial layer to produce trenches for under-etching. (d) 2% HF wet under-etching of AlAs sacrificial layer. (e-f) membrane pick-up by a PDMS-PPC bilayer film. (g) membrane transferred onto a new receiving substrate (MgF_2 in this work). (h) PDMS removal. (i) PPC and PR dissolution by acetone. (j) laser structure patterning. (k) ICP etching. (j) PR cleaning to shape the final laser device.

Picking-up the membrane from the grown substrate was typically carried out by directly using a PDMS stamp as reported by many previous works [3], [4], [32], [33], [141]. However, releasing the membrane from the PDMS stamp to the new receiving substrate turns out to be often problematic as a result of strong adhesion between the PDMS and the semiconductor membrane. The previous standard methods rely on the control of the speed at which the PDMS is peel-removed from the receiving substrate. Due to the different surface adhesion condition between the semiconductor membrane and the receiving substrate, extensive calibration of peel-speed through numerous experiments is required.

To have a more generally applicable and systematic releasing procedure that works for different types of semiconductor membranes and receiving substrates, we adopted an approach that has been demonstrated recently in a graphene layer transfer [34] using a polypropylene carbonate (PPC) film as an intermediate layer between the PDMS and the semiconductor membrane. The PPC was first spin coated on a PDMS film. Membranes were next picked up by the PPC-PDMS bilayer from the original growth substrate with the PPC layer facing down in direct contact with the semiconductor membrane (Fig. 6.2e and 6.2f). After releasing the membrane from the grown substrate, the PPC-PDMS bilayer was heated up to 110 ℃ together with the membrane to soften the PPC layer. The bilayer was then attached onto the receiving substrate with the membrane side in contact with the substrate surface. After cooling down the temperature below its glass transition point, the PPC became hardened and much easier to be detached from the soft PDMS layer. Therefore, by removing the PDMS layer, the PPC thin layer was left on the top of the membrane and the substrate (Fig. 6.2h). Since the releasing process only deals with the adhesion between PPC and PDMS, this procedure is applicable in general for different types of substrates and membranes. In this work, a MgF_2 was used as a receiving substrate for its low refractive index but higher thermal conductivity than SiO_2. After the removal of the PDMS layer, both the PPC and PR residues were dissolved by acetone and completely cleaned away by O_2 plasmon (Fig. 6.2i). Ring shapes were then patterned onto the transferred membrane (Fig. 6.2j) via photolithography and an identical dry etching step was applied to finalize the laser patterns (Fig. 6.2k), followed with an eventual clean step (Fig. 6.2l).

The fabrication results are shown in Fig. 6.3. The SEM image of a released 250 μm × 250 μm membrane square after the transfer step (Fig. 6.3a) provides the evidence of successfully using this membrane transfer method.

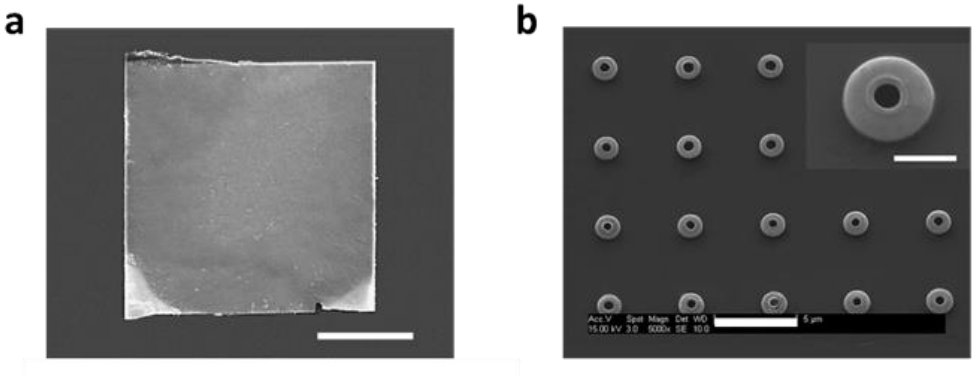

Figure 6.3 SEM image of a released membrane and the final nano-ring laser arrays (a) SEM image of a released membrane of a square shape with side length of 250 μm before nano-ring patterning, scale bar 100 μm. (b) SEM image of fabricated nano-ring laser array, scale bar 5 μm. Inset: zoomed-in image of a nano ring laser with an outer diameter of 1.47μm, inner diameter of 240 nm and radial thickness of 505 nm, scale bar 1 μm.

Due to its strain-compensated feature, no curving or bending was observed after the under etching of the sacrificial layer, leading to the successful transfer of entire membrane squares. This transfer approach has been applied to fabricate various membrane lasers of ring and disk shapes, with the outer diameters of rings in the range of 1.45-1.65 μm and the diameters of disks in the range of 2-5 μm. Nano-ring laser devices with an outer diameter of ~1.5 μm are shown in Fig. 6.3b.

6.3 Optical Characterization of Nano-ring Laser Devices

Lasing characterization was performed on the nano-ring lasers shown in Fig 6.3b through optical pumping via a 349 nm pulse laser (Spectra Physics, 1 KHz, 5 ns) at an angle of 45 ° from the sample normal with the beam size around 20 μm. RT single mode lasing was

identified through PL spectra evolution under increased pumping strengths shown in Fig. 6.4a as a result of the compact cavity volume (0.24 λ^3).

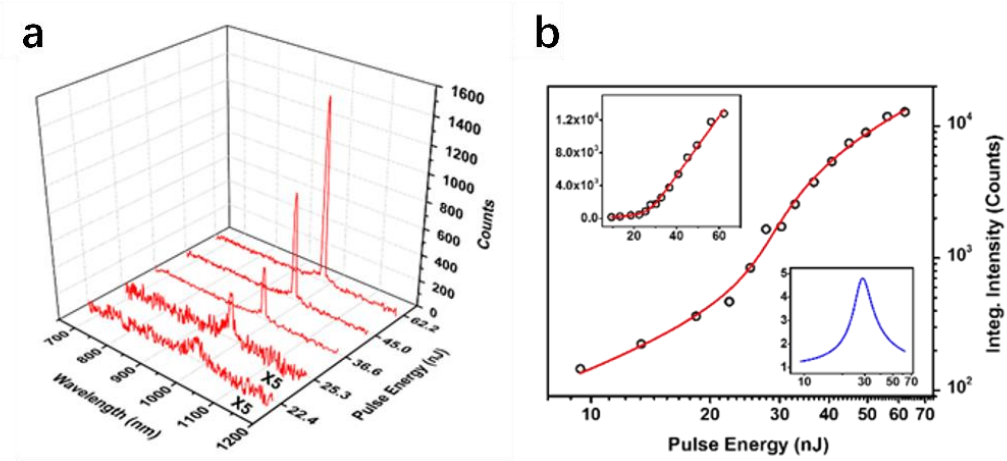

Figure 6.4 Optical characterization and SEM image of nano-ring laser devices (a) Spectra evolution of a nano-ring laser with increase of pumping. (b) Experimentally measured LILO curve (black circles) of (a) on double logarithm scale with lasing rate equation fitting (red solid line). Upper left inset: LILO curve on linear scale. Lower right inset: slope of LILO on double-logarithm scale where the peak (maximum of the slope) indicates the threshold.

At a low pumping level, only broadband spontaneous emissions were observed. At different high pumping levels, a single sharp peak at 980 nm appeared, increasing supper-linearly with pumping levels. This peak eventually became much more intense than the spontaneous emission background with linewidth decreased down to 1.2 nm, which was identified by high resolution spectroscopy. Lasing behavior is also confirmed by the S-shaped LILO curve shown in Fig. 3d. The experimental data of the S-curve is fitted by the single mode rate equations (solid line in Fig. 6.3d), and a good agreement has been reached. Laser threshold is identified through as 29 nJ, equivalent to an average power density of 9 W/cm^2, corresponding to an absorbed power of 4 W/cm^2.

6.4 Summary

In Summary, we have demonstrated a generally applicable and more systematic approach in releasing and transferring semiconductor nano-membranes from grown substrates to receiving substrates. The procedure is robust with the membrane transfer yield >80%. The procedure combined with the strain-balanced membrane design has resulted in a successful transfer of the thinnest nano-membrane so far. As an initial device demonstration, we have fabricated semiconductor membrane lasers of a nano-ring shapes with the outer diameter as small as 1.5 μm, capable of operating at RT. The total volume of the nano-ring laser is only 0.24 λ^3 (λ in vacuum). The transfer method can be applicable to a wide range of substrates, including especially metallic substrates and Si. Such an approach will allow a wide range of device fabrication and integration, providing a general avenue for future nanolaser fabrication and integration.

CHAPTER 7

SUMMARY AND FUTURE WORK

7.1 Summary

The purpose of this section is to briefly summarize the research work presented in this dissertation, which can be refined by four numbers, “one,” “two,” “three” and “four”, specifically stated as follows.

“One,” demand: there is one increasing demand for breakthrough approaches or technologies to overcome the barrier of lattice-mismatch in the traditional planar epitaxial growth to achieve more diverse and compact optical devices toward the realization of PICs in the near future.

“Two,” approaches: two alternative approaches that attempt to surmount the limitation of planar epitaxial growth are adopted in this dissertation, namely the semiconductor NW growth technique in the spirit of the “bottom-up” approach and heterogeneous integration techniques through a general applicable membrane transfer method. With the help of NW growth technique, laser material can be obtained with wide wavelength coverage and tunability. With the help of the membrane transfer method, hybrid integration of III-V compound semiconductors with Si substrates becomes attainable.

“Three,” types of laser devices: the use of those two alternative approaches lead to the demonstration of three types of nanolaser devices, which are monolithic multi-color nanosheet lasers, MIR SWW lasers, and membrane transferred nano-ring lasers.

"Four," key results: four key results have been obtained in this dissertation, containing i) monolithic two-color laser in green and red with wavelength separation of up to 97 nm; ii) monolithic RGB and white laser with color tunability in full visible range; iii) MIR SWW lasers at 3 μm, with cavity volume of $0.44\lambda^3$ (λ in vacuum); iv) single mode membrane transferred nano-ring lasers with cavity volume of $0.24\lambda^3$ (λ in vacuum).

7.2 Future Work

Prospects and recommendations for future research work are introduced in this section, including the monolithic RGB or white lasers and the membrane transferred nano-ring lasers.

For the monolith RGB or white lasers, a more exciting result would be the realization of electrical injection. One specific electrical injection design by taking advantage of current multi-segment heterostructure nanosheets is shown in Fig. 7.1.

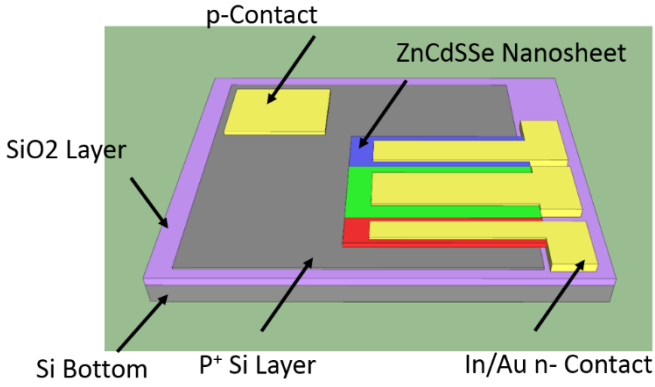

Figure 7.1 Design of monolithic RGB lasers based on multi-segment heterostructure nanosheets for electrical injection.

The design starts with a silicon-on-insulator (SOI) substrate with a ~200 nm thin layer of highly doped p-type Si. The use of the SOI structure is to maximize the optical confinement and minimize the absorption in the p-Si layer. A multi-segment heterostructure nanosheet

is then transferred to and placed at one edge of the highly doped p-type Si to avoid the injection leakage from n-contact to p-type Si. Three separate indium/Au n-contacts are fabricated on the top of each RGB segment and one p-contact is fabricated on the Si area. The diffusion of the indium into the top surface of the nanosheet enables the ohmic contact between the n-metal and nanosheet, similar to Ref [142]. The feasibility of the carrier injection and eventual lasing with a similar configuration has been successfully demonstrated on a NW structure. Compared to the structure in Ref [143], the large lateral dimensions of the nanosheet would make electrical injection much simpler and more efficient than NWs.

For the membrane transferred nano-ring lasers, future dimension miniaturization is demanded. Current sizes of the nano-ring lasers are limited by the use of the photolithograph. Electron beam lithography may need to be applied for even a smaller nanolaser size. Meanwhile, as the size further shrinks, carefully calibrated surface treatment would be required to reduce surface recombination and to preserve PL emission. But such nano-ring or nanomembrane lasers are better than the nano-pillar lasers due to the reduced side wall surfaces. Practical design for efficient electrical injection, satisfactory mode confinement, and low cavity loss may all be needed to develop high-efficiency membrane-based nanolasers.

REFERENCES

[1] Marell, M. J. H., Smalbrugge, B. Geluk, E. J., Veldhoven, P. J. V., Barcones, B., Koopmans, B., Notzel, R., Smit, M. K. & Hill, M. T. Plasmonic distributed feedback lasers at telecommunications wavelengths. *Optics Express* **19**(16), 15109-15118 (2011)

[2] Chuang, S. L. & Bimgerg, D. Metal-Cavity Nanolaser. *IEEE Photonics Journal* **3**(2) 288-292 (2011)

[3] Yang, H., Zhao, D. Chuwongin, S., Seo, J., Yang, W. Shuai, Y., Berggren, J., Hammar, M., Ma, Z. & Zhou, W. Transfer-printed stacked nanomembrane lasers on silicon. *Nature Photonics* **6** 615-620 (2012)

[4] Zhao, D., Liu, S., Yang, H., Ma, Z., Reuterskiold-Hedlun, C. Hammar, M. & Zhou, W. Printed Large-Area Single-Mode Photonic Crystal Bandedge Surface-Emitting Lasers on Silicon. *Scientific Report* **6** 18860 (2016)

[5] Ding, K., Hill, M. T., Liu, Z. C., Yin, L. J., Veldhoven, P. J. V. and Ning, C. Z. Record performance of electrical injection sub-wavelength metallic-cavity semiconductor lasers at room temperature. *Optical Express* **21**(4) 4728-4733 (2013)

[6] Khajavikhan, M., Katz, M., Lee, J. H., Slutsky. B., Mizrahi, A., Lomakin V. & Fainman, Y. Thresholdless nanoscale coaxial lasers. *Nature* **482** 204-207 (2012)

[7] Yu, K., Lakhani, A. & Wu, M. C. Subwavelength metal-optic semiconductor nanopatch lasers. *Optical Express* **18**(9) 8790-8799 (2010)

[8] Oulton, R. F., Sorger, V. J., Zentgraf, T., Ma, R. M., Gladden, C. Dai, L., Bartal, G. & Zhang, X. Plasmon lasers at deep subwavelength scale. *Nature 461* 629-632 (2009)

[9] Ma, R. M., Oulton, R. F., Sorger, V. J. & Zhang, X. Plasmon lasers: coherent light source at molecular scales. *Laser Photonics Rev.* **1** 21 (2012)

[10] Hill, M. T., Marell, M., Leong, E. S. P., Smalbrugge, B., Zhu, Y., Sun, M., Veldhoven, P. J. V., Geluk, E. J., Karouta, F., Oei, Y., Notzel, R. Ning, C. Z. & Smit, M. K. Lasing in metal-insulator-metal sub-wavelength plasmonic waveguides. *Optical Express* **17**(13) 11107-11112 (2009)

[11] Wu, S., Buckley, S., Schaibley, J. R., Feng, L., Yan, J. Mandrus, D. G., Hatami, F., Yao, W., Vuckovic J., Majumdar, A. & Xu, X. Monolayer semiconductor nanocavity lasers with ultralow thresholds. *Nature* **520** 69-72 (2015)

[12] Ye, Y., Wong, J., Lu, X., Ni, X., Zhu, H., Chen, X., Wang, Y. & Zhang, X. Monolayer excitonic laser. *Nature Photonics* **9** 733-737 (2015)

[13] Ding, K., Liu, Z. C., Yin, L. J., Hill, M. T., Marell, M. J. H., Veldhoven, P. J. V., Noetzel, R. & Ning, C. Z. Room-temperature continuous wave lasing in deep-subwavelength metallic cavities under electrical injection. *Phys, Rev, B* **85** 041301 (2012)

[14] Noginov, M. A., Zhu, G., Belgrave, A. M., Bakker, R., Shalaev, V. M., Narimanov, E. E., Stout, S., Herz, E., Suteewong, T. & Wiesner U. Demonstration of a spaser-based nanolaser. *Nature* **460** 1110-1112 (2009)

[15] Yang, P., Yan, H., Mao, S., Russo, R., Johnson, J., Saykally, R., Morris, N., Pham, J., He, R. & Choi, H. J. Controlled growth of ZnO Nanowires and their optical properties. *Adv. Funct. Mater* **12**, 323-331 (2002)

[16] Johnson, J. C., Choi, H. J., Knutsen, K. P., Schaller, R. D., Yang, P. & Saykally, R. J. Single gallium nitride nanowire lasers. *Nature Mater* **1**, 106-110 (2002)

[17] Agarwal, R., Barrelet, C. J. & Lieber, C. M. Lasing in Single Cadmium Sulfide Nanowire Optical Cavities. *Nano Lett.***5**, 917-920 (2005)

[18] Ding, J., Zapien, X. J., Chen, A. W. W., Lifshitz, Y., Lee, S. T. & Meng, X. M. Lasing in ZnS nanowires grown on anodic aluminum oxide templates. *Appl. Phys. Lett.* **85**, 2361-2363 (2004)

[19] Huang, M. H., Mao, S., Feick, H., Yan, H., Wu, Y., Kind, H., Weber, E., Russo, R. & Yang, P. Room-Temperature Ultraviolet Nanowire Nanolasers. *Science* **8**, 1897-1899 (2001)

[20] Wagner, R. S. & Ellis, W. C. Vapor-liquid-solid mechanism of single crystal growth. *Appl. Phys. Lett.* **4**, 89-90 (1964).

[21] Yazawa, M., Koguchi, M., Hiruma, K. Heteroepitaxial ultrafine wire-like growth of InAs on GaAs substrates. *Appl. Phys. Lett.* **58**, 1080-1082 (1991).

[22] Liu, J., Sun, X., Camacho-Aguilera, R., Kimerling, L. C. & Michel, J. Ge-on-Si laser operating at room temperature. *Opt*. Lett. **35**, 679-681 (2010)

[23] Rong, H., Xu, S., Kuo, Y., Sih, V., Cohen, O., Raday, O. & Paniccia, M. Low-threshold continuous-wave Raman silicon laser. *Nature Photon.* **1**, 232-237 (2007)

[24] Groenert, M. E., Christopher, W. L., Pitera, A. J., Yang, V., Lee, H., Ram, R. J. & Fitzgerald E. A. Monolithic integration of room-temperature cw GaAs/AlGaAs lasers on Si substrates via relaxed graded GeSi buffer layers. *J. Appl. Phys.* **93**, 362-367 (2003)

[25] Wirths, S., Geiger, R., Driesch, N. V. D., Mussler, G., Stoica, T., Mantl, S., Ikonic, Z., Luysberg, M., Chiussi, S., Hartmann, J. M., Sigg, H., Faist, J., Buca, D. and

Grutzmacher, D. Lasing in direct-bandgap GeSn alloy grown on Si. *Nature Photon.* **9**, 88-92 (2015)

[26] Fang, A. W., Park, H., Cohen, O., Jones, R., Paniccia, M. J. & Bowers, J. E. Electrically pumped hybrid AlGaInAs-silicon evanescent laser. *Opt. Express* **14**, 9203-9210 (2006)

[27] Van Campenhout, J., Rojo-Romeo, P., Regreny, P., Seassal, C., Van Thourhout, D., Verstuyft, S., Cioccio, L. D., Fedeli, J. M., Lagahe, C. & Baets, R. Electrically pumped InP-base microdisk lasers. *Opt. Express* **15**, 6744-6749 (2007)

[28] Kopp, C., Bernabe, S., Bakir, B. B., Fedeli, J., Orobtchouk, R., Schrank, F., Porte, H., Zimmermann, L. & Tekin, T. Silicon photonic circuits: on-CMOS integration, fiber optical coupling, and packaging. *IEEE J. Sel. Top. Quantum Electon.* **17**, 498-509 (2011)

[29] Rumpler, J. J. & Fonstad, C. J. Continuous-wave electrically pumped 1.55-μm edge-emitting platelet ridge laser diodes on silicon. *IEEE Photon. Tech. Lett.* **21**, 827-829 (2009)

[30] Inoue, D., Hiratani, T., Fukuda, K., Tomiyasu, T., Amemiya, T., Nishiyama, N. & Arai, S. High-modulation efficiency operation of GaInAsP/InP membrane distributed feedback laser on Si substrate. *Opt. Express* **23**(22), 250395 (2015)

[31] Inoue, D., Hiratani, T., Atsuji, Y., Tomiyasu, T., Amemiya, T., Nishiyama, N. & Arai, S. Monolithic Integration of Membrane-Based Butt-Jointed Built-in DFB lasers and p-i-n Photodiodes Bonded on Si Substrate. *IEEE J. Selec. Topics in Quantum Electron.* **21**(6), 1502907 (2015)

[32] Meitl, M. A., Zhu, Z., Kumar, V., Lee, K. J., Feng, X., Huang, Y. Y., Adesida, I., Nuzzo, R. G. & Rogers, J. A. Transfer printing by kinetic control of adhesion to an elastomeric stamp. *Nature Matt.* **5**, 33-38 (2006)

[33] Justice, J., Bower, C., Meitl, M., Mooney, M. B., Gubbins, M. A. & Corbett B. Wafer-scale integration of group III-V lasers on silicon using transfer printing of exitaxial layers. *Nature Photon.* **6**, 610-614 (2012)

[34] Wang, L., Meric, I., Huang, P. Y., Gao, Q., Gao, Y., Tran, H., Taniguchi, T., Watanale, K., Campos, L. M., Muller, D. A, Guo, J., Kim, P., Hone, J., Shepard, K. L. & Dean, C. R., One-Dimensional Electrical Contact to a Two-Dimensional Material. *Science* **342** 614-617 (2013)

[35] Chuang, S. L. *Physics of Photonics Devices, 2nd Edition.* (John Wiley & Sons Inc., 2009)

[36] Singh, J. *Optoelectronics: An Introduction to Materials and Devices.* (McGraw-Hill Inc., 1996)

[37] Coldren, L. A., Corzine, S. W. & Masanovic, M. L. *Diode Lasers and Photonics Integrated Circuits, 2nd Edition.* (John Wiley & Sons Inc., 2012)

[38] Vasileska, D. & Goodnick, S. M. *Computational Electronics.* (Morgan & Claypool Publishers, 2006)

[39] Mohammed, S. N. & Abidi, S. T. H. Current, carrier concentration, Fermi energy, and related properties of binary compound polar semiconductors with nonparabolic energy bands. *J. Appl. Phys.* **60**(4), 1384-1390 (1986)

[40] Bailey, P. T., O'Brien, M. W. & Rabii, S. Direct-Transition Optical Absorption in PbS, PbSe, and PbTe from Relativistic Augmennt-Plane-Wave Functions. *Physical Review* **179**(3), 736-739 (1969)

[41] Henry, C. H. Theory of the Linewidth of Semiconductor Lasers. *IEEE J. Electron.* **QE-18**(2), 259-264 (1982)

[42] Ascher, U. M. & Petzold, L. R. Computer Methods for Ordinary Differential Equations and Differential-Algebraic Equations. (Society for Industrial and Applied Mathematics, 1998)

[43] Mayer, B., Loitsch, B., Treu, J., Kostenbader, T., Lichtmannecher, S., Reichert, T., Morkotter, S., Kaniber, M., Abstreiter, G., Gies, C., Koblmuller, G. & Finley J. J. Monolithically Integrated High-β Nanowire Lasers on Silicon. *Nano Lett.* **16**, 152-156 (2016)

[44] Ning, C. Z. Semiconductor Nanolasers. *Phys. Status Solidi B* **247**(4), 7774-788 (2010)

[45] Balanis, C. A., *Advanced Engineering Electromagnetics, 2nd Edition.* (John Wiley & Sons Inc., 2012)

[46] Marcatili, E. A. J. Dielectric rectangular waveguide and directional coupler for integrated optics. *Bell Syst. Tech. J.* **48** 2071-2102 (1969)

[47] Ryu, J. W., Rim, S., Park, Y. J., Kim, C. M. & Lee, S. Y., Resonances in ciruclar dielectric caivty. *Phys. Lett. A* **372** 3531-3536 (2009)

[48] Zou, C. L., Yang, Y., Xiao, Y, F., Dong, C. H., Han, Z. F. & Guo, G. C. Accurately calculating high quality factor of whispering-gallery modes with boundary element method. *J. Opt. Soc. Am. B* **26**(11) 2050-2053 (2009)

[49] Neumann, A., Wierer Jr., J. J., Davis, W., Ohno, Y., Brueck, S. R. J. & Tsao, J. Y. Four-color laser white illuminant demonstrating high color-rendering quality. *Opt. Express* **19**, A982-A990 (2011)

[50] Baker, C. E. Laser display technology. *IEEE Spectrum* **5**, 39-50 (1968)

[51] Zhao, J. L., Jiang, H. Z. & Di, J. L. Recording and reconstruction of a color holographic image by using digital lensless Fourier transform holography. *Opt. Express* **16** 2514-2519 (2008)

[52] Kotani, A., Witek, M. A., Osiri, J. K., Wang, H., Sinville, R., Pincas, H., Barany, F. & Soper, S. A. EndoV/DNA ligase mutation scanning assay using microchip capillary electrophoresis and dual-color laser-induced fluorescence detection. *Anal. Methods* **4**, 58 (2012)

[53] Lin, W. Y., Chen, C. Y., Lu, H. H., Chang, C. H., Lin, Y. P., Lin, H. C. & Wu, H. W. 10 m/500 Mbps WDM visible light communication systems. *Opt. Express* **20**, 9919–9924 (2012)

[54] Cossu, G., Khalid, A. M., Choudhury, P., Corsini, R. & Ciaramella, E. 3.4 Gbit/s visible optical wireless transmission based on RGB LED. *Opt. Express* **20**, B501–B506 (2012)

[55] Girndt, A., Koch, S. W. & Chow, W. W. Microscopic theory of laser gain in semiconductor quantum wells. *Appl. Phys. A* **66**, 1-12 (1998)

[56] Yoshida, H., Gonno, Nakano, Y., Taniguchi, K. S., Hino, T., Ishibashi, A., Ikeda, M. & Chuang, S. L. Gain characteristics of gainguided II–VI laser diodes. *Appl. Phys. Lett.* **69**, 3893-3895 (1996)

[57] Lougue, F. P., Rees, P., Heffernan, J. F., Jordan, C., Donegan, J. F., Hegarty, J., Hiei, F., Taniguchi, S., Hino, T., Nakano, K. & Ishibashi, A. Optical gain in (Zn, Cd)Se-Zn(S, Se) quantum wells. *J. Opt. Soc. Am. B* **15**, 1295-1304 (1997)

[58] Girndt, A., Jahnke, F., Knorr, A., Koch, S. W. & Chow, W. W. Multi-Band bloch equations and gain spectra of highly excited II-VI semicondutor quantum wells. *Phys. Stat. Sol. B* **202**, 725-739 (1997)

[59] Yamada, Y., Masumotoa, Y. & Taguchi, T. Formation of optical gain due to exciton localization in CdxZn1−xS-ZnS strained-layer quantum wells. *Physica B: Cond. Mat.* **191**, 83-89 (2002)

[60] Klingshirn, C., Kalta, H., Umlauffa, M., Petria, W., Majumdera, F. A., Bogdanova, S. V., Langbeina, W., Grüna, M., Hettericha, M., Geyzersb, K. P., Heukenb, M., Naumovc, A., Stanzlc, H. & Gebhardtc, W. Stimulated emission of II–VI epitaxial layers. *J. Crys. Growth* **138**, 786-790 (1994)

[61] Motisuke, P., Argüello, C. A. & Luzzi, R. Effect of excited electron states lifetime on gain spectra of EHL in CdS. *Solid State Commun.* **23**, 617-620 (1977)

[62] Pan, A. L., Zhou, W., Leong, E. S. P., Liu, R., Chin, A. H., Zou, B. & Ning, C. Z. Continuous alloy-composition spatial grading and superbroad wavelength-tunable nanowire lasers on a single chip. *Nano Lett.* **9**, 784-788 (2009)

[63] Pan, A. L., Liu, R. B., Sun, M. H. & Ning, C. Z. Spatial composition grading of quaternary ZnCdSSe alloy nanowires with tunable light emission between 350 and 710 nm on a single substrate. *ACS. Nano* **4**(2), 671-680 (2010)

[64] Liu, Y., Zapien, J. A., Shan, Y. Y., Geng, C. Y., Lee, C. S. & Lee, S. T., Wavelength controlled lasing in $Zn_xCd_{1-x}S$ single crystal nanoribbons. *Adv. Mater.* **17**, 1372-1377 (2005)

[65] Zapien, J., Liu, Y., Shan, Y., Tang, H., Lee, C. & Lee, S. T. Continuous near-infrared-to-ultraviolet lasing from II-VI nanoribbons. *Appl. Phys. Lett.* **90**, 213114-213116 (2007)

[66] Kuykendall, T., Ulrich, P., Aloni, S. & Yang, P. D. Complete composition tunability of InGaN nanowires using a combinatorial approach. *Nat. Mater.* **6**, 951-956 (2007)

[67] Ding, Y., Yang, Q., Guo, X., Wang, S., Gu, Fu, F., Wan, J., Cheng, Q. J. & Tong, L. Nanowires/microfiber hybrid structure multicolor laser. *Opt. Express* **17**, 21813-21818 (2009)

[68] Naderi, N. A., Grillot, F., Yang, K., Wright, J. B., Gin, A. & Lester, L. F. Two-color multi-section quantum dot distributed feedback laser. *Opt. Express* **16**, 27028-27035 (2010)

[69] Tang, S. K. Y., Li, Z., Abate, A. R., Agresti, J. J., Weitz, D. A., Psaltis, D. & Whitesides, G. M. A multi-color fast-switching microfluidic droplet dye laser. *Lab Chip* **9**, 2767-2771 (2009)

[70] Wang, Y., Tsiminis, G., Yang, Y., Ruseckas, Kanibolotsky, A. L., Perepichka, I. F., Skabara, P. J., Turnbull, G. A., Samuel, I. D. W., Broadly tunable deep blue laser based on a star-shaped oligofluorene truxene. *Synthetic Metals* **160**, 1397-1400 (2010)

[71] Kloepfer, J. A., Mielke, R. E., Nadeau, J. L., CdSe quantum dot internalization by Bacillus subtilis and Escherichia coli. *Proc. SPIE* **5361**, 133-141 (2004)

[72] Nichols, P. Growth and Characterization of Chalcogenide Alloy Nanowires with Controlled Spatial Composition Variation for Optoelectronic Applications (Doctoral Dissertation). *Arizona State University* (2012)

[73] Gu, F. X., Yang, Z. Y., Yu, H. K., Xu, J. Y., Wang, P., Tong, L. M. & Pan, A. L. Spatial Bandgap Engineering along Single Alloy Nanowires. *J. Am. Chem. Soc.* **133**, 2037−2039 (2011)

[74] Liu, Z., Yin, L., Ning, H., Yang, Z. Tong, L. & Ning, C. Z. Dynamical Color-Controllable Lasing with Extremely Wide Tuning Range from Red to Green in a Single Alloy Nanowire Using Nanoscale Manipulation. *Nano Lett.* **13**, 4945-4950 (2013)

[75] Palik, E. D. Handbook of Optical Constants of Solids Volume IV (Elsevier Inc. 1997)

[76] Sobolev, V. V., Donetskina, V. I. & Zagainov, E. F. Direct precision method for detection of excitons in II-VI and III-V crystals at room and liquid nitrogen temperatures. *Sov. Phys. Semicond.,* **12**, 646-652 (1978)

[77] Logothetidis, S., Cardona, M., Lautenschlager, P. & Garriga, M. Temperature dependence of the dielectric function and the interband critical points of CdSe. *Phys. Rev. B,* **34**, 2458-2469 (1986)

[78] Mzerd, A., Sayah, D., Saunders, I. J. & Jones, B. K. Electrical Properties of $Cd_{1-y}Zn_yS$ and CdS(In) Thin Films Prepared by Pyrolytic Spray Technique. *Phys. Status Solidi A*, **119**, 487-494 (1990)

[79] Levy, M. & Sarachik, M. P. A calibration curve for room-temperature resistivity versus carrier concentration in n-type CdSe. *J. Appl Phys.,* **69**, 2703-2704 (1991)

[80] Kim, Y. L., Jung, J. H., Yoon, H. S., Song, M. S., Bae, S. H., Kim, Y., Chen, Z. G., Zou, J., Joyce, H. J., Gao, Q., Tan, H. H. & Jagadish, C. CdS/CdSe lateral heterostructure nanobelts by a two-step physical vapor transport method. *Nanotechnology* **21**, 145602 (2010)

[81] Tong, L. M., Lou, J. Y., Gattass, R. R., He, S. L., Chen, X. W., Liu, L. & Mazur, E. Assembly of silica nanowires on silica aerogels for microphotonic devices. *Nano Lett.* **5**, 259-262 (2005)

[82] Kwon, S. J., Choi, Y.J., Park, J. H., Hwang, I. S. & Park, J. G. Structural and optical properties of CdS_xSe_{1-x} nanowires. *Phys. Rev. B* **72**, 205312 (2005)

[83] Zimmler, M. A., Capasso, F., Muller, S. & Ronning, C. Optically pumped nanowire lasers: Invited review. *Semicond. Sci. Technol.* **25**, 024001 (2010)

[84] O'Carroll, D., Lieber, wirth, I. & Redmond, G. Microcavity effects and optically pumped lasing in single conjugated polymer nanowires. *Nature Nanotechnology* **2**, 180-184 (2007)

[85] Johnson, J. C., Yan, H., Yang, P. & Saykally, R. J. Optical Cavity Effects in ZnO Nanowire Lasers and Waveguides. *J. Phys. Chem. B* **107**, 8816-8828 (2003)

[86] Ma, R. M., Oulton, R. F., Sorger, V. J., Bartal, G. & Zhang, X. Room-temperature sub-diffraction-limited plasmon laser by total internal reflection. *Nat. Mater.* **10**, 110-113 (2011)

[87] Casperson, L. W. Threshold characteristics of multimode laser oscillators. *J. App. Phys.* **46**, 5194-5201 (1975)

[88] Hu, X. P., Zhao, Z., Wang, X., Gao, Z. D., Liu, H., He, J. L. & Zhu, S. N. High-power red-green-blue laser light source based on intermittent oscillating dual-wavelength Nd: YAG laser with a cascaded $LiTaO_3$ superlattice. *Opt. Lett.* **33**, 408-410 (2008).

[89] Fujimoto, Y., Ishii, O. & Yamazaki, M. Multi-color laser oscillation in Pr3+ doped fluoro-aluminate glass fiber pumped by 442.6 nm GaN-semiconductor laser. *Electron. Lett.* **45**, 1301-1302 (2009)

[90] Yamashita, K., Takeuchi, N., Oe, K. & Yanagi, H. Simultaneous RGB lasing from a single-chip polymer device. *Opt. Lett.* **35**, 2451-2453 (2010)

[91] Alivisatos, A. P. Semiconductor clusters, nanocrystals, and quantum dots. *Science* **271**, 933-937 (1996)

[92] Huang, Y., Duan, X. F. & Lieber, C. M. Nanowires for integrated multicolor nanophotonics. *Small* **1**, 142-147 (2005)

[93] Yang, Z., Xu, J., Wang, P., Zhuang, X., Pan, A. & Tong, L. On-nanowire spatial band gap design for white light emission. *Nano Lett.* **11**, 5085-5089 (2011)

[94] Dang, C., Lee, J., Breen, C., Steckel, J. S., Coe-Sullivan S. & Nurmikko A. Red, green and blue lasing enabled by single-exciton gain in colloidal quantum dot films. *Nat. Nanotech.* **7**, 335-339 (2012)

[95] Anikeeva, P. O., Halpert, J. E., Bawendi, M. G. & Bulovic, V. Quantum dot lightemitting devices with electroluminescence tunable over the entire visible spectrum. *Nano Lett.* 9, 2532-2536 (2009)

[96] Kim, T., Cho, K., Lee, E. K., Lee, S. J., Chae, J., Kim, J. W., Kim, D. H., Kwon, J. Amaratunga, G., Lee, S. Y., Choi, B. L., Kuk, Y., Kim, J. M. & Kim K. Full-colour quantum dot displays fabricated by transfer printing. *Nature Photon.* **5**, 176-182 (2011)

[97] VEM. Thin Film Evaporation Guide (Lebow Corporation and Vacuum Engineering & Materials Inc., 2008)

[98] Fang, X., Zhai, T., Gautam, U. K., Li, L., Wu., L., Bando, Y. & Golberg, D. ZnS nanostructures: from synthesis to applications. *Prog. Mater. Science.* **56**, 175-287 (2011)

[99] Yue, G. H., Yan, P. X., Yan, D., Liu, J. Z., Qu, D. M., Yang, Q. & Fan, X. Y. Synthesis of two-dimensional micron-sized single-crystalline ZnS thin nanosheets and their photoluminescence properties. *J. Cryst. Growth.* **293**, 428-432 (2006)

[100] Moore, D. & Wang, Z. L. Growth of anisotropic one-dimensional ZnS nanostructures. *J. Mater. Chem.* **16**, 3898-3905 (2006)

[101] Harrison, W. A. *Electronic Structure and the Properties of Solids*. (Dover Publication Inc.: New York, 1989)

[102] Ichino, K. *Molecular beam epitaxy and characterization of heterostructures with ZnCdSSe quaternary alloys for light emitting devices*. Kyoto University (1994)

[103] Yamaguchi, T., Yoshida, H., Abe, T., Kasada, H. & Ando, K. Microdefects and Minority Carrier Diffusion Lengths in II-VI Wide-Gap Semiconductors. *Elec. and Comm. In Japan.* **81**(10), 55-63 (1998)

[104] Maslov, A. V. & Ning, C. Z. Modal Gain in a Semiconductor Nanowire Laser with Anisotropic Bandstructure. *IEEE J. Quant. Electron.* **40**(10), 1389-1397 (2004)

[105] Chow, W. W. & Koch, S. W., *Semiconductor-Laser Fundamentals.* (Springer, Berlin, German, 1999)

[106] Tamargo, M. C. II-VI *Semiconductor Materials and their Applications.* (Taylor & Francis: New York, 2002)

[107] Gorkavenko, T. V., Zubkova, S. M., Makara, V. A. & Rusina, L. N. Temperature Dependence of the Band Structure of ZnS, ZnSe, ZnTe, and CdTe Wurtzite-Type Semiconductor Compounds, *Semiconductor*. **41**(8), 886-896 (2007)

[108] Palmer, D. W. (source: http://www.semiconductors.co.uk).

[109] Pan, A. L., Liu, R. B., Sun, M. H. & Ning, C. Z. Quaternary alloy semiconductor nanobelts with bandgap spanning the entire visible spectrum. *J. Am. Chem. Soc.* **131**, 9502–9503 (2009)

[110] Deng, Z., Yan, H. & Liu, Y. Band gap engineering of quaternary-alloyed ZnCdSSe quantum dots via a facile phosphine-free colloidal method. *J. Am. Chem. Soc.* **131**, 17744-17745 (2009).

[111] Ichino, K., Onishi, T., Kawakami, Y., Fujita, S. & Fujita, S. Growth of ZnS and ZnCdSSe alloys on GaP using an elemental sulfur source by molecular beam epitaxy. *J. Cryst. Growth.* **138**, 28-34 (1994)

[112] Wang, Y., Liu, M., Ling, T., Tang, C., Zhi, C. & Du, X. Gas-phase anion exchange towards ZnO/ZnSe heterostructures with intensive visible light emission. *J. Mater. Chem. C.* **2**, 2793-2798 (2014)

[113] Dloczik, L. & Konenkamp, R. Nanostructure transfer in semiconductors by ion exchange. *Nano Lett.* **3**, 651-653 (2003)

[114] Fan, Z., Ho., J. C., Jacobson, Z. A., Yerushalmi, R., Alley, R. L., Razavi, H. & Javey, A. Wafer-scale assembly of highly ordered semiconductor nanowire arrays by contact printing. *Nano Lett.* **8**, 20-25 (2008).

[115] Fan, F., Liu, Z., Yin, L., Nichols, P. L., Ning, H., Turkdogan, S. & Ning, C. Z. Simultaneous two-color lasing in a single CdSSe heterostructure nanosheet. *Semicond. Sci. Technol.* **28**, 065005 (2013).

[116] Ning, C. Z. What is Laser Threshold? *IEEE Journal of Selected Topics in Quantum Electronics*, **19**(4), 1503604 (2013)

[117] International Commission on Illumination. CIE 15: Colorimetry Technical Report, 3rd Edition. *US Gov. Doc.* (2004)

[118] Xu, Z., & Bi, Y. Large laser projection displays utilizing all-solid-state RGB lasers. *Proc. of SPIE* **5632** 115-122 (2005).

[119] International Electrotechnical Commission. Multimedia systems and equipment-colour measurement and management-part 2-1: Colour management–default RGB colour space–sRGB. *IEC* 61966-2-1, (1999).

[120] Hunter, R. S. Photoelectric Color-Difference Meter. *J.O.S.A.* **38**(7), 661 (1948).

[121] Geburt, S., Thielmann, A. Roder, R., Borschel, C., McDonnell, A., Kozlik, M., Kuhnel, J., Sunter, K. A., Capasso, F. & Ronning, C. Low threshold room-temperature lasing of CdS nanowires. *Nanotech.* **23** 365204 (2012)

[122] Pan, A., Liu, R., Zhang, Q., Wang, Q., He, P., Zacharias, M. & Zou, B. Fabrication and Red-Color Lasing of Individual highly Uniform Single-Crystal CdSe Nanobelts. *J. Phys. Chem. C.* **111**, 14253-14256 (2007).

[123] Zimmler, M. A., Bao, J., Capsso, F., Muller, S. and Ronning, C. Laser action in nanowires: Observation of the transition from amplified spontaneous emission to laser oscillation. *App. Phys. Lett.* **93**, 051101 (2008)

[124] Okazaki, K., Nakamura, D., Higashihata, M., Iyamperumal, P. and Okada, T. Lasing characteristics of an optically pumped single ZnO nanosheet. *Opt. Exp.* **19**, 20389-20394 (2011).

[125] Hou, D., Wu, H. and Liu, Y. Preparation of ultrawide ZnSe nanoribbons with the function of lasing cavity. *Opt. Elec.* **6**, 0241-0244 (2013)

[126] Lu, Y., Gu, F., Meng, C., Yu, H., Ma, Y., Fang, W. & Tong, L. M. Multicolour laser from a single bandgap graded CdSSe alloy nanoribbons. *Opt. Exp.* **21**, 22314-22319 (2013).

[127] Xu, J., Ma, L., Guo, P., Zhuang, X., Zhu, X., Hu, W., Duan, X. & Pan. A. Room-Temperature Dual-Wavelegnth Lasing from Single-Nanoribbon Lateral Heterostructures. *J. Amer. Chem. Soc.* **134** 12394-12397 (2012).

[128] Pan, A., Liu, R., Yang, Q., Zhu, Y., Yang, G., Zou, B. & Chen, K. Stimulated Emissions in Aligned CdS Nanowires at Room Temperature. *J. Phys. Chem. B* **109** 24268-24272 (2005).

[129] Roder, R., Ploss, D., Kriesch, A., Buschlinger, R., Geburt, S., Peschel, U. & Ronning, C. Polarization features of optically pumped CdS nanowire lasers. *J. phys. D: App. Phys.* **47** 394012 (2014).

[130] McCann, P. J. Mid-Infrared lasers and molecular spectroscopy applications. *LEOS 19th Annual Meeting of the IEEE* **MM4**, (2006)

[131] Yasumoto, M., Tomimasu, T., Ishizu, A., Tsubouchi, N., Awazu, K., & Umesaki, N. Thin-film deposition method assisted by mid-infrared-FEL. *Nuclear Instruments and Methods in Physics Research A* **475**, 640-644 (2001)

[132] Topfer, T., Petrov, K. P., Mine, Y., Jundt, D., Curl, R. F., & Tittel, F. K., Room-temperature mid-infrared laser sensor for trace gas detection. *Applied Optics* **36**, 8024 (1997)

[133] Waynant, R. W., Ilev, I. K., & Gannot, I. Mid-infrared laser applications in medicine and biology. *Phil. Trans. R. Soc. Lond. A* **359**, 635 (2001)

[134] Chen, R., Tran, T. D., Ng, K. W., Ko, W. S., Chuang, L. C., Sedgwick, F. G., & Chang-Hasnain, C. Nanolasers grown on silicon. *Nature Photon.* **5**, 170-175 (2011)

[135] Chin, A. H., Vaddiraju, S., Maslov, A. V., Ning, C. Z., Sunkara, M. K., & Meyyappan, M., Near-infrared semiconductor subwavelength wire lasers. *App. Phys. Lett.* **88**, 163115 (2006)

[136] Findlay, P. C., Kotitschke, C. R. R., Hollinggworth, A., Murdin, B. N., Langerak, C. J. G. M., van der Meer, A. F. G., Oswald, J., Homer, A., Springholz, G. & Bauer. G. Auger recombination dynamics of lead salts under picosecond free-electron-laser excitation. *Phys. Rev. B.* **58**, 12908-12915 (1998)

[137] Preier, H. Recent Advances in Lead-Chalcogenide Diode Lasers. *App. Phys.* **20**, 189-206 (1979)

[138] Dalven, R. Electronic Structure of PbS, PbSe, and PbTe. *Solid State Phys.* **28**, 179-224 (1974)

[139] Nichols, P. L., Sun, M., & Ning, C. Z. Influence of Supersaturation and Spontaneous Catalyst Formation on the Growth of PbS Wires: Toward a Unified Understanding of Growth Modes. *ACS Nano* **5**, 8730-8738 (2011)

[140] Liang, D. & Bower, E. Recent progress in lasers on silicon. *Nature Photon.* **4**, 511-517 (2010)

[141] Sheng, X., Robert,,C., Wang, S., Pakeltis, G., Corbett, B. & Rogers, J. A. Transfer printing of fully formed thin-film microscale GaAs lasers on silicon with a thermally conductive interface material. *Laser Photon. Rev.* **9**(4), L17-L22 (2015)

[142] Ma, R. M., Dai, L. & Qin, G. G. High-Performance Nano-Schottky Diodes and Nano-MESFETs Made on Single CdS Nanobelts. *Nano Lett.* **7** 868-873 (2007)

[143] Duan, X., Huang, Y., Agarwal, R. & Lieber, C. M. Single-nanowire electrically driven lasers. *Nature* **421** 241-245 (2003)